The Analysis of an Organic Rankine Cycle for Smaller Concentrated Solar Powered Systems

by
Louis Karsten

Thesis presented in partial fulfilment of the requirements for the degree of Master of Engineering Mechanical in the Faculty of Engineering at Stellenbosch University

Supervisor: Prof Frank Dinter
Co-supervisor: Dr Jaap Hoffmann

December 2018

DECLARATION

By submitting this thesis electronically, I declare that the entirety of the work contained therein is my own, original work, that I am the sole author thereof (save to the extent explicitly otherwise stated), that reproduction and publication thereof by Stellenbosch University will not infringe any third party rights and that I have not previously in its entirety or in part submitted it for obtaining any qualification.

Date: December 2018

Plagiaatverklaring / *Plagiarism Declaration*

1 Plagiaat is die oorneem en gebruik van die idees, materiaal en ander intellektuele eiendom van ander persone asof dit jou eie werk is.
Plagiarism is the use of ideas, material and other intellectual property of another's work and to present is as my own.

2 Ek erken dat die pleeg van plagiaat 'n strafbare oortreding is aangesien dit 'n vorm van diefstal is.
I agree that plagiarism is a punishable offence because it constitutes theft.

3 Ek verstaan ook dat direkte vertalings plagiaat is.
I also understand that direct translations are plagiarism.

4 Dienooreenkomstig is alle aanhalings en bydraes vanuit enige bron (ingesluit die internet) volledig verwys (erken). Ek erken dat die woordelikse aanhaal van teks sonder aanhalingstekens (selfs al word die bron volledig erken) plagiaat is.
Accordingly all quotations and contributions from any source whatsoever (including the internet) have been cited fully. I understand that the reproduction of text without quotation marks (even when the source is cited) is plagiarism.

5 Ek verklaar dat die werk in hierdie skryfstuk vervat, behalwe waar anders aangedui, my eie oorspronklike werk is en dat ek dit nie vantevore in die geheel of gedeeltelik ingehandig het vir bepunting in hierdie module/werkstuk of 'n ander module/werkstuk nie.
I declare that the work contained in this assignment, except otherwise stated, is my original work and that I have not previously (in its entirety or in part) submitted it for grading in this module/assignment or another module/assignment

17180430 **Studentenommer / *Student number***	**Handtekening / *Signature***
L Karsten **Voorletters en van / *Initials and surname***	**Datum / *Date:*** *2018/09/07*

Abstract

The Analysis of an Organic Rankine Cycle for Smaller Concentrated Solar Powered Systems

Louis Karsten

Department of Mechanical and Mechatronic Engineering,
Stellenbosch University,
Private Bag X1, Matieland 7602, South Africa
Thesis: MEng (Mech)
December 2018

Small-scale energy consumers (500 kWe – 5 MWe), that are situated in off-grid areas are often left reliant on fossil fuels (like diesel generators) to meet their energy needs. The International Energy Association (IEA) however attempts to decarbonise the entire energy system and has set certain goals for the renewable energy sector. Most renewable energy sources offer only intermitted power solutions for small-scale off-grid applications and storing electrical energy for this scale becomes expensive. Concentrated solar power (CSP) can offer a non-intermitted solution by having the added benefit of thermal energy storage (TES). However, the critical barrier to the widespread usage of small-scale CSP is the lack of optimised and economically competitive technology. Steam Rankine cycles are typically integrated with CSP in large-scale applications but the thermodynamic properties of steam however prohibit water being used as suitable working fluid in lower temperature and lower power output applications. The aim of this thesis is therefore to determine whether the integration of an organic Rankine cycle (ORC), with a smaller CSP system can result in a feasible energy solution for off-grid applications.

The first step taken was to determine the technical feasibility of solar integrated organic Rankine cycle (SORC) technology. It was proven feasible by the operation of existing small-scale SORC plants. ORC's and CSP as separate types of technology are being used in various industries. The integration of CSP with an ORC is however considered an immature technology.

A small-scale application in the higher DNI region of South Africa was identified to use as case study. Black Mountain mine near the town Aggeneys was selected by using a multi criteria decision analysis tool. Even though Black Mountain mine is grid-connected, it is still a viable case study to analyse whether an SORC can be a feasible solution for a mine. In proving so, the proposition then exists to use a SORC for future mining developments in off-grid areas.

A SORC was theoretically analysed by looking at the solar field, TES and power block separately. The theory developed was then combined to create a model for a

SORC. The simulation was conducted on MatLab and the design point was resultantly determined at a plant efficiency of 12.8 % and a turbine inlet pressure and evaporating temperature of 2858.8 kPa and 186 °C respectively. The simulation was then expanded to run over a period of one year and a maximum capacity factor of 83 % was recorded. The lowest achievable levelised cost of electricity (LCOE) was 16.7 $c/kWh at a solar multiple (SM) of 1.7 and TES size of 6 hours. The conclusion was reached that SORC's are economically competitive with diesel generators but cannot solely meet the required energy demand and must therefore utilise auxiliary energy sources.

Uittreksel

Die Analise van ‘n Organiese Rankine Siklus vir die gebruik van Kleiner Gekonsentreerde Son Aangedrewe Stelsels

Louis Karsten

Departement van Meganiese en Megatroniese Ingenieurswese,
Universiteit van Stellenbosch,
Privaatsak X1, Matieland 7602, Suid Afrika

Tesis: MIng (Meg)
Desember 2018

Kleinskaalse energie verbruikers (500 kWe – 5 MWe), wat buite elektrisiteitsnetwerkgebiede geleë is, is dikwels afhanklik van fossiel brandstowwe (soos diesel kragopwekkers) om hul energie behoeftes te bevredig. Die Internasionale Energievereniging (IEA) poog egter om die hele energiesisteem te koolstof vry te maak en het sekere doelwitte vir die hernubare energie sektor gestel. Die meeste hernubare energiebronne bied slegs onderbroke kragoplossings vir kleinskaalse buite elektrisiteitsnetwerk toepassings. Die stoor van elektriese energie op hierdie skaal word buitendien ook duur. Gekonsentreerde sonkrag (CSP) kan 'n ononderbroke oplossing bied deur die bykomende voordeel van warmte-energie berging (TES) te hê. Die kritieke beperking vir die wydverspreide gebruik van kleinskaalse CSP is egter die gebrek aan optimale en ekonomies mededingende tegnologie. Stoom Rankine siklusse word tipies geïntegreer met CSP in grootskaalse toepassings, maar die termodinamiese eienskappe van stoom verbied egter dat water as geskikte werkvloeistof in laer temperature en laer kraguitsettoepassings gebruik word. Die doel van hierdie tesis is dus om vas te stel of die integrasie van 'n organiese Rankine-siklus (ORC) met 'n kleiner CSP-stelsel tot 'n haalbare energie-oplossing vir buite elektrisiteitsnetwerk toepassings kan lei.

Die eerste stap is uitgevoer deur die tegniese uitvoerbaarheid van sonkrag-geïntegreerde organiese Rankine-siklus (SORC) tegnologie te bepaal. Die uitvoerbaarheid is bewys deur die bedryf van bestaande kleinskaalse SORC-aanlegte. ORC's en CSP as afsonderlike tipes tegnologie word in verskeie nywerhede gebruik. Die integrasie van CSP met 'n ORC word egter beskou as 'n onvolwasse tegnologie.

'n Kleinskaalse toepassing in die hoër DNI-streek van Suid-Afrika is geïdentifiseer as gevallestudie. Black Mountain myn naby die dorp Aggeneys is gekies met behulp van 'n multi-kriteria besluitanalise instrument. Selfs al is die Black Mountain myn aan die elektrisiteitsnetwerk verbind, is dit steeds 'n

lewensvatbare gevallestudie om te ontleed of 'n SORC 'n haalbare oplossing vir 'n myn kan wees. Sodoende, bestaan die voorstel om 'n SORC te gebruik vir toekomstige ontginningsontwikkelings wat nie aan die elektrisiteitsnetwerk verbind is nie.

'n SORC is teoreties ontleed deur afsonderlik na die sonveld, TES en kragblok te kyk. Die teorie wat ontwikkel is, is dan gekombineer om 'n model vir 'n SORC te skep. Die simulasie is op MatLab uitgevoer en die ontwerppunt is gevolglik bepaal by 'n aanlegsbenuttingsgraad van 12.8 % en 'n turbine inlaatdruk en verdampingstemperatuur van onderskeidelik 2858,8 kPa en 186 °C. Die simulasie is dan uitgebrei om oor 'n tydperk van een jaar te hardloop en 'n maksimum kapasiteitsfaktor van 83 % is aangeteken. Die laagste haalbare gerealiseerde koste van elektrisiteit (LCOE) was 16.7 $c/kWh teen 'n sonveelvoud (SM) van 1.7 en TES grootte van 6 uur. Die gevolgtrekking is gemaak dat SORC's ekonomies mededingend is met dieselgenerators, maar nie alleen in die energie vraag kan voorsien nie en dus bykommende energie hulpbronne moet gebruik.

Acknowledgements

I would like to honour and express my sincere gratitude to the following individuals and organisations for their contribution towards the successful completion of this thesis:

- Dr Jaap Hoffmann for his guidance, advice, making it possible to attend a conference abroad and patience in the completion of this thesis.

- Prof Frank Dinter for his supervision, guidance and inputs throughout the duration of the thesis.

- My family especially my mother and father for their constant encouragement and motivation.

- All my friends for their support especially Jan-Louis janse van Vuuren for his engagement in resolving the challenges my studies presented.

- The whole of STERG for all the relevant and irrelevant conversations for creating a pleasant working environment.

- The financial assistance of the National Research Foundation (NRF) towards this research is hereby acknowledged. Opinions expressed and conclusions arrived at, are those of the author and are not necessarily to be attributed to the NRF.

- Most importantly, my Lord and Saviour Jesus Christ, for all things have been created through Him and for Him.

Dedication

"Whatever you do, work at it with all your heart, as working for the Lord, not for human masters, since you know that you will receive an inheritance from the Lord as a reward. It is the Lord Christ you are serving." - **Colossians 3:23-24**

Table of Contents

List of Figures

List of Tables

Nomenclature

Abbreviations

ACC	Air cooled condenser
CSP	Concentrated solar power
DHI	Diffuse horizontal irradiation
DNI	Direct normal irradiance
GHI	Global horizontal irradiation
HTF	Heat transfer fluid
HVAC	Heating, ventilation and cooling
IEA	International Energy Association
ITD	Initial temperature difference
LCOE	Levelised cost of electricity
LFR	Linear Fresnel reflectors
MCDA	Multi criteria decision analysis
NELHA	National Energy Laboratory of Hawaii Authority
NREL	National Renewable Energy Laboratory
PT	Parabolic trough
REIPPPP	Renewable Energy Independent Power Producer Procurement Programme
RMSE	Root mean square error
RO	Reverse osmosis
SAM	System advisor model
SCA	Solar collector assembly
SF	Solar field
SM	Solar multiple
SMART	Simple multi-attribute rating technique
SORC	Solar integrated organic Rankine cycle
TES	Thermal energy storage

Constants

g_c	Proportionality constant	[-]
g	Gravitational constant	[m/s^2]
σ	Stefan-Boltzmann constant	[W/m^2K^4]

Symbols

A	Area	[m^2]
C_p	Heat capacity	[kJ/(kgK)]
D	Diameter	[m]
e	Error	[-]
E_a	Net annual electricity	[MWh]
EOT	Equation of time	[minutes]
f	Friction factor	[-]
Gr	Grashof number	[-]
H	Bernoulli head	[m]
h	Enthalpy	[kJ/kg]
h	Heat transfer coefficient	[$W/(m^2K)$]
I	Irradiation	[W/m^2]
l	Length	[m]
k	Thermal conductivity	[W/m °C]
kd	Annual debt interest rate	[%]
k_f	Burnt fuel costs	[%]
$k_{insurance}$	Annual insurance interest rate	[%]
K_L	Loss coefficient	[-]
K_θ	Incidence angle modifier	[-]
LC	Longitude correction	[hours]
LCT	Local time	[hours]
$\dot{m}$	Mass flow rate	[kg/s]
N	Number of day of the year	[-]
Nu	Nusselt number	[-]

p	Perimeter	[m]
P	Pressure	[kPa]
Pr	Prandtl number	[-]
$\dot{q}$	Heat transfer rate	[W/m]
$\dot{Q}$	Heat transfer rate	[W]
R	Thermal resistance	[°C/W]
Ri	Richardson number	[-]
Re	Reynolds number	[-]
u	Fluid velocity	[m/s]
SP	Turbine size parameter	[-]
T	Temperature	[°C]
ts	Solar time	[hours]
V	Velocity	[m/s]
V_r	Turbine volume flow ratio	[-]
$\dot{W}$	Power	[W]
x	Function of day number N	[°]
α	Absorptance	[-]
δ	Declination angle	[°]
ε	Emissivity	[-]
η	Efficiency	[%]
θ_i	Angle of incidence	[°]
θ_z	Zenith angle	[°]
∅	Latitude	[°]
μ	Dynamic viscosity	[kg/(m.s)]
ν	Kinematic viscosity	[m^2/s]
ρ	Density	[kg/m^3]
τ	Transmissivity	[-]
ω	Hour angle	[°]

Subscripts

a	Absorber
air	Air
an	Annulus
ap	Aperture
avg	Average
bulk	Bulk
b,n	Beam normal
C	Condenser
c	Cover
cl	Clean mirror
comp	Components
cond	Conduction
conv	Convection
cr	Critical
da	Dirt on receivers
Dis	Discharged
dm	Dirt on mirrors
Dump	Dumped
e	Electrical
eff	Effective
evap	Evaporator
F	Fan
film	Film
gain	Gained
gen	Generator
ge	Geometrical
gross	Gross
HTF	Heat transfer fluid
i	Inlet conditions

ia	Inner absorber tube
ic	Inner cover of absorber tube
is	Isentropic
L	Loss
max	Maximum
m	Mean property condition
net	Net
o	Outlet conditions
oa	Outer absorber tube
oc	Outer cover of absorber tube
opt	Optical
PT	Parabolic trough
PB	Power block
plant	Plant
pump	Pump
rad	Radiation
ref	Reflector mirror
rec	Recuperator
SF	Solar Field
sh	Shadow
sky	Sky
sol	Solar
T	Turbine
th	Thermal
tr	Tracking
un	Unaccounted
wall	Wall

1 Introduction

1.1 Research background

According to scientific research the main cause of global warming is the human exacerbation of the greenhouse effect. Fossil fuels produce 80 % of the world's current energy requirements and the energy demand is expected to increase by 61 % leading up to 2050 (IEA & IRENA, 2017). The environmental effects can become catastrophic if fossil fuels usage is continued at the current extent. During the COP21 conference in Paris a long-term goal was set to keep the average global warming below 2 °C. However, parties were urged to pursue efforts to limit it to 1.5 °C (C2ES, 2015). The International Energy Association (IEA) contributes to this goal by attempting to decarbonise the entire energy system and set certain goals for the renewable energy sector (IEA, 2014).

According to World Economic Forum (2018), a fifth of the current global energy is produced by renewable energy sources. From 2015 to 2016 solar power provided 50 % of all newly installed renewable energy capacity. It was also the first time in history that the added solar capacity exceeded all other electricity-producing technology. Wind power provided 33 % of newly installed renewable energy capacity followed by hydro power giving 15 % (World Economic Forum, 2018). Solar power is definitely on the fore front of renewable energy installations and the IEA set a goal in their latest roadmap specifically for concentrated solar power (CSP). With CSP having 5133 MW installed capacity at the end of 2017 (Helios CSP, 2018), the goal is to reach a global capacity of 1000 GW at 2050, (IEA, 2014).

Taking into account the large decrease in the price of photovoltaic technology price over the past decade, CSP technology must yet prove itself to the energy sector by highlighting the real value of CSP. Stakeholders are gaining confidence in the value of CSP as the technology is proving to offer a non-intermittent solution to help supply the ever-growing energy demand. Contributing factors include the vast amounts of research aimed at developing cost effective thermal energy storage (TES) and the successful implementation of various CSP systems. CSP developments are typically larger than 50 MW_e and feeds into the national grid.

The critical barrier to the widespread usage of off-grid small-scale CSP (500 kW_e – 5 MW_e), is the lack of optimised and economically competitive technology. Small-scale consumers that want to utilize off-grid energy sources are often left reliant on fossil fuels (like diesel generators) during night time. Other renewable technology are intermitted power supplies and storing electrical energy at this scale becomes impractically expensive hence small-scale CSP can be a solution.

1.2 Motivation

The effect of deploying small-scale CSP reaches far beyond just the climate and environmental benefits. In South Africa the mining-, construction-, auto-, metal- and engineering sectors contribute about 20 % of South Africa's gross domestic product, hence making it important to sustain these industries (SEIFSA, 2016). These industries are very reliant on energy and the widespread load shedding in 2015 left various concerns about the reliability of grid-offered energy. These industries are typical small-scale users that might be interested in a reliable, renewable energy source in order to hedge themselves against energy uncertainties for future developments. A reliable small-scale renewable energy alternative can be a key contributor in securing economic growth in South Africa.

In large scale CSP plants water is an excellent working fluid choice because high temperature energy resources benefits steam Rankine cycle efficiencies. The thermodynamic properties of steam however prohibit water being used as suitable working fluid in lower temperature and lower power output applications (Macchi & Astolfi, 2017). Andreasen et al. (2017) also concluded in a comparative study between working fluids that the use of steam greatly limits the design of high-efficiency turbines for low power output applications. The study highlighted that single-stage steam turbines are impractical solutions due to high supersonic flows at stator exit and rotor inlet, high liquid content at turbine exit, high volumetric ratios between inlet and outlet conditions and high peripheral speed. In order to achieve high efficiency values, a high number of stages is required. This makes steam turbines a complex and capital intensive solution for small-scale power applications.

Contrary to the above, organic Rankine cycles (ORC) are designed specifically to produce power within the lower temperature and lower power output ranges in a technically and economically feasible manner. For the power output range of 500 – 1000 kW ORC turbines can achieve thermal efficiencies of up to 85 % compared to the lower values of steam turbines ranging from 52 % - 71 % depending on the number of stages and turbine configuration (Andreasen et al., 2017). A promising advantage of coupling an ORC instead of a steam Rankine cycle with CSP, is that less and cheaper components are needed due to lower temperatures and cycle simplicity.

The successful completion of the 1 MW_e solar integrated organic Rankine cycle (SORC) plant in Arizona, USA in 2006, leads to a resurgence of interest in the research and development of small-scale SORC's. If SORC's can prove to be as a reliable and bankable replacement for fossil fuels in off-grid scenarios, the argument supporting the value of CSP will be strengthened. SORC's can then form part of the solution to secure a sustainable energy future. The future of electricity generating Rankine cycles coupled with CSP may subsequently cover the whole spectrum of energy requirements as proposed in figure 1.

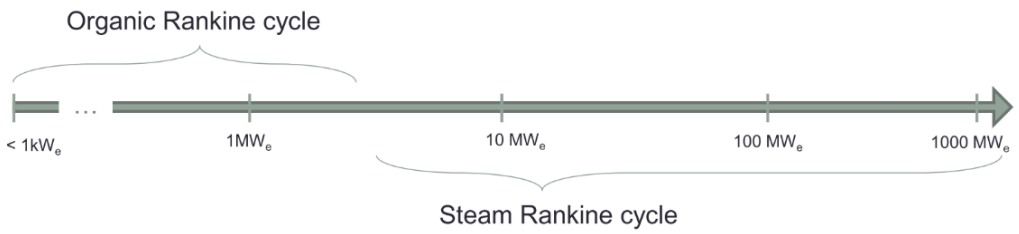

Figure 1: Proposed range of Rankine Cycles, adapted from (Dickes, 2016)

1.3 Objectives

The main goal of this research is to determine whether the integration of an ORC, with a smaller CSP system can result in a feasible solution for off-grid applications. The SORC gross power output range of 500 kW_e – 5 MW_e is considered for a specific location and industry in Southern Africa. Even though the economics will play a role in the study, the focus will be on the technical aspects.

The objectives of the research are:

- Determine the technological maturity and technical feasibility of integrating ORC technology with the small-scale CSP.
- Identify an industry and site in Southern Africa as case study for the proposed SORC.
- Analyse and simulate a SORC plant to component level. The first simulation is to determine the design point of the plant. The second simulation is an annual simulation for the identified site.
- Perform a high level economic analysis of the SORC in order to determine the economic competitiveness of the technology.

1.4 Thesis layout

Chapter 1 introduces the background information leading up to the research problem. The research was further motivated and it was demonstrated how a SORC fits into the larger picture in securing a sustainable energy future. The objectives of the research were clearly defined.

Chapter 2 consists of a literature study and starts with giving an overview of ORC's and CSP to gain an understanding of these types of technology. The chapter continues by looking at the status of SORC's and gives a technical overview of the technology. The chapter ends off by drawing conclusions on the technological maturity and technical feasibility of integrating ORC technology with the small-scale CSP.

Chapter 3 goes through the process of identifying an industry for the possible deployment of a small-scale SORC and ends off by identifying a specific site.

Chapter 4 analyses the theory of all the functioning units in the SORC plant namely the solar field, storage and power block. The analysis goes to component level and provides the theory for the simulations in the following chapters.

Chapter 5 describes the first simulation to obtain the design point of the SORC plant for the specific location. The simulation methodology is carefully described, and all the input parameters of the simulation are tabulated.

Chapter 6 describes the annual simulation of the SORC plant. The simulation results are shown, and the high-level economic analysis follows.

Chapter 7 is the concluding chapter with a summary of the research and the main results. The chapter gives an overall conclusion on the research question as well as recommendations on future work.

2 Literature Study

The literature study aims to broaden the understanding of an SORC and concludes on the technological maturity and technical feasibility of integrating an ORC with small-scale CSP. In this chapter, an overview of ORC's and CSP is given in their respective fields. The discussion continues to look at the status of SORC's whereafter a technical overview of SORC's is given. The chapter ends off by looking at the South African context.

2.1 Introduction to SORC's

2.1.1 ORC overview

Even though steam Rankine cycles are more commonly used, the usage of organic fluids as working fluid is not a new concept. In 1826, Thomas Howard patented the first concept of an engine using ether as a working fluid, but the first commercially used organic fluid was Naphtha in 1890 where the Gas Engine & Power Company of New York claimed to have sold five hundred of these engines. (Casati, 2014).

The first operational solar ORC was built by Frank Shuman in Philadelphia USA in 1907 and was rated at 2.5 kW thermal output. With the 100 m^2 collector area, direct vapour of Ether at 115 °C was used to drive an irrigation pump (Shuman, 1907). Another organic fluid namely Diphenyl oxide was also reportedly used in 1926 in a Rankine cycle (Curran, 1981). The first solar to electric application of an ORC came in 1961 when Israeli engineer Harry Zvi Tabor, alongside his partner Lucien Bronicki developed an ORC turbine. This was the first turbine to operate at low temperatures. Cheap fossil fuels prevented the widespread usage of this turbine but Bronicki went on to later find Ormat Industries that still develops and manufactures turbines to date (Keighley, 2013).

The commercial use of ORCs originated primarily from geothermal resources in the 1970's (Southon, 2015). Currently ORC technology is used in a variety of industries mostly because of the modularity and versatility seeing that the technology can be used at a wide range of temperatures (Vélez et al., 2012). When referring to the industries using ORC technology, it can be divided into two categories. Firstly the heat resource and secondly the output application. Figure 2 shows the most common heat sources for an ORC system and the different output application industries are summarised in figure 3.

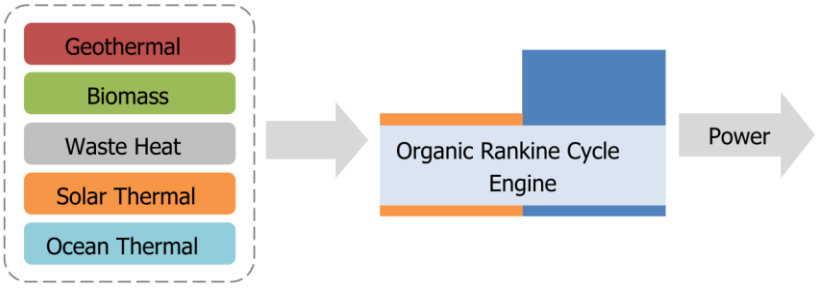

Figure 2: ORC heat resources, adapted from (Southon, 2015)

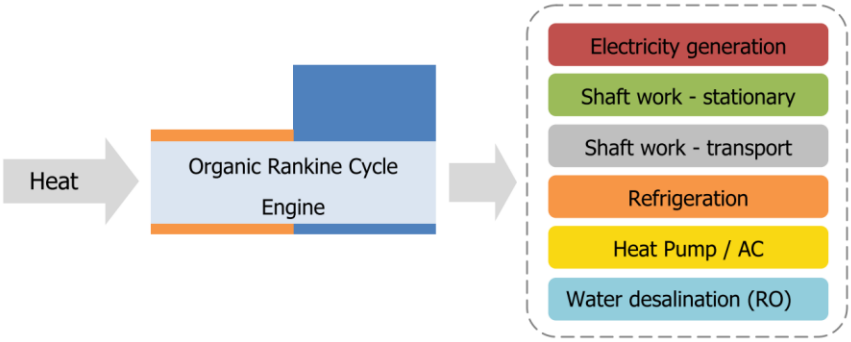

Figure 3: ORC output application industries, adapted from (Southon, 2015)

At the end of 2016, the ORC market reached a total installed capacity of 2701 MW distributed between 1754 ORC plants. Referring to figure 4 (a), geothermal applications is the market dominating heat source for ORC plants and accumulates to almost 75 % of installed capacity (Tartière & Astolfi, 2017). ORC geothermal plants vary from 200 kW_e to the largest being the 88 MW_e plant named Ngatamariki in New Zealand (Southon, 2015). These plant sizes vary greatly because the temperature range of geothermal sources can range from a few tens of degrees up to 300 °C (Quoilin, 2011). Due to the multi-MW scale of geothermal plants, the number of plants is relatively low with only 337 installations. The market share per heat source and per manufacturer are shown in figure 4 (a) and figure 4 (b) respectively.

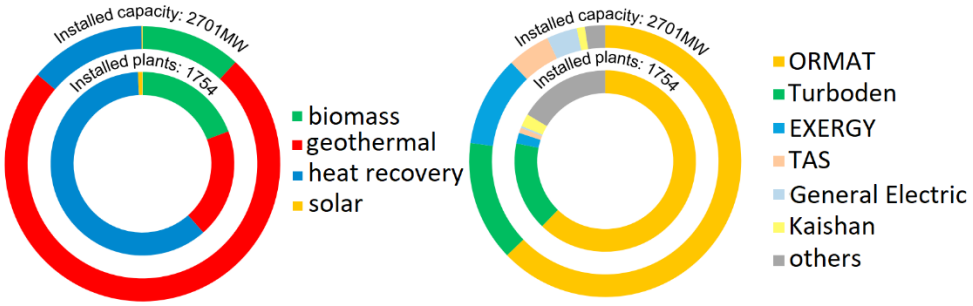

Figure 4: Total installed capacity per heat source (a) and per manufacturer (b) (Tartière & Astolfi, 2017)

Waste heat recovery is the second most utilised heat source by ORC plants with about 14 % of total installed capacity. Waste heat recovery accounts for a large number of plants as about 800 of these units installed by ORMAT are smaller than 4 kW_e (Tartière & Astolfi, 2017). Biomass accounts for the third largest industry with a market share of about 11 %. The cost is significantly lower than fossil fuels but a great investment cost is needed to achieve the clean biomass combustion needed for the boiler. To make the biomass ORC plants economically viable, combined heat and power is required but the plant is driven by an operating strategy bias to the heat requirement (Quoilin et al., 2013). Turboden is the largest ORC manufacturer in the biomass industry with 228 plants at present and many more under construction (Tartière & Astolfi, 2017).

Solar applications are almost negligible in comparison to the total market share of ORC's. Two main possibilities of integrating solar energy with an ORC exist. The first is reversible ORC/heat pump units powered by solar thermal roofs and the second is CSP systems for power generation (Quoilin et al., 2015), (Southon, 2015). This thesis focuses on the latter case of integrating an ORC with CSP.

It can be concluded that ORC as technology has been established in the general market and that there are a number of companies driving the development of this technology. It became clear that the ORC technology is yet to be proven in the solar specific industry but the advantage for the solar thermal industry is that other industries are developing and optimising technology that can be easily implemented in the solar thermal field. On the other hand, as the solar thermal industry develops and optimises solar collectors for other thermodynamic cycles, the point could be reached where CSP and ORC can be combined in an economical way.

2.1.2 CSP technology

The rate at which incoming solar energy reaches the earth's surface is called the solar irradiance or insolation and is measured in Watts per metre squared (W/m^2). Just outside the earth's atmosphere, the average solar irradiance is 1367 W/m^2. Designers are often interested in knowing how much solar energy falls on a certain area over a period of time and this summation of solar energy is called solar radiation or irradiation and is measured in Watt-hours per square meter (Wh/m^2) (Stine & Geyer, 2001). The solar irradiation can be divided into three components where the beams coming directly from the sun's disc are referred to direct normal irradiation (DNI), the scattered solar irradiance which seemingly comes from all directions is called the diffuse horizontal irradiation (DHI) and lastly the combination of DNI and DHI forms what is referred to as global horizontal irradiation (GHI). CSP systems can only harness the sun's energy in the form of DNI while solar photovoltaic panels absorb the sun's energy in the form of GHI.

CSP plants concentrate solar rays onto what is called the receiver, to heat up a fluid that in turn, with direct or indirect means run a turbine. The turbine is coupled with a generator that then generates electricity. One of the main advantages of CSP power plants compared to other renewable energy sources is the fact that a system can be integrated with a comparatively inexpensive thermal energy storage system. Energy is stored in the form of heat, most often in a molten salt solution. The main solar concentrating technologies are the linear Fresnel reflector, central receiver tower, parabolic dish and parabolic trough (PT) and these technologies are depicted in figure 5.

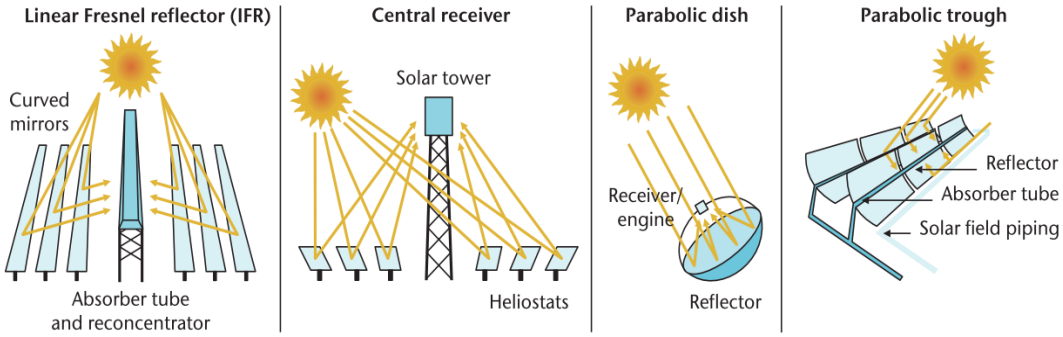

Figure 5: Main CSP technologies (IEA, 2014)

Parabolic dishes and central receiver towers have the highest concentration ratios leading to the high temperatures typically obtained by these types of technology. Central receivers are still a leading type of CSP technology. In terms of total installed capacity, Ivanpah Solar Electric Generating System located in Nevada, USA is the largest CSP plant. The plant consists of three central receiver towers each with its own turbine. Combined the plant gives a net power output of 377 MW_e (NREL, 2014). Parabolic dishes have almost disappeared from the commercial energy landscape because it has not proved possible to reduce the higher cost and risks associated with the technology. It also does not easily lend itself to storage (IEA, 2014).

Linear Fresnel reflectors (LFR) are also used on commercial size scale. Examples are the 30 MW_e plant running in Calasparra, Spain and the 125 MW_e plant built in Rajasthan, India. LFR's use flat mirrors and have the advantage over PT's that they are easier and cheaper to manufacture. The disadvantage compared to troughs, is the optical loses the plant experiences when the sun is low in the sky in the mornings and late afternoons. All LFR plants currently use direct steam generation, (IEA, 2014).

One small PT plant in Thailand also uses direct steam generation but PT plants are mainly coupled to traditional steam Rankine cycles for power generation, working at temperatures between 300 °C to 400 °C (Quoilin, 2011), (IEA, 2014). PT plants require high temperature and high pressure to increase efficiency but this leads to expensive component investment costs. There is a natural temperature limit

imposed by the sun's energy and in order for the plant to be profitable, high power output needs to be obtained (Quoilin, 2011). ORC seems to be a promising technology because a plant operates at much lower temperature and pressure and this significantly decreases the investment costs. The power output of such an ORC plant is however limited to a small-scale.

2.1.3 Current status of SORC plants

An example of an attempt to lower the investment cost of solar ORC was first seen in 1985 in Beith Ha'Arava, Israel. Engineers replaced the solar collectors with the newer concept of a solar pond. The pond works on the inversion effect where a mass of water can be hotter at the bottom than at the top by inhibiting natural convection. A further increase in temperature gradient is forced by the salt gradients present. Temperatures of up to 96 °C are reached at the bottom of these ponds. Heat is then extracted by pumping the brine through radial funnels to heat the thermodynamic working fluid of the ORC. Another realised advantage of this technology is the fact that the solar pond provides a large built in storage. This Israeli Solar Pond Power Plant used a 5 MW ORC turbine supplied by ORMAT and the power plant operated from 1985 until 1989. With thermodynamic conversion efficiencies of 5.5 % and an overall sun to electrical efficiency of under 1 % the plant was closed down because the power produced was not economically competitive with the cheap fossil fuels available at the time (Tabor & Doron, 1990), (Dickes, 2016). This however is unique to the high salinity of water from the Dead Sea and it is unlikely to be replicated elsewhere.

The first commercial SORC plant is the 1 MW_e APS Saguaro PT plant in Arizona, USA completed in 2006. The plant has 10 340 m^2 of PT collectors using thermal oil at 300 °C as heat transfer fluid in the solar field. The ORC module uses n-pentane as working fluid with a 1 MW_e turbine supplied by ORMAT. A major increase in efficiency was seen with an overall solar to electrical efficiency of 12.1 % at design point. This is still the largest operating SORC plant in the world to date and a pioneer in SORC technology as it proved the simplicity of an ORC compared to that of a conventional steam Rankine cycle as this plant even allows for unattended operation. All of which are important factors in the economic considerations and commercial acceptance of this technology (Canada et al., 2005), (Dickes, 2016), (Quoilin et al., 2013).

In December 2009 another SORC plant was inaugurated in the Kona Desert at the National Energy Laboratory of Hawaii Authority (NELHA) in Hawaii. This project named the "Holaniku at Keahole Point" uses PT collectors. Sources differ about the output of the plant but most agree that it has an installed thermal capacity of 2 MW and an output of 500 kW_e (PowerTechnology, n.d.), (SolarServer, 2010), (SOPOGY, 2013), (Nelson & Starcher, 2011), (Kalaiselvam & Parameshwaran, n.d.) . The solar field uses thermal oil that is heated up to 200 °C when entering the power block. The power block consists of a closed loop ORC supplied by ElectraTherm, using a twin screw expander to power the

generator. The plant incorporates 2 hour TES and at present the plant produces an average of 4 GWh electricity per year. The plant uses a total of 1.5 ha of land and unfortunately no information was available about the overall plant efficiencies. (SOPOGY, 2013).

In Ait Baha Morocco a cement plant has been operating since 2010 and produces 5000 tons/day. It was using coal as its main fuel and had an existing ORC running from waste heat of the cement production process (Ojan, 2015). In 2014, a CSP system was installed to provide auxiliary heat to the ORC complementing the waste heat. The solar field consist of PT air receiver built by Airlight Energy with a 3.9 MW_{th} peak thermal output. These receivers are quite revolutionary in their designs and various studies found interest in their working (Good et al., 2013). Air enters the solar field at 270 °C and exits at 570 °C. Incorporated in the solar field is a packed-bed rock storage with 5 hour TES (Airlight Energy, 2015). A schematic layout of the plant can be seen in figure 6.

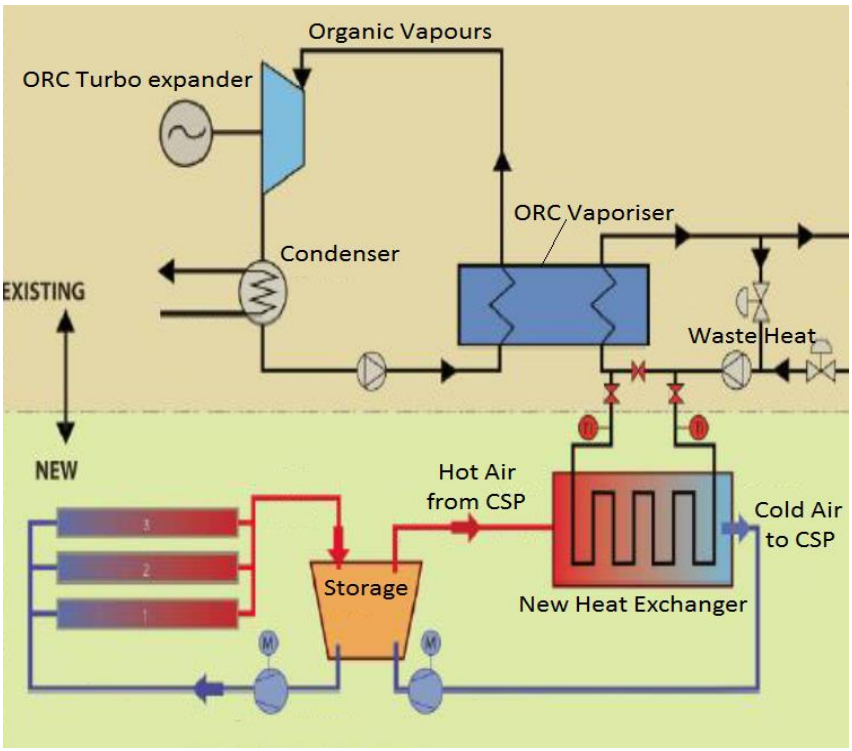

Figure 6: ORC plant layout, adapted from (Ojan, 2015).

The hot air from the storage enters a heat exchanger where more heat is added to industrial waste heat coming from the cement production plant before going to the evaporator of the ORC. The ORC working fluid reaches a temperature of about 200 °C. The power block has a turbine with 2 MW_e designed output supplied by Turboden.

Also in Morocco at Benguerir known as the Green Energy Park of the Research Institute for Solar Energy and New Energies, a 1 MW_e ORC plant manufactured by ENARRAY is under construction but the plant does not include TES (Gaggioli, 2016a), (IRESEN, 2016b) and (IRESEN, 2016a). Further development of this plant is planned with another project called the ORC-Plus project. The ORC-Plus project is a 6.4 M€ initiative funded by the EU Commission under the framework programme Horizon 2020. The project aims at developing an optimized combination of innovative TES and engineering solutions necessary to improve the dispatchability (production on demand) of an existing SORC (ORC Plus, 2015).

The current ORC plant as well as the planned ORC-Plus project uses type FLT Soltigua LFR's with a net collecting surface of 11 434 m^2. The HTF named DelcoTermSolar E15 that is used is a paraffinic based oil with minimal environmental impact. The solar field will have working temperatures ranging between 180 °C and 300 °C. The ORC power block uses a 1 MW_e rated Exergy radial outflow turbine and an air cooled condenser (ACC) (Gaggioli, 2016a). The 20 m^3 storage tank will provide 4 hours of full load production after sunset (Gaggioli, 2016b). The completed plant will serve as a pilot plant to validate the technology in a real operational environment and demonstrate its feasibility in increasing the dispatchability of CSP plants and lowering the levelised cost of electricity (LCOE) (IRESEN 2016a). In figure 7, a schematic layout of the plant upon completion is shown.

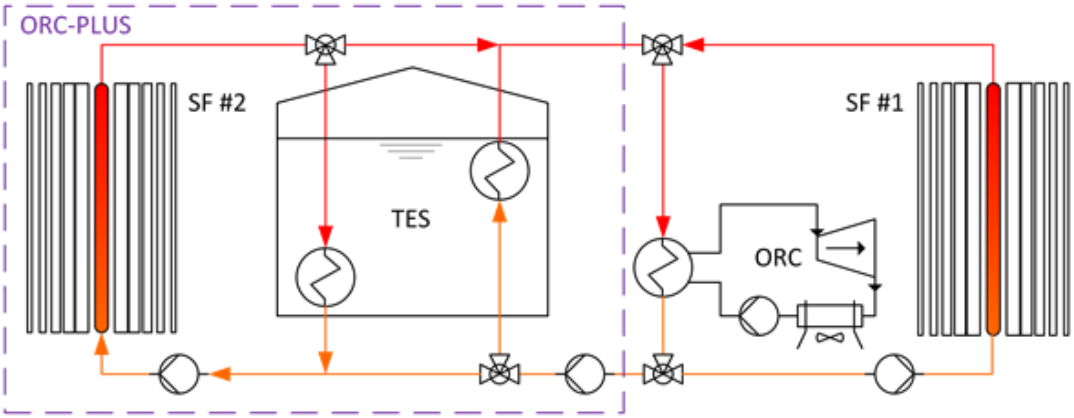

Figure 7: ORC Plus pilot plant layout (ORC Plus, 2015)

These are the only operating and developed SORC plants. The conclusion is that the combination of CSP and ORC as technology in the range from 500 kW_e – 5 MW_e is immature. This leads to investment and development being slow as this technology has yet to prove successful whereafter widespread deployment will take place. A trend can be seen on the other hand with the increased interest in SORC over the past ten years.

On a micro scale (<10 kW) a few developments are taking place. The best documented is the 1 kW SORC plant installed in Lesotho in 2007 for rural electrification. The work was done by a collaboration between Massachusetts Institute of Technology, University of Liege, STG International and the Government of Lesotho. The plant uses a simple ORC without regeneration therefore the plant is robust and cheap. This is achieved by using and modifying commercial HVAC compressors and heat exchangers with a scroll expander and an overall efficiency of about 5 % is achieved (Orosz, 2009), (Quoilin et al., 2011), (Quoilin et al., 2013), (Quoilin & Lemort, 2009), (Tchanche et al., 2011), (Giovannelli, 2015), (Wang et al., 2013), (Kim & Han, 2015).

Other smaller SORC applications include the 10 kW power output plant running with an overall efficiency of 4.7 % operating off-grid in Indonesia since 2012 (Pikra et al., 2013), (Kim & Han, 2015). In 2012 the University of Louisiana in conjunction with CLECO Power LLC, constructed a 50 kW pilot scale PT trough Plant in Louisiana. The plant uses an ORC power block provided by ElectraTherm. The working fluid of the ORC is R245fa where the heat exchanger operates at 93 °C inlet and 121 °C outlet temperature. The plant had an overall efficiency of 6 % (Raush et al., 2013), (Desai & Bandyopadhyay, 2016). Granite Power completed a pilot SORC plant in 2014 that can generate up to 30 kW of electricity with 1 hour TES. They claim they have developed a high efficiency version of the ORC but no information on their operating efficiencies are available (Berlin, 2014).

2.2 SORC technical overview

2.2.1 Working fluids

The ORC is conceptually the same as a traditional steam Rankine cycle in the sense that it is based on the vaporization of high pressure liquid which is in turn expanded to a lower pressure to generate mechanical work. The difference is that an organic component is used as working fluid instead of water and thereby allowing for a more efficient system at these lower temperatures. Various organic components are available but it is typically a refrigerant, hydrocarbon, silicon oil or a perfluorocarbon that is used (Quoilin, 2011).

Working fluids can be categorised according to their saturation vapour curve. Three basic types of working fluids namely wet, dry and isentropic fluids can be categorised and the distinction between them are drawn regarding the vapour slope of the saturation curve. Referring to figure 8, wet fluids are classified by having a negative saturation curve slope, isentropic fluids have an infinite slope and dry fluids have a positive slope. Examples of wet fluids are water and ammonia; organic fluids are either dry or isentropic fluids.

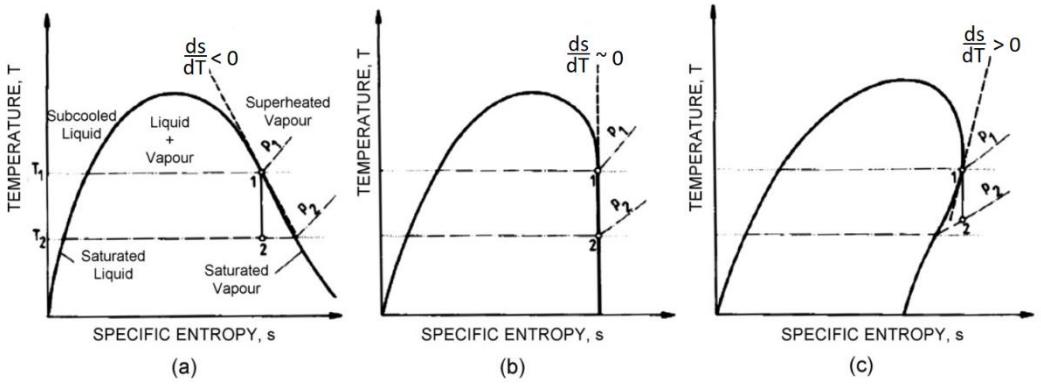

Figure 8: T-S diagram of fluids (a) wet, (b) isentropic and (c) dry, (Badr et al., 1985)

For wet fluids, a superheater is required to superheat the vapour and this increases the system cost. Since ORC's focuses on lower heat sources the superheating of the vapour, as in the case for steam Rankine cycles, is not necessary (Vélez et al., 2012). If the wet fluid is expanded (between points 1 and 2) without superheating, the vapour falls in the liquid/vapour area and the condensate so formed can cause damage to the turbine. The same is not true for the organic fluids as it can be seen that the fluid still falls in the vapour region after the expansion process without being superheated before the expansion process, hence no vapour condensation happens in the turbine (Delgado-Torres & García-Rodríguez, 2010).

Another advantages of organic fluids over water, is the higher molecular weight associated with organic fluids. A further comparison between steam and organic fluids as working fluids can be seen in table 1.

Table 1: Comparison between ORC compared to steam Rankine cycles, (Southon, 2015)

Advantages of ORC's	Disadvantages of ORC's
Choosing a working fluid with a low boiling point can allow for economic conversion of low-temperature heat sources.	Working fluids are more expensive and often less chemically stable and environmentally friendly than steam.
Choosing a dry, high molecular weight working fluid can eliminate expensive superheating or reduce turbine strength requirements.	At high temperatures, complex steam cycle systems are capable of higher efficiency than current ORC designs.
Fluids with high vapour densities can lead to smaller turbine and piping requirements.	ORC fluids often have poorer heat transfer properties, requiring a larger heat exchanger than an equivalent steam system.
No need for de-aeration and demineralisation processes, and non-condensable gases removal systems are often simple.	ORC fluids often are more viscous, leading to higher pumping work and piping size requirements.

Advantages of ORC's	Disadvantages of ORC's
Condensing pressure is often higher than atmospheric, reducing need for seals to be able to prevent air infiltration.	ORC fluids often have a lower latent and specific heats than water, requiring larger mass flow rates. This leads to larger pipe, heat exchanger and pump requirements.
Evaporation pressure can be lower than steam cycles, reducing the strength requirements of some components and sometimes removing the need for an on-site operator.	There is less design experience and expertise for ORC turbines than steam turbines.
Turbine designs can often be of lower complexity due to lower pressure ratios and fewer stages.	
ORC working fluids with a small density difference between vapour and liquid do not need steam drum or recirculation components.	

It can be concluded from table 1 that the application of water and organic fluids are different. Ultimately, the type of working fluid that would be selected also depends on the temperature range at which the ORC would be operating as fluids are limited by their own fluid- and thermodynamic properties. Figure 9 gives an indication of typical temperatures at which the most common types of fluids can be used.

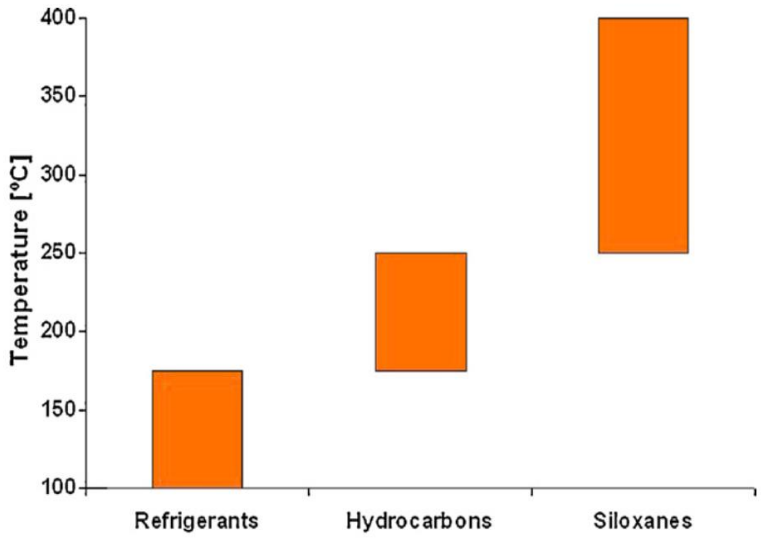

Figure 9: Classification of working fluids according to their temperature ranges**,** (Vélez et al., 2012)

A summary of the thermochemical properties of the most commonly used organic fluids can be seen in table 2.

Table 2: Estimated maximum functional temperature for most commonly used organic fluids, (Macchi & Astolfi, 2017)

Fluid	T_{max} (ºC)	T_{cr} (ºC)	P_{cr} (bar)	T_B
Hydrocarbons				
Pentane	300	196.55	33.7	36.06
Cyclopentane	300	238.54	45.15	49.25
Toluene	350-400	318.6	41.263	110.6
Chlorobenzene	320	359.5	45.191	131.75
Biphenyl	400	499.85	33.8	255
Diphenyl oxide	400	493.65	30.8	258
Downtherm A	400	497.2	31.34	257
Fluoro-compounds and refrigerants				
R134a	350-370	101.06	40.593	-26.07
R245fa	300	154.01	36.51	15.14
R23	400	25.86	48.2	-82.1
R32	570-590	78.4	57.8	-51.65
Fluorinol 85	250-300	233	55.2	75
Perfluorohexane	400	175.55	18.7	56.6
Perfluoropropane (R218)	500	71.85	26.75	-39
Hexafluorobenzene	350-400	243.58	32.75	117.96
Siloxanes				
Linear (MM…MD_2M)	300	245.6; 326.25	19.39; 12.27	100.52; 194.35
Cyclic (D_4…D_6)	350	313.35; 372.63	13.32; 9.61	175; 244.99
Some inorganics and organic compounds				
Pyridine	350-400	346.8	56.3	115.2
Carbon dioxide	650-700	30.98	73.77	N/A
Titanium tetrachloride	550	365.95	46.61	134.8

No working fluid is optimal for all applications. Many studies over different applications have proved and the study of working fluid candidates must be integrated into the design process of a specific application. (Quoilin & Lemort, 2011). The thermodynamic and physical properties of working fluids are what differentiate it the most. For example the greater the latent heat and molecular weight of the fluid, the more energy the fluid can absorb during the evaporation process. This results in smaller pumps and decreases costs due to the decreased flow rate (Vélez et al., 2012).

The relationship between working fluid properties and thermodynamic cycle performance are discussed below:

- *Thermal stability*: The thermal stability of the fluid that is used can limit the temperature of the heat source because fluids can chemically brake down certain temperatures. This alters the way the cycle operates and can result in toxic and irritating compounds which can induce health problems if leaked (Vélez et al., 2012).

- *Vaporization latent heat:* Also referred to as enthalpy of vaporization, the higher the vaporization latent heat, the more available heat can be added to the working fluid in the heat exchanger. This effect decreases the necessity of regulating the superheating and expanding of the vapour through regenerative feed heating in order to obtain higher efficiencies (Maizza & Maizza, 2001). In terms of work output it has been found that for the same defined temperatures, a larger unit work output is produced with working fluids with a higher vaporization latent heat (Chen et al., 2010) in (Bao & Zhao, 2013). The scenario looks different for the case where the heat source is of varying temperature. Larjola (1995) in Bao and Zhao (2013) found that the temperature profile of the working fluid better follows the temperature profile of the heating fluid in the evaporator therefore fluid with a lower vaporization latent heat is desirable with a heat source of varying temperature. Due to storage incorporated the current applications aim for a high vaporization latent heat.

- *Density:* Bao and Zhao (2013) states that a high vapour density is of key importance especially for working fluids with a low condensing pressure. A low density leads to higher volume flow rates which in turn lead to larger pressure drops in the heat exchangers and the bigger turbine sizes. All these have an adverse effect on the cost of the system. When looking at the isentropic efficiency that is described by the size parameter (SP) and the isentropic volume flow ratio or just volume flow ratio (V_r), both as defined in subsection 4.4.3, a lower value for SP is desired to decrease the turbine size. A higher density at the turbine outlet decreases the SP hence a higher fluid density is beneficial.

- *Specific heat:* A few researcher tried to propose relationships between the specific heat of the fluid and the required pump work (Chen et al., 2010), (Maizza & Maizza, 1996), (Papadopoulos et al., 2010) but Bao and Zhao (2013) concluded that there is no direct relationship between specific heat and specific or total pump work.

- *Critical temperature:* Bao and Zhao (2013) studied the effect critical temperature has on cycle performance and concluded that a fluid with a higher critical temperature results in higher overall cycle efficiency but lower condensing pressure. An adverse effect of working with high critical temperatures is that low vapour densities are involved.

- *Boiling temperature:* Mago et al. (2008) showed that the fluid with the highest boiling temperature, showed the best thermal efficiency. Bao and Zhao (2013) noted that that the study done by Mago et al. (2008) only considered a small number of working fluids and the results cannot be taken as absolute. Saleh et al. (2007) showed with a more comprehensive study that the above is only true when comparing working fluids out of the same family. The boiling temperature can be used as a relative indicator but it cannot be concluded that any one fluid will result in a higher thermal efficiency just because of a higher boiling temperature.

- *Freezing temperature:* The lowest temperature in the cycle must be above the working fluids' freezing point.

- *Molecular weight:* Bao and Zhao (2013) concluded that high molecular weight has a positive impact on turbine efficiency but it must be noted that fluids with a high critical pressure and high molecular weight require higher heat transfer area. In choosing a working fluid a higher molecular weight is still desired.

- *Molecular complexity:* Molecular complexity is directly related to whether a fluid is dry, wet or isentropic because of the definition given by Bao and Zhao (2013). As the molecular complexity increases, the vapour slope of the saturation curve becomes more positive. Some of the thermodynamic properties are directly influenced by the molecular complexity and as a rule for homologous fluids, the critical temperature increases with increasing molecular complexity whilst the critical pressure decreases. Molecular complexity will hence not be treated as an absolute criteria and as Bao and Zhao (2013) has shown, high molecular complexity can either have a positive or negative impact on cycle efficiency depending on a lot of factors (Bao & Zhao, 2013).

- *Viscosity:* In order to maintain low friction losses in the pipes and heat exchangers, low viscosity is desired in both the liquid and vapour phase (Bao & Zhao, 2013).

- *Conductivity:* In order to obtain a high heat transfer coefficient in the heat exchangers, a high conductivity is required (Bao & Zhao, 2013).

These above discussed thermodynamic and physical properties of working fluids are used in subsection 4.4.1 in a weighted decision analysis to determine the working fluid that is best suited for small scale SORC systems.

2.2.2 Thermodynamic cycle

A few thermodynamic cycles have been proposed in literature to convert low-grade heat into electricity. They include the supercritical Rankine cycle, trilateral flash cycle, Kalina cycle and the ORC. When considering the supercritical Rankine cycle's high operating pressure, the trilateral cycle's difficult two-phase expansion and the Kalina cycle's complex system structure, the ORC remains the better option with its high reliability, low maintenance and simple cycle structure (Bao & Zhao, 2013). An ORC with an internal heat exchanger or also referred to as a recuperator is shown in figure 10.

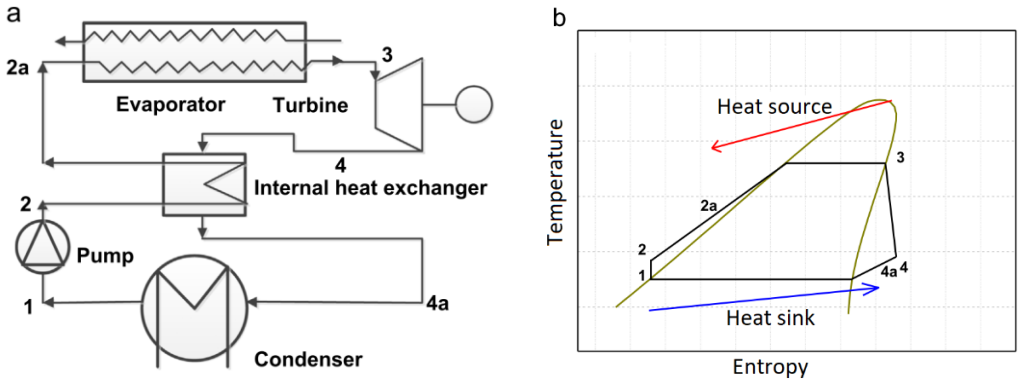

Figure 10: Organic Rankine cycle with internal heat exchanger schematic and T-S diagram, (Li, 2016)

The fact that an ORC per definition works with lower temperature differences is the reason for the typical low efficiencies of ORC's. However, there are still ways whereby the thermal efficiencies can be improved. The matter to consider would be if the cost of the added means of increasing thermal efficiency would justify the gain of increased thermal efficiency. Even small increases in thermal efficiency can mean large savings in money. The two basic principles to increase thermal efficiency are (Çengel & Boles, 2011):

- Increase the average temperature at which heat is transferred to working fluid in the evaporator.

- Decrease the average temperature at which heat is being rejected from the working fluid in the condenser.

When considering the internal heat exchanger, it is evident that the working fluid absorbs heat from the exhaust vapour coming from the turbine. This raises the temperature at which heat is added to the working fluid in the evaporator. The result then is a raise in the working fluid's enthalpy at the evaporator entrance. For the same net power output as the baseline cycle, less heat is added to the working fluid which increases the thermal efficiency for the case with the internal heat exchanger (Li, 2016).

For an ACC the only way to reduce the condensing temperature is to decrease the initial temperature difference between the ambient air and the condensing vapour. The cost of an ACC increases as the initial temperature difference decreases therefore an optimum trade-off exists for each system.

2.2.3 ORC turbines

The turbine is the key component in an ORC and has the largest effect on cycle efficiency. It has the function of converting the working fluid's kinetic energy into rotary mechanical energy, which is in turn converted to electrical energy by the generator coupled to the expander via a shaft. Depending on the size of the plant and working fluid, the turbine type varies over a large range of possibilities. Turbines can be divided in two main categories namely turbomachines and volumetric expanders (Macchi & Astolfi, 2017), (Quoilin & Lemort, 2011). Turbomachines are commonly referred to as turbines where volumetric expanders are referred to as expanders, but the terms are used interchangeably. Volumetric expanders are in effect a positive displacement machine where pockets of fluids are trapped during rotation, expanded and then discharged.

Scroll and screw expanders are generally used for applications where an output of less than 100 kW_e is needed. For larger power outputs turbomachines are more suitable and their typical power output range is between 100 kW and 15 MW. Depending on the relative motion of the working fluid to the turbine's shaft, turbomachines can be categorized in three main categories namely axial, radial inflow or centripetal and radial outflow. For a power output of higher than 0.5 MW an axial turbine is the most common choice in ORC's and is developed by both Turboden and Ormat (Macchi & Astolfi, 2017). Because the enthalpy drop is much lower for organic fluids during expansion, fewer stages are required on a turbine used in an ORC. Single-stage axial turbines can even be used for low temperatures ORC.

With proper design, an axial turbine can fit practically any application. In the ORC field however, off the shelf components are not readily available because of the wide range of applications and different working fluids being used. Most ORC turbine designs are customized for the specific application. As a rule for ORC's, certain design decisions needs to be established prior to commencing with turbine design. This includes firstly selecting the working fluid and secondly the power cycle arrangement.

Various correlation diagrams and charts for the estimation of axial turbine efficiency are proposed in literature. Examples are the Baljé and Binsley plots (Binsley & Binsley, 1968) and the Smith charts (Smith, 1965), but they lack crucial variables relating to ORC applications. Because ORC's operate at lower temperatures and have a smaller enthalpy drop over the turbine, ORC turbines normally are more compact with fewer turbine stages and have low loading coefficients. Contrary to steam and gas turbines with higher temperatures and mechanical stresses, peripheral speed is not a critical issue for ORC turbines in determining the stage number. Design processes taking into account actual blade dimensions and Mach number effects are more crucial for ORC turbines designs where turbine blades are characterized by large height variation, large flaring angles and supersonic velocities (Macchi & Astolfi, 2017).

2.3 South African context

2.3.1 CSP in South Africa

South Arica is a third world country with a population close to 56 million people living in about 13.2 million households. Currently 75 % of households are electrified leaving about 3.3 million households without electricity and these are mostly in the rural areas, (Jamal, 2015). South Africa does have an extensive existing electrical grid and with the planned grid up until 2024 shown in figure 11, the electrification rate will increase over the next few years.

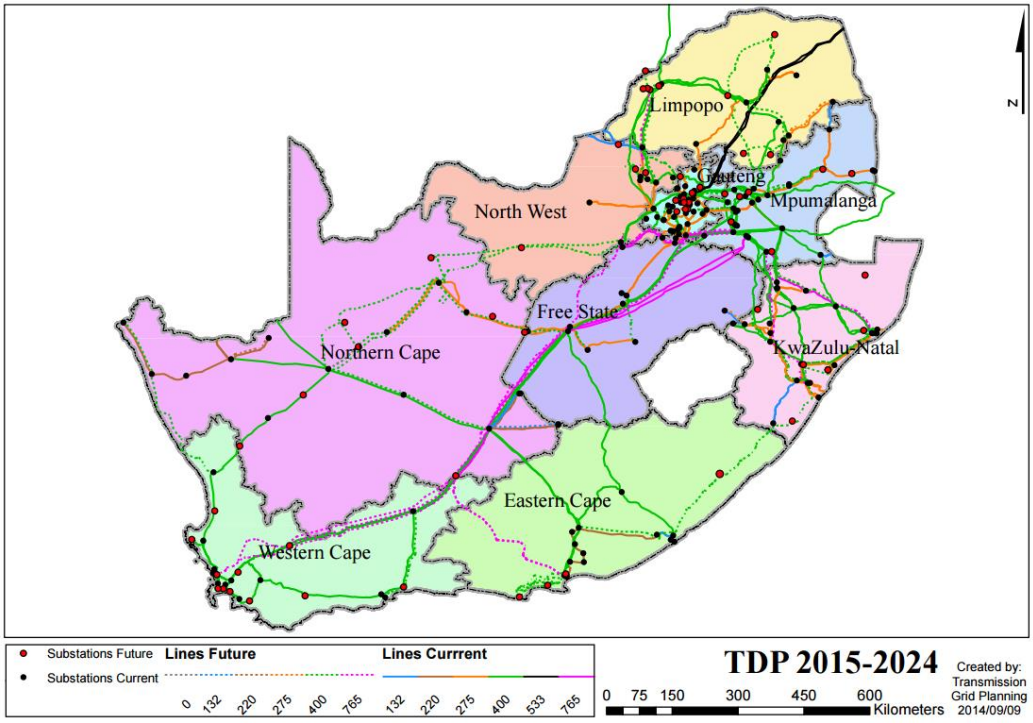

Figure 11: South Africa's national grid development plan 2015-2024, (Eskom, 2014)

The grid developed mostly around large cities and the coal fire power stations that still produce the majority of South Africa's electricity. Despite this well-developed electrical grid, there still exists a large energy deficit in South Africa especially in the rural off-grid areas.

The South African government introduced the Renewable Energy Independent Power Producer Procurement Programme (REIPPPP) to prioritise renewable energy. The government aims to achieve 17800 MW of renewable energy by the year 2030 that will make out 42 % of the total energy production Through the REIPPPP, the South African Department of Energy has rolled out four bid windows in order to achieve their renewable energy goal. From these bids the leading renewable technologies were solar PV and wind energy with CSP lagging behind them (T. O. Craig et al., 2017). A total of seven CSP projects were conceived from the REIPPPP bidding windows with an additional CSP plant being built apart from the program. More details relating to these eight CSP projects currently running in South Africa are given in table 3.

Table 3: CSP projects in South Africa, (Rycroft, 2018)

Project	Technology	Capacity (MW)	REIPPPP Window	Nearest Town	Status
Bokpoort CSP	PT	50	2	Groblershoop	Operational
Eskom CSP	Central receiver tower	100	Other	Upington	Planning
Ilanga CSP 1	PT	100	3	Upington	Construction
Kathu Solar Park	PT	100	3	Kathu	Operational
Kaxu Solar 1	PT	100	1	Pofadder	Operational
Khi Solar 1	Central receiver tower	50	1	Upington	Construction
Redstone CSP	Central receiver tower	100	3	Postmasburg	Planning
Xina CSP	PT	100	3	Pofadder	Operational
Total	**8**	**700**			

Kaxu Solar 1 was the first operational plant followed by Bokpoort and Khi. With the completion of all the CSP projects, South Africa will have a total installed capacity of 700 MW CSP.

According to T. O. Craig et al. (2017), CSP in South Africa face challenges that can be summarized in three aspects: Cost and funding, market and political will, and technology. The first two issues might arise due to the LCOE of CSP being high compared to other renewable energy technologies. (Dinter & Busse, 2015) however stated that a few issues have been raised regarding the use of LCOE as measure between technologies and that it does not consider the 'hidden benefits' of a technology. The hidden benefits typically include the lifetime of components and impact of temperature on performance. CSP has the further advantage of thermal storage that enables this technology to play an important role in any electrical network.

2.3.2 Possible industries for SORC Plants

The government plans to increase the electrification rate to 97 % in 2025 where 90 % of households will be connected to the grid and 7 % to off-grid options. The South African Department of Energy considers off-grid applications due to the transmission and distribution system cost to remote rural areas (Jamal, 2015). Small-scale CSP systems will have to compete against PV with battery storage or with back-up fuel sources and the fact that CSP seems to benefit more from the economics of scale ensures greater challenges for CSP. A possible solution is to establish micro-grids connecting rural areas in clusters. A micro-grid is just like the normal grid but only on a smaller scale that have enough generation, storage and intelligence to operate independently from the larger grid (Lovins, 2011). The power usage for critical loads can also then be managed easier.

Another challenge also arises when looking for local skills to maintain the energy plant of a micro grid in remote areas. SORC's can play a vital role as ORC's are less complex with fewer and cheaper components where a system can run without supervision. The downside of small-scale CSP systems in an off-grid or micro-grid application is that there is very little industrial experience to accurately estimate the costs associated with implementing such systems (IEA, 2014). The first possible application for SORC's are micro-grids.

In the industrial sector, various industries could also potentially use a small-scale SORC. ProTarget, a company in Germany, has identified industries in South Africa that could be typical users of a small-scale system (Mitchell & Scheuerer, 2014):

- Food and beverage industry
- Abattoirs
- Breweries and distilleries
- Textile and leather industry
- Paper industry
- Pharmaceutical and chemical industry
- Mining and oil industry

- Plastics and rubber industry
- Hotel and tourism industry
- Water treatment systems

The interest in small-scale SORC's has definitely grown over the past years but SORC's are still considered an immature technology, as they are still in the research and development phase. The successful operation of the few SORC has proven the technical feasibility of combining CSP with ORC's. The biggest challenge for SORC's remains to prove whether it is a relevant and economically competitive renewable energy source within certain contexts or not.

3 Site Selection

In this chapter, firstly a suitable industry is identified for a SORC within the South African context and solar resource distribution. Secondly, the chapter continues by selecting a specific location for the implementation of a SORC using a selection tool.

3.1 Industry selection

A suitable site for the implementation of a SORC will be where one of the possible industries listed in subsection 2.3.2 falls in the higher DNI region of SA. The most industrial development in South Africa is around the Gauteng area where the average annual sum DNI is about 2000 kWh/m^2 and around the coastal towns of Durban, East-London, Port Elizabeth and Cape Town where the DNI levels decrease dramatically referring to figure 12.

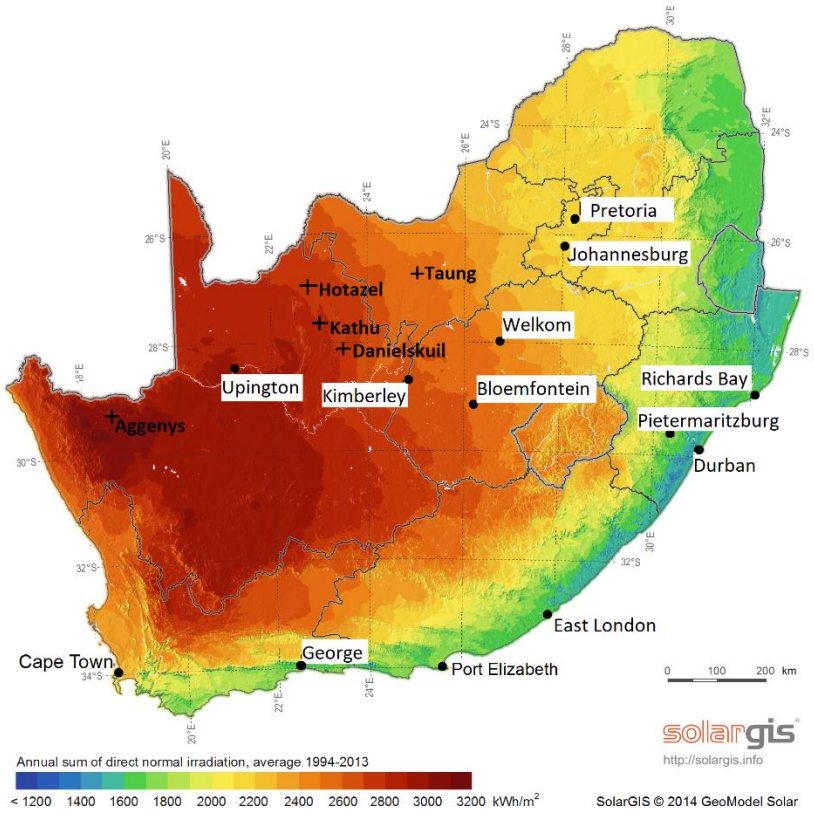

Figure 12: South African DNI map, (GeoSun Africa, 2016)

In the higher DNI region in the North Western part of South Africa, numerous mining industries exist in the region from Kimberley stretching Westward and past Upington. Most of these mines have been running for numerous years and are grid connected.

Currently the Thabazimbi mine of Croniment Mining AG, is the only mine in SA that runs completely off-grid. The mine has a 1 MW_e demand and is being powered by Solar PV and diesel generators. This mine however falls outside the higher DNI region of SA (Günter & Colin, 2016).

In the higher DNI region various smaller mines consuming a total of less than 5 MW_e are listed in table 4. Even though these mines are grid-connected, it is still a viable case study to analyse whether an SORC could be a feasible solution for a mine. In proving so, the proposition then exists to use a SORC for future mining developments in a similar area where the cost can be compared with the cost of installing a new grid section. This is another reason for considering the mining industry as the other industries are mostly found in industrial developed areas and the chances of there not being a grid connection, is slim.

Table 4: Smaller mines in the higher DNI region of SA, (World Bank Database, 2016)

Mine	Commodity	Location	Energy demand (MW_e)
Finsch	Diamond	Near Danielskuil	1.56
Avontuur Manganese Project	Manganese, iron ore	Near Hotazel	3.03
Pering	Lead	Near Taung	0.49
Black Mountain	Zinc, lead, silver and copper	Near Aggeneys	4.81
Tshipi	Manganese	Near Kathu	4.17
Wessels	Manganese	Near Hotazel	3.13
Gloria	Manganese	Near Hotazel	3.13

3.2 Specific site selection

The decision of which site will be used as case study is decided using a multi criteria decision analysis (MCDA) tool namely the simple multi-attribute rating technique (SMART) described in (Evans, 2017) and developed by (Von Winterfeldt & Edwards, 1986).

The value tree generated for the SMART analysis can be seen in figure 13. The analysis consists of two main categories namely cost and performance. Even though the final decision on which technology to implement will mainly be based on cost, it is difficult to make an accurate cost estimate at this stage. Access to economic data is restricted while the performance parameters are easy to quantify, as data is readily available. The five sites are all situated in the Western region of South Africa hence the assumption is made that no relative difference in the two cost parameters exist between the five sites.

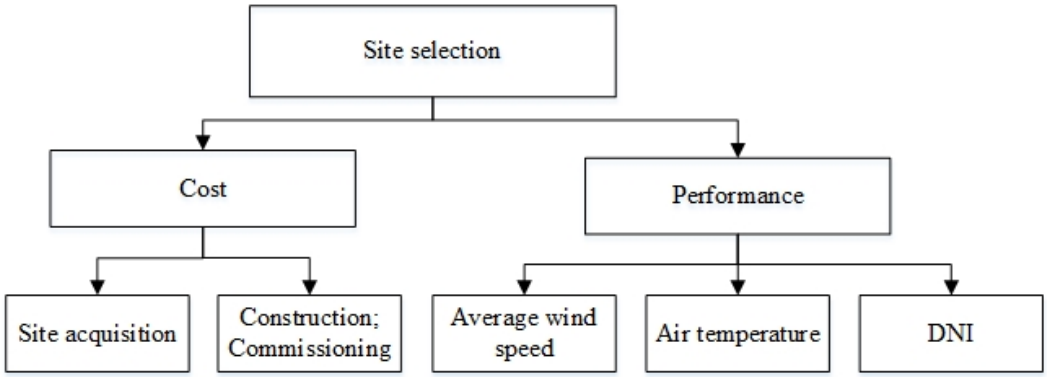

Figure 13: Site selection value tree

The performance evaluation consists of the average wind speed, the average air temperature and the average annual sum DNI. Higher wind speed has an adverse effect on PT performance as the heat loss from the receivers increase. A higher average air temperature firstly reduces the losses from the PT receiver having a positive effect on system performance. Secondly, in the case of using an ACC, the higher temperature increases the condensing temperature of the working fluid for a constant initial temperature difference (ITD), having an adverse effect on system performance. The latter case outweighs the importance of the first therefore a lower air temperature is desired. The effect of the wind speed, air temperature and DNI on the performance analysis are weighed 10 %, 10 % and 80 % respectively as an estimated indication the effect each has on performance. The data for each location is presented in table 5.

Table 5: Possible mining locations for SORC implementation, (SODA, 2014)

	Performance		
Location	**Average wind speed (km/h)**	**Average air temperature (°C)**	**DNI (kWh/m^2)**
Danielskuil	14.8	17.3	2517
Hotazel	14.4	19.7	2472
Taung	13.3	18.2	2409
Aggeneys	15.1	18.9	2754
Kathu	14.8	18.3	2526

This data is linearly scaled between the minimum and maximum value for each category noting that higher wind speed has a negative effect on the solar field performance therefore the wind speed is inversely scaled between minimum and maximum. The scaled values are then multiplied with the weighted importance of each category and an overall result is obtained to determine the preferred location. This process is displayed in table 6.

Table 6: SMART selection

	Cost		Performance			
Location	**Site acquisition**	**Construction and commissioning**	**Average wind speed (km/h)**	**Average air temperature**	**DNI (kWh/m^2)**	**Result**
Max Value	1	1	15.1	19.7	2754	
Min Value	1	1	13.3	17.3	2409	
Danielskuil	1	1	0.17	1	0.31	**0.53**
Hotazel	1	1	0.39	0	0.18	**0.39**
Taung	1	1	1	0.63	0	**0.37**
Aggeneys	1	1	0	0.33	1	**0.88**
Kathu	1	1	0.17	0.58	0.34	**0.51**

From the SMART analysis, the preferred location is Aggeneys. Kathu follows with Danielskuil, Hotazel, and Taung in descending order of preference. Seeing that the analysis result is by far in the favour of Aggeneys, small adjustments to the assumed weighted parameters will not make a difference in the outcome. Following this SORC's with the range 500 kW_e – 5 MW_e will be theoretically analysed in chapter 4 and then simulated for a typical small-scale mine situated in the Aggeneys area in chapters 5 and 6.

4 Theoretical Analysis

This chapter theoretically analyses the power plant and its functional units namely the solar field, storage and ORC power block. The type of hardware choices for each functional unit is also presented here. A quick investigation into the solar effects is given and thereafter a thermal analysis and pressure drop analysis is conducted on the solar field. Regarding the storage, a very basic analysis is presented. The power block is considered in detail by first selecting a suitable working fluid, considering the power block layout and analysing each component of the power block. After concluding this chapter all the theory is present to successfully simulate the SORC plant at design point.

4.1 SORC plant layout

When looking at a typical SORC plant, the plant can be divided into three main functioning units namely the solar field, TES and power block. This functional layout as depicted in figure 14 forms the basis of the plant wherein each of the functioning units can have various components and technology.

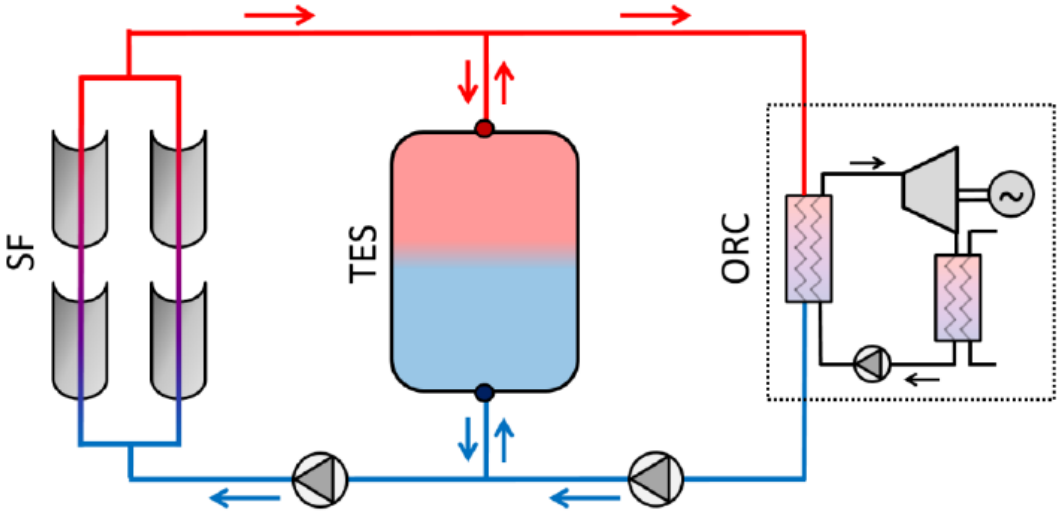

Figure 14: General plant layout (Dickes et al., 2015)

The power output of the plant is described as follows:

$$\dot{W}_{gross} = \eta_{PT}\,\eta_{PB}\dot{Q}_{in} \tag{4-1}$$

and

$$\dot{W}_{net} = \eta_{plant}\dot{Q}_{in} \tag{4-2}$$

In terms of the individual components in the plant, the net power output of the plant can also be calculated after knowing the individual power consumptions of the power block pump, condenser fan and solar field pump. The net power output of the plant is:

$$\dot{W}_{Net} = \dot{W}_{gross} - (\dot{W}_{PB,pump} + \dot{W}_{C,F} + \dot{W}_{SF,pump}) \quad (4\text{-}3)$$

4.2 Solar field

4.2.1 Hardware choice

The solar field is responsible for collecting the sun's energy and various types of technology were briefly discussed in subsection 2.1.2 to perform this function. For the scale of electricity production this project considers, linear concentrating collectors are the best option. The cost of energy considering LFR's and PT's for a given ORC plant with specific working fluid is nearly equal (Desai & Bandyopadhyay, 2016). LFR collectors have high optical losses and at high incidence angles the optical efficiency decreases rapidly, leaving PT's to have a much higher overall thermal performance. In terms of net electricity production over a one year period, a plant using PT's can have up to 6 % higher overall efficiency when compared to using LFR's for the same size plant (Giostri et al., 2012).

The PT technology is more mature than LFR hence PT's are more widely used than LFR's especially with Rankine cycles. PT's are well known and trusted by the industry and considered state of the art. Current research and development concentrate on substantial progress in selective surfaces, improved materials, manufacturing processes and vacuum technology to further better the thermal performance of a PT collector (Yilmaz & Söylemez, 2014). Because of these combined facts, a PT will be the technology of choice for the solar field.

In a PT field, the length of the hot outlet piping must be minimised in order to minimise thermal losses. The central feed layout configuration minimises piping all together as there is no pipe running the length of the collector row. Direct access to each collector row is available without the need of underground piping which is necessary especially in cleaning the mirrors. This is a major advantage for the central feed layout when compared to the direct return and reverse return configurations. The central feed layout configuration is most widely used and is the preferred option over the direct return and reverse return configurations for solar fields of the current scale (Lovegrove & Stein, 2012). The central feed configuration that will be considered for this project is showcased in figure 15.

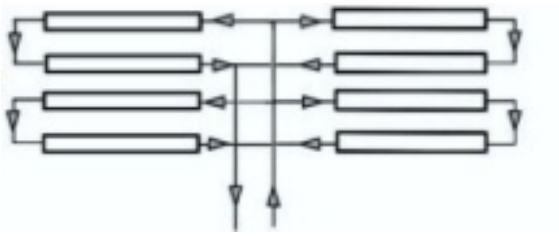

Figure 15: Central feed layout, adapted from (Lovegrove & Stein, 2012)

The selection of heat transfer fluid (HTF) is very important in the design phase. A single-phase liquid has the best heat transfer coefficients and provides stable thermal operation. Thermal oil is the standard HTF used in a PT as nearly all PT power plants use synthetic thermal oils (Günther et al., 2011). Sometimes for temperatures below 200 °C, pressurized water or a mixture of water and ethylene glycol is used (Lovegrove & Stein, 2012). Eastman developed Therminol 66, a synthetic thermal oil for non-pressurized/low-pressure systems to be used amongst others in ORC applications. Therminol 66 can be effectively used in the temperature range of -3 °C to 345 °C, and is non-corrosive to metals (Eastman, 2017). Therminol 66 is the HTF of choice for this project. The complete set of Therminol 66 fluid properties can be found in appendix A.

4.2.2 Solar radiation and tracking

In order to maximise the collector's aperture exposure to the incoming solar irradiance various solar tracking mechanisms have been developed. The basic principle is for the collector's aperture to follow the sun as the sun moves across the sky during the day. The tracking axis can be orientated and tilted in different ways with the most common orientations being a horizontal tracking axis, tilted tracking axis, offset aperture, vertical tracking axis, vertical tracing axis with an offset, and lastly a tracking axis that is tilted at latitude angle.

In figure 16 the typical effect the type of tracking has on the amount of solar irradiation falling on the collector aperture can be seen. One axis horizontal tracking will be considered for this analysis because of the large solar field that will be required for the needed power output. To get an idea of the size range of the solar field this project is investigating, a PT solar field for a 1 MW_e SORC power plant is roughly 10 ha (Vélez et al., 2012) .

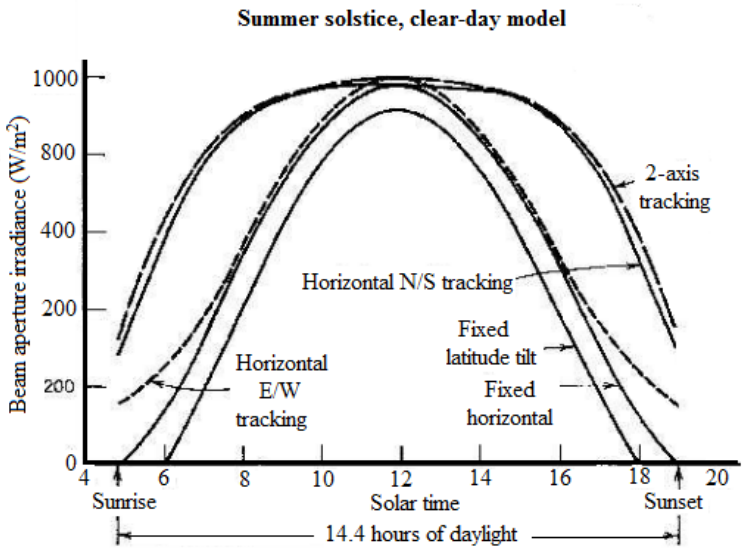

Figure 16: Solar irradiance that reaches the different tracking types' collectors, (Stine & Geyer, 2001)

When designing the power plant, it is important to be able to predict the angle between the vector normal to the collector aperture and the sun's rays. This angle is referred to as the *angle of incidence* (θ_i) and the maximum amount of solar radiation energy which could reach the PT collector is reduced by the cosine of this angle (Stine & Geyer, 2001). The angle of incidence differs for the different ways of tracking and this analysis will consider one axis horizontal tracking. Furthermore the collector tracking axis will be configured to align in the North-South direction to provide the collector to gather more energy from the sun with respect to the other orientations over a period of one year (Yilmaz & Söylemez, 2014). The angle of incidence can therefore be expressed as a function of location (latitude, $\emptyset$, which is negative for the southern hemisphere), time (hour angle, ω) and date (declination angle, δ), (Stine & Geyer, 2001):

$$cos\theta_i = \sqrt{cos^2\theta_z + cos^2\delta \times sin^2\omega} \tag{4-4}$$

Where the zenith angle:

$$\theta_z = cos^{-1}(sin\delta sin\emptyset + cos\delta cos\omega cos\emptyset) \tag{4-5}$$

The declination angle is defined as follow:

$$\delta = sin^{-1}(0.39795\cos(0.98563(N - 173))) \tag{4-6}$$

The hour angle is defined as follow:

$$\omega = 15(ts - 12) \tag{4-7}$$

where the solar time:

$$ts = LCT + \frac{EOT}{60} - LC - D \tag{4-8}$$

with

$D = 1$ (if daylight savings time is in effect)

$D = 0$ (if daylight savings time is not in effect)

$$LC = \frac{longitude - \left(\begin{matrix}longitude\ of\ standard \\ time\ zone\ median\end{matrix}\right)}{15} \tag{4-9}$$

$$EOT = 0.258cosx - 7.416sinx - 3.648cos2x - 9.228sin2x \tag{4-10}$$

and

$$x = \frac{360(N-1)}{365.242} \tag{4-11}$$

4.2.3 Thermal analysis of receiver

A thermal analysis of the collector's receiver is required to determine the useful heat that is gained in absorber tube. The heat is transferred from the solar irradiance falling on the collector aperture as depicted in figure 17. The analysis can then predict the behaviour of the PT solar field for certain working conditions. The solar field consists of various PT modules using evacuated tubes as receiver type.

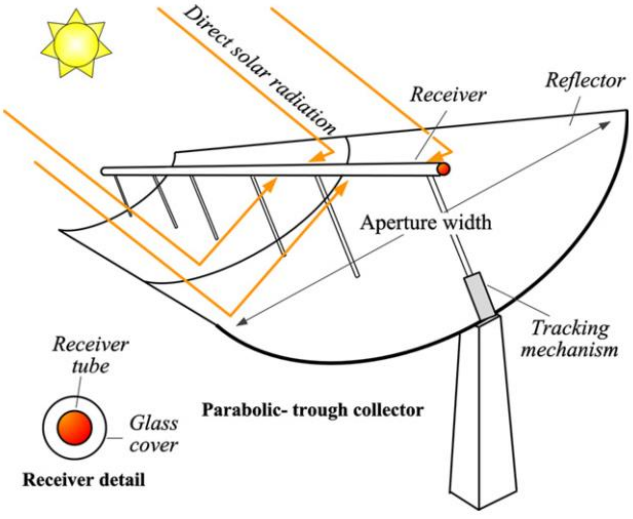

Figure 17: Parabolic trough collector (Cabrera et al., 2013)

Various thermal models have been developed to accurately model a PT collector with an evacuated tube receiver (Russell, 2003), (Padilla et al., 2011), (García-Valladares & Velázquez, 2009), (Yilmaz & Söylemez, 2014). When comparing these analytical and numerical models to test results of Sandia National Laboratory, certain models were more accurate than others. A detailed RMSE (Root Mean Square Error) analysis was done by (Yilmaz & Söylemez, 2014) to compare these models. Table 7 summarises the accuracy of the different models compared to the Sandia National Laboratory test results.

Table 7: RMSE PT collector model comparison

Model	**RMSE**
	η_{pt} (%)
Vacuum intact	
Yilmaz & Söylemez model	0.766
Padilla et al. model	1.012
García-Valladares & Velázquez model	1.433
NREL model	1.382
Air annulus	
Yilmaz & Söylemez model	1.429
Padilla et al. model	1.225
García-Valladares & Velázquez model	2.292
NREL model	1.562

Under vacuum conditions, the Yilmaz & Söylemez model gave the most accurate results over the entire temperature range. The model predicted the solar field exit temperature very accurately and showed the best overall accordance with test results of all the PT models. The methodology behind the Yilmaz & Söylemez model originates from Kalogirou (2012) but Yilmaz & Söylemez developed their own heat transfer model for the differential area. The basic methodology considers a single differential area of a PT collector receiver. This is done by discretizing the receiver through dividing it into N equal finite segments that is modelled. At each differential step, the analysis estimates the solar heat gained and the thermal losses from the receiver separately.

After the useful heat gained at that incremental step, the increase in mean fluid temperature is calculated. This is then extrapolated to the entire solar field to calculate the total heat gained. The thermal analysis present in this chapter will therefore also take this approach in the methodological sense as described above. The analysis will be conducted from first principles and the thermal models will be self-developed. The analysis will be done with the following assumptions:

- The conduction heat loss through to the retainer keeping the receiver in place is considered negligible.

- The pipes transporting the heat transfer fluid between PT modules, the header pipes at the ends of the solar field and the pipes to and from the storage tanks are assumed to be perfectly insulated and their heat losses to the environment are negligible.

- The thermal conditions at the heat transfer surface is approximated as constant surface heat flux (Yilmaz & Söylemez, 2014), (Kalogirou, 2012).

- The HTF temperature in the solar field remains lower than the boiling temperature of Therminol 66 hence no phase change in the heat transfer fluid happens during the flow through the solar field.

- The flow is hydrodynamically fully developed as the hydrodynamic entry length is well short of the trough length and momentum entrance effects can be neglected.

- The flow in the PT receiver is expected to be turbulent therefore the flow is considered thermally fully developed as the thermal entry length is well short of trough length.

- For each differential area, the only significant temperature gradient exists in the radial direction of the receiver. The heat gained by the receiver per differential area is treated as a one-dimensional heat transfer problem in the radial direction. The temperature gradient in the axial direction is in turn interpreted as a one dimensional forced convection problem.

The most important parameters to be calculated with the thermal analysis is the solar field outlet temperature, useful heat gain and PT collector efficiency. The PT collector is discretised down its length and for each differential control volume all the calculations are done. The discretised receiver tube is shown in figure 18.

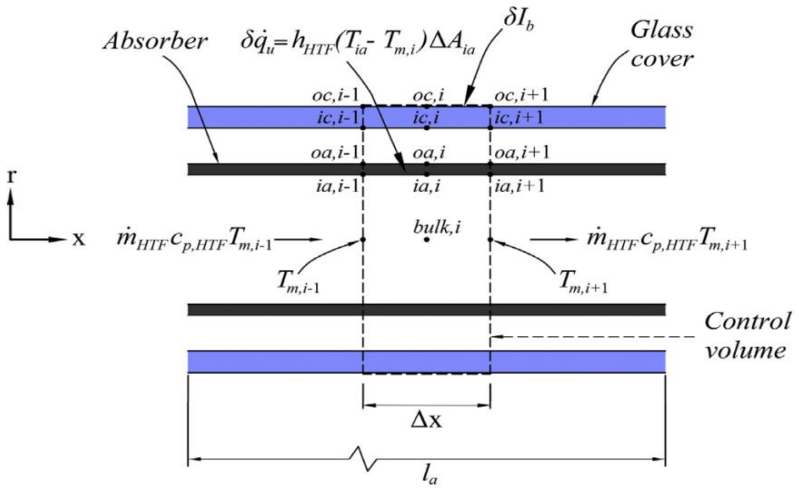

Figure 18: Differential control volume of the receiver, (Yilmaz & Söylemez, 2014)

The incoming radiation is concentrated by the collector onto the receiver tube where a portion of the heat is absorbed by the HTF and another portion lost into the atmosphere as thermal losses. After an energy balance is conducted over the control volume of figure 18, a generalised form of a governing equation can be expressed as:

$$\sum_{i=1}^{N} \delta\dot{q}_{gain} p_{ia} \Delta x = \dot{m}_{HTF} \left[\left(h + \frac{u_m^2}{2} \right)_{i+1} - \left(h + \frac{u_m^2}{2} \right)_{i-1} \right] \tag{4-12}$$

$$i = 1,2,3, \dots, N$$

Where $\delta\dot{q}_{gain}$ is the useful heat gained over the inner surface of the absorber differential ($A_{ia} = p_{ia}\Delta x$). For incompressible fluids $h \cong c_p T$ and it can be assumed the kinetic terms will have a negligible difference over the differential area for steady state conditions. Therefore, the increase in temperature of the heat transfer fluid over the differential area can be expressed as:

$$T_{m,i+1} = T_{m,i-1} + \frac{\delta\dot{q}_{gain} p_{ia} \Delta x}{\dot{m}_{HTF} C_{p,HTF}} \tag{4-13}$$

To determine the useful heat gained, the thermal resistance method is used. In figure 19, the cross-sectional area of the differential control volume is shown with the one-dimensional radial heat transfer. With energy balances, the nodal temperatures and the heat transfer rates are found. A small percentage of the incoming solar irradiation is absorbed by the glass cover and the rest of the heat is deposited on the outer surface of the absorber tube. As the outside surface temperature of the absorber tube increases, the heat is conducted through the absorber wall to the heat transfer fluid by forced convection (useful heat).

The rest of the heat is lost to the vacuum annulus as radiation. The lost heat is then conducted through the glass cover wall because glass is opaque to long wavelength radiation. The combination of the conducted heat and absorbed solar heat is then lost to the surroundings by a combination of convection and radiation. The assumption is made that all heat fluxes and temperatures are uniform around the circumference of the receiver. In reality this is not the case as the bottom part of the receiver receives much higher flux. For the methodology of this model it has been proven that making this simplifying assumption does not introduce any significant error (Kalogirou, 2012) and this approach is more conservative.

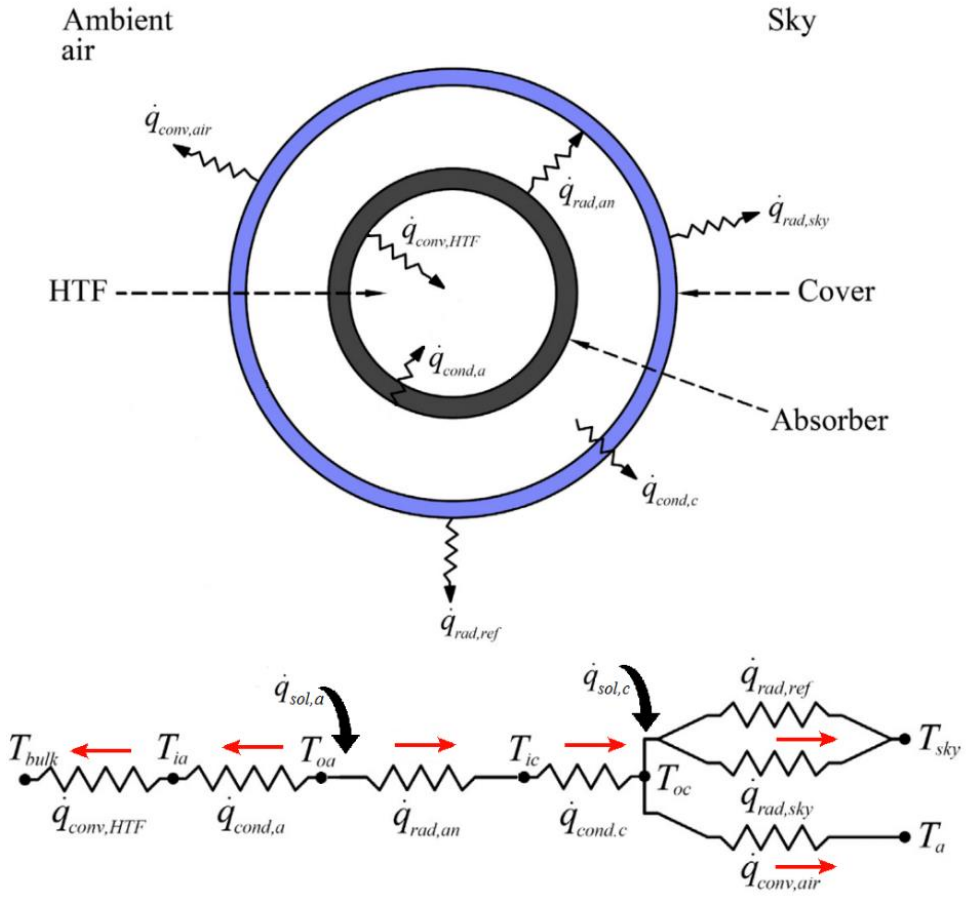

Figure 19: Cross-section of the receiver tube with the accompanying the thermal resistance diagram, adapted from (Yilmaz & Söylemez, 2014)

Energy equations are written between the nodal temperature points of the resistance diagram and the rate of heat transfer relationships are expressed in equations 4-14 – 4-17 while these rates are further investigated in the following paragraphs.

$$\dot{q}_{conv,HTF} = \dot{q}_{cond,a} \tag{4-14}$$

$$\dot{q}_{rad,an} = \dot{q}_{sol,a} - \dot{q}_{cond,a} \tag{4-15}$$

$$\dot{q}_{cond,c} = \dot{q}_{rad,an} \tag{4-16}$$

$$\dot{q}_{cond,c} + \dot{q}_{sol,c} = \dot{q}_{rad,ref} + \dot{q}_{rad,sky} + \dot{q}_{conv,air} \tag{4-17}$$

Solar heat gained:

The solar absorption in the glass envelope is a heat generation phenomenon. The glass cover wall is relatively thin and the solar absorptance coefficient is very small, therefore solar absorption can be treated as a heat flux phenomenon without introducing significant errors (Kalogirou, 2012). The solar absorption in the glass cover can be calculated as such:

$$\dot{Q}_{sol,c} = I_{b,n}\eta_{opt}\alpha_c l_{ap} dx \tag{4-18}$$

where the effective optical efficiency at the glass cover, η_{opt} is:

$$\eta_{opt} = e_{sh}e_{ge}e_{tr}e_{dm}e_{da}e_{un}\rho_{cl}K_\theta \tag{4-19}$$

and the incidence angle modifier K_θ is:

$$K_\theta = \cos\theta_i + 0.000884\theta_i - 0.00005369\theta_i^2 \tag{4-20}$$

The parameters used to estimate the optical efficiency were generated by the National Renewable Energy Laboratory (NREL) in Colorado, USA report (Price et al., 2002), based on field tests done by Dudley et al. (Dudley et al., 1994 in Kalogirou, 2012). The tests also concludes that a valid assumption can be made that the parameters are independent of temperature. These parameters are only valid for normal solar irradiance and the incident angle modifier is used to account for incident angle losses.

The solar energy that is not absorbed in the glass cover is deposited on the receiver tube's outside surface and this is treated as a heat flux phenomenon. The solar heat flux can be calculated as such:

$$\dot{Q}_{sol,a} = I_{b,n}\eta_a\alpha_a l_{ap} dx \tag{4-21}$$

where the effective optical efficiency at the receiver tube, η_a is:

$$\eta_a = \eta_{opt}\tau_c \tag{4-22}$$

Heat conduction through the absorber wall:

The heat transfer through the absorber tube wall happens through conduction heat transfer. This is expressed with Fourier's law of heat conduction for a cylinder:

$$\dot{Q}_{cond,a} = \frac{T_{oa} - T_{ia}}{R_{cond,a}} \tag{4-23}$$

where

$$R_{cond,a} = \frac{ln(D_{oa}/D_{ia})}{2\pi k_a \Delta x} \tag{4-24}$$

Heat transfer to the heat transfer fluid:

The heat is now transferred to the HTF by means of internal forced convection. The flow regime of the fluid is defined by the Reynolds number which specifies whether the flow is laminar or turbulent. For a laminar flow regime the Reynolds number need be below the critical defined Reynolds number of 2300 (Çengel & Ghajar, 2015). Under steady state conditions the mass flow rate of the heat transfer fluid can be written as:

$$\dot{m}_{HTF} = \rho_{HTF} A_a u_{m,HTF} \tag{4-25}$$

The flow is considered to be fully developed as it is both hydrodynamically and thermally developed. For a laminar flow regime inside a circular tube under the assumed conditions of constant heat flux upon the receiver, the Nusselt number is a constant which is (Çengel & Ghajar, 2015), (Yilmaz & Söylemez, 2014):

$$Nu_{HTF} = 4.364 \tag{4-26}$$

The transitional region between laminar and turbulent flow can lead to unstable solutions. For PT collectors the Reynolds number is typically high enough to ensure turbulent flow therefore the assumption is made that flow will be turbulent and this assumption is monitored in the simulation. In the case of a fully turbulent flow regime (Re above 10 000) the heat transfer can be expressed for smooth pipes as was developed by experimental studies (Sandall et al., 1980):

$$Nu_{HTF} = \frac{\sqrt{f/8}\, Re_{HTF} Pr_{HTF}}{12.48 Pr_{HTF}^{2/3} - 7.853 Pr_{HTF}^{\frac{1}{3}} + 3.613 \ln(Pr_{HTF}) + 5.8 + C} \tag{4-27}$$

$$For \quad 0.5 \leq Pr \leq 2000$$

$$10^4 \leq Re \leq 5 \times 10^6$$

Where $C = 2.78 \ln\left(\frac{\sqrt{f/8} Re_{HTF}}{90}\right)$ and f is the Fanning friction factor, which is defined for smooth pipes as $f = (0.79 ln Re_{HTF} - 1.64)^{-2}$.

The convective heat transfer coefficient on the inside of the absorber tube can then be calculated from:

$$h_{HTF} = Nu_{HTF} \frac{k_{HTF}}{D_{ia}} \tag{4-28}$$

The thermal convective resistance is then:

$$R_{conv,HTF} = \frac{1}{\pi D_{ia} h_{HTF} \Delta x} \tag{4-29}$$

Following from Newton's law of cooling the convective heat transfer within the absorber tube can be expressed as:

$$\dot{Q}_{conv,HTF} = \frac{T_{ia} - T_{bulk}}{R_{conv,HTF}} \tag{4-30}$$

Where $T_{bulk} = T_{m,i}$ and is the bulk mean fluid temperature. It can be approximated with the arithmetic mean temperature difference:

$$T_{bulk} = \left(\frac{T_{m,i-1} + T_{m,i+1}}{2}\right) \tag{4-31}$$

Seeing that $T_{ia} >> T_{bulk}$, all HTF properties will be evaluated at the mean film temperature:

$$T_{film} = \left(\frac{T_{bulk} + T_{ia}}{2}\right) \tag{4-32}$$

Annulus region heat transfer:

The heat transfer in the annulus region happens by means of thermal radiation only because of the vacuum that exists in the annulus region. The absorber outside surface behaves nearly grey (surface properties are independent of wavelength) diffuse emitter (surface properties are independent of direction) in the solar spectrum when the surface's emissivity remains close to constant for incidence angles of lower than 40˚ (Touloukian & Dewitt, 1972) in (Yilmaz & Söylemez, 2014). When considering an enclosure consisting of two opaque surfaces at certain temperatures, the heat transfer is expressed by (Çengel & Ghajar, 2015):

$$\dot{Q}_{rad,a} = \frac{T_{oa} - T_{ic}}{R_{rad,a}} \tag{4-33}$$

where

$$R_{rad,a} = \frac{1}{\pi D_{oa} h_{rad,a} \Delta x} \tag{4-34}$$

with $h_{rad,a}$ simplified for infinitely long concentric circles as:

$$h_{rad,a} = \frac{\sigma(T_{oa} + T_{ic})({T_{oa}}^2 + {T_{ic}}^2)}{\frac{1}{\varepsilon_a} + \frac{1 - \varepsilon_c}{\varepsilon_c}\left(\frac{D_{oa}}{D_{ic}}\right)} \tag{4-35}$$

Heat conduction through the glass cover wall:

The solar absorption in the glass cover has already been dealt with and the heat conduction though the cover wall can thus be expressed by Fourier's law:

$$\dot{Q}_{cond,c} = \frac{T_{ic} - T_{oc}}{R_{cond,c}} \tag{4-36}$$

where

$$R_{cond,c} = \frac{ln(D_{oc}/D_{ic})}{2\pi k_c \Delta x} \tag{4-37}$$

Heat transfer from the cover to the surroundings:

The heat loss from the cover occurs from the outer surface with both thermal radiation to the sky and convection heat loss to the ambient air. In order to model the reality better, the convection heat loss will be considered as a combination between natural and forced convection. As the wind loads may vary from zero to very strong winds also changing direction, this combined convection approach is essential. The error of ignoring natural convection at high velocities is negligible but may be significant at low velocities.

A parameter called the Richardson number, Ri, has thus been developed to assess the relative importance of the natural convection component. As the heat transfer coefficient of forced convection is a strong function of the Reynolds number Re, and for natural convection the heat transfer coefficient is a strong function of the Grashof number, Gr. The parameter was defined as $Ri = Gr/Re^2$ and is stated that when $Ri < 0.1$, natural convection is negligible, when $Ri > 10$ then forced convection is negligible, and both are considered when $0.1 < Ri < 10$ (Çengel & Ghajar, 2015), (Naeeni & Yaghoubi, 2007).

Because of the varying wind loads, both convection regimes will be considered. After a study that observed various temperature and velocity fields around the collector, it was found that the effect of the collector's orientation on heat transfer could be neglected for wind speeds that result in a $Re \leq 4.5 \times 10^5$ based on the collector aperture. This correlates with wind speeds < 13 m/s at standard atmospheric conditions. The receiver tube can be considered isothermal over the discretised control volume length and for an isothermal horizontal tube in an isothermal environment the heat transfer coefficient can then be calculated as follow (Yilmaz & Söylemez, 2014), (The subscripts and superscripts used in equations 4-38 – 4-43 are only to distinguish between the Nusselt umbers):

$$Nu^T = 0.772 Ra_{air}^{1/4} \tag{4-38}$$

$$Nu_l = \frac{2f}{ln(1 + 2f/Nu^T)} \quad \rightarrow f = 1 - \frac{0.13}{(Nu^T)^{0.16}} \tag{4-39}$$

$$Nu_t = 0.103 Ra_{air}^{1/3} \tag{4-40}$$

$$Nu_N = [(Nu_l)^{10} + (Nu_t)^{10}]^{1/10} \tag{4-41}$$

$$Nu_F = aRe^n \tag{4-42}$$

To calculate the mixed convective regime heat transfer, a procedure was proposed by (Morgan, 1975). Taking $Nu_F = Nu_N$ and the constants a and n from table 8 the procedure can be expressed as follow:

Table 8: Constants for equations to calculate the mixed convective regime heat transfer

	Re range						
	10^{-4} to 4×10^{-3}	4×10^{-3} to 9×10^{-2}	9×10^{-2} to 1.0	1.0 to 35	35 to 5×10^{3}	5×10^{3} to 5×10^{4}	5×10^{4} to 2×10^{5}
a	0.437	0.565	0.8	0.795	0.583	0.148	0.0208
n	0.0895	0.136	0.28	0.384	0.471	0.633	0.814

$$Re_i = [Nu_N/a]^{1/n} \tag{4-43}$$

Calculation an effective Reynolds number from:

$$Re_{eff} = [(Re_i + Re_{air} cos\emptyset)^2 + (Re_{air} sin\emptyset)^2]^{1/2} \tag{4-44}$$

Then substituting back into equation 4-43 the Nu is obtained for the mixed convection flow regime:

$$Nu_{air} = aRe_{eff}^n \tag{4-45}$$

The heat transfer coefficient for the mixed convective regime for the outside of the receiver tube is then expressed as:

$$h_{air} = Nu_{air} \frac{k_{air}}{D_{oc}} \tag{4-46}$$

The thermal convective resistance is then:

$$R_{conv,air} = \frac{1}{\pi D_{oc} h_{air} \Delta x} \tag{4-47}$$

Following from Newton's law of cooling the convection heat transfer for the outside of the receiver tube is:

$$\dot{Q}_{conv,air} = \frac{T_{oc} - T_a}{R_{conv,air}} \tag{4-48}$$

For the calculation of the radiation heat transfer, it is taken that the bottom half of the cover emits radiation to the reflector mirror and the top half of the cover to the sky. The reflector mirror is assumed to be at local air temperature. Furthermore, the cover is treated as a small convex grey object in a larger blackbody cavity, which is the sky. In reality the sky is not a blackbody however Kalogirou (2012) stated that it is common practice to model it this way. Various correlations exist where the effective sky temperature is related to the ambient temperature (Yilmaz & Söylemez, 2014), (Kalogirou, 2012) but as the sky temperature is more a function of upper atmospheric conditions and remains more or less constant, a temperature of 0 °C will be assumed for the sky temperature. The sensibility of the simulation towards this value is monitored. The resultant heat transfer rates for the cover can be calculated as follow:

$$\dot{Q}_{rad,sky} = \frac{T_{oc} - T_s}{R_{rad,sky}} \tag{4-49}$$

$$\dot{Q}_{rad,ref} = \frac{T_{oc} - T_a}{R_{rad,a}} \tag{4-50}$$

where

$$R_{rad,sky} = \frac{1}{\pi (D_{oc}/2) h_{rad,sky} \Delta x} \tag{4-51}$$

$$R_{rad,ref} = \frac{1}{\pi (D_{oc}/2) h_{rad,ref} \Delta x} \tag{4-52}$$

with $h_{rad,sky}$ and $h_{rad,ref}$ calculated as follow:

$$h_{rad,sky} = \sigma\varepsilon_c(T_{oc} + T_{sky})({T_{oc}}^2 + {T_{sky}}^2) \tag{4-53}$$

$$h_{rad,ref} = \sigma\varepsilon_c(T_{oc} + T_a)({T_{oc}}^2 + {T_a}^2) \tag{4-54}$$

PT collector efficiency:

The thermal efficiency of the PT field is the ratio of the total solar radiation falling onto the PT receiver to the heat that is absorbed into the HTF. The thermal losses that occur is due to the temperature difference between the receiver tube and ambient conditions. The thermal efficiency is expressed as:

$$\eta_{th} = \frac{\dot{Q}_{gain}}{\dot{Q}_{in}\eta_{opt}} \tag{4-55}$$

where η_{opt} is the effective optical efficiency from equation 4-19 and

$$\dot{Q}_{in} = I_{b,n}A_a \tag{4-56}$$

the overall efficiency of the solar field can then be expressed as:

$$\eta_{SF} = \eta_{opt}\eta_{th} = \frac{\dot{Q}_{gain}}{\dot{Q}_{in}} \tag{4-57}$$

4.2.4 Pressure drop analysis

The reason for analysing the pressure drop in the solar field's receiver tubes is to determine the power requirements to maintain the HTF flow. Once the pressure loss is known in the pipes, the power requirement of the pump to overcome the pressure loss can be calculated:

$$\dot{W}_{SF,pump,L} = \frac{\dot{V}\Delta P_L}{\eta_{SF,pump}} \tag{4-58}$$

with

$$\Delta P_L = \Delta P_{major} + \Delta P_{minor} \tag{4-59}$$

Major pipe losses:

The pressure drop is due to viscous effects and represents an irreversible pressure loss effect. This pressure loss can be expressed for all types of fully developed internal flows as (Çengel & Ghajar, 2015):

$$\Delta P_{major} = f \frac{L}{D} \frac{\rho V_{avg}^2}{2} \tag{4-60}$$

where $\rho V_{avg}^2/2$ is the dynamic pressure and f is the Darcy friction factor.

Depending on the flow regime, whether the flow is laminar or turbulent, the friction factor is different. The flow regime is defined by the Reynolds number and for a fully developed laminar flow in circular tubes the Darcy friction factor is defined as (Çengel & Ghajar, 2015):

$$f = \frac{64\mu}{\rho D V_{avg}} = \frac{64}{Re} \tag{4-61}$$

It is notable that for the laminar case the Darcy friction factor is function of the Reynolds number only and independent of the pipe surface roughness. The case for turbulent flow differs as any irregularity or surface roughness disturbs the sublayer of flow and thus effects the flow. The friction factor for turbulent flow is a strong function of surface roughness and therefore for fully developed turbulent pipe flow the flow is dependent on the Reynolds number and the relative surface roughness, ε/D. An implicit relationship was developed to determine the friction factor known as the Colebrook equation:

$$\frac{1}{\sqrt{f}} = -2.0 log\left(\frac{\varepsilon/D}{3.7} + \frac{2.51}{Re\sqrt{f}}\right) \tag{4-62}$$

Because this relationship is implicit in f, it requires iteration to solve. An approximate explicit relationship for f was developed in 1983 by S.E. Haaland. The Haaland approximation can serve as a good initial guess for the iterative method of the Colebrook equation (Çengel & Ghajar, 2015):

$$\frac{1}{\sqrt{f}} \cong -1.8 log\left[\frac{6.9}{Re} + \left(\frac{\varepsilon/D}{3.7}\right)^{1.11}\right] \tag{4-63}$$

Minor pipe losses:

The minor losses are due to the fluid that pass through various fittings like elbows, T-sections, inlets, outlets, etc. The pressure drop due to these components is expressed in terms of their loss coefficient, K_L**:**

$$\Delta P_{comp} = \rho g h_L = \rho K_L \frac{V_{avg}^2}{2} \tag{4-64}$$

Another addition to the minor losses is the pressure drop in the evaporator, $\Delta P_{SF,e}$. A typical value for the evaporator pressure drop is assumed as expressed in subsection 4.4.4. The total pressure loss due to these minor effects can then be expressed as;

$$\Delta P_{minor} = \rho \frac{V_{avg}^2}{2} \left(\sum K_L \right) + \Delta P_{SF,e} \tag{4-65}$$

For the solar field layout as depicted in figure 15 the fittings and their respective representative loss coefficients for a single PT collector loop (four PT modules) can be seen in table 9 found in (Çengel & Cimbala, 2010).

Table 9: Solar field fittings for a PT collector loop

Fitting	Number of fittings	Loss coefficient
Elbows (Smooth bend)	2	0.3
180° return bend	2	0.2
T-section, run through	2	1
Flow rate control valves	2	2

With PT collector loops being typically a few hundred metres and comparing equation 4-65 with 4-60 it is clear that the minor pipe losses will be orders of magnitude smaller than the major losses making it negligible for the current purpose.

4.3 Storage

Solar energy as a resource is time dependant and energy demand is often time dependent as well but in a different fashion. Hence, the storage of energy is necessary to match the energy demand with the available energy supply (Duffie & Beckman, 2013). One of the main advantages of CSP over other renewable technologies is the possibility of integrating cost-effective local storage capacity that can be integrated into a design that delivers minimal or zero impact on system efficiency and cost of energy (Lovegrove & Stein, 2012).

Most solar power plants like the Spanish Andasol plant adopted an indirect TES system where thermal oil is used in the solar field as HTF and molten salt as storage medium in the storage tanks. These systems represent the state of the art storage technology with multiple subsystems and controlling strategies but due to complexity and cost, it is arguably unfeasible for small-scale systems.

To minimize cost one of the main considerations is to minimize storage volume. The ultimate reduction in storage volume can be achieved by a thermocline sensible-heat storage system using one tank for both the hot and cold fluid resulting in the storage volume equalling the storage fluid volume. The hot HTF, which is also the storage fluid, is then introduced to the top of the tank, while the cold fluid is withdrawn from the bottom of the tank. No heat exchangers are necessary as in the case of indirect storage that simplifies the system, reduces the cost and no heat exchanger inefficiencies play a role. Momentum-induced mixing of the hot and cold HTF is normally minimised by carefully designing the inlet and outlet diffusers (Stine & Geyer, 2001). The working principle of this system is illustrated in figure 20.

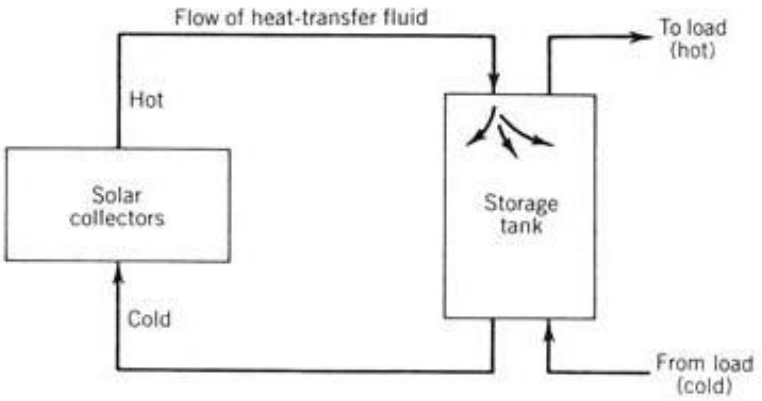

Figure 20: Thermocline sensible heat storage schematic, adapted from (Stine & Geyer, 2001)

For a uniform flow process, the energy balance of the TES tank can be written as:

$$\dot{Q}_{TES} = \dot{Q}_{Dump} - \dot{Q}_{Dis} - \dot{Q}_{L} \tag{4-66}$$

with

$$\dot{Q}_{Dump} = \dot{Q}_{SF} \tag{4-67}$$

$$\dot{Q}_{Dis} = \dot{Q}_{Evap} \tag{4-68}$$

The total net energy stored or discharged in kWh is then:

$$Q_{TES} = \dot{Q}_{TES}.hour \tag{4-69}$$

The thermal storage capacity of the tank, $Q_{TES,max}$, is dependent on the electrical energy demand of the plant in terms of length of operating hours required.

The volume of the TES tank can be determined from the definition of the HTF's heat capacity where

$$C_{p,HTF} = \frac{Q_{TES,max}}{m_{TES}T} \tag{4-70}$$

Hence the TES volume is:

$$V_{TES} = \frac{m_{TES}}{\rho_{HTF}} = \frac{Q_{TES,max}}{\rho_{HTF}C_{p,HTF}\Delta T} \tag{4-71}$$

4.4 Power block

4.4.1 Working fluid selection

The theory for an ORC is the same as the steam Rankine cycle with only the working fluid properties differing. The selection of the working fluid not only affects the efficiency of the system but also the design and size of the system components, stability, safety and environmental concerns and ultimately the cost of the system (Bao & Zhao, 2013). Hence, it is a very important degree of freedom for any ORC design process. Bao and Zhao (2013) continue by saying that the selection of an ORC working fluid is more complex than other thermodynamic cycles mainly due to two reasons:

- The temperature of the heat sources for ORC varies widely from 80 °C to 500 °C.
- Excluding a few organic fluids whose critical temperatures are too high or too low, hundreds of fluids are available for usage including hydrocarbons, aromatic hydrocarbons, perfluorocarbons, alcohols, CFS's, siloxanes, ethers etc.

Due to the working fluid selection being so important, many researchers have carried on the fluid screening method and this method is by far the most frequently used method for working fluid selection in scientific literature (Bao & Zhao, 2013). The method consists of building a steady state simulation model of the proposed ORC plant and run it with different working fluids to determine the most effective fluid for the current application.

Another fluid selection guideline has been developed by (Macchi & Astolfi, 2017) to help ORC designers with the task of screening hundreds of working fluids. The number of applicable fluids is drastically decreased by considering and comparing different fluids over a range of criteria. The first requirements that are considered is:

- *Commercially available at a reasonable cost*: with the intended storage and MW range of the proposed system, a large fluid inventory is needed and the fluid cost can mount up to a significant portion of the total plant cost.

- *Non-flammable*.

- *Nontoxic.*

- *Compatible with materials*: the working fluid must be compatible with the lubricating oils, elastomers, metals etc.

- *Environmentally benign*: the two main indexes that account for fluid acceptance is the Ozone Depletion Potential and the Global Warming Potential.

It is practically impossible to fulfil all these requirements with a working fluid that is suitable for all ORC applications hence ORC manufacturers must compromise on some of the qualities listed above but it is still aimed for (Macchi & Astolfi, 2017). The second list of considerations in selecting a suitable working fluid concerning the thermodynamic considerations were discussed in subsection 2.2.1.

In the case of varying heat source temperatures, it can be more advantageous to use mixtures of working fluids rather than pure working fluids. In such a system heat is supplied to or rejected at variable temperatures but at a constant pressure because the boiling temperature varies during phase change and the mixture evaporates over a large range of temperatures. The properties of these mixtures are however not always known (Bao & Zhao, 2013). At constant heat source temperatures, pure working fluids are more desirable and their fluid properties are readily available. The solar field with the incorporated storage allows for heat addition to the power block at constant temperature. Only pure working fluids will be considered henceforward.

In subsection 2.2.1 the working fluids were categorised according to their saturation curve and the categorisation disregards the structural point of view. When looking at the latter two, the possible ORC working fluids can be categorised in seven main classes and Bao and Zhao (2013) pointed out typical characteristics of each after screening the fluids over a range of applications:

1. Hydrocarbons; including linear (n-butane, n-pentane), branched (isobutane, isopentane) and aromatic hydrocarbons (toluene, benzene)
    - Flammability issues
    - Desirable thermodynamic properties

2. Perfluorocarbons;
    - Thermodynamically undesirable.
    - Extremely inert and stable.
    - Extreme molecular complexity.

3. Siloxanes;
    - Mostly used as mixtures rather than pure fluids.
    - Isobaric condensation and evaporation are not isothermal and exhibit a certain glide.

4. Partially flouro-substituted straight chain hydrocarbons;
    - Several zero Ozone Depletion Potential fluids exists which are of interest.

5. Ethers and fluorinated ether;
    - Thermodynamically undesirable.
    - Flammability and toxicity issues.

6. Alcohols;
    - Thermodynamically undesirable.
    - Soluble in water.
    - Flammability issues.

7. Inorganics;
    - Operational problems.
    - Small environmental impact.
    - Inexpensive.

Even though the screening process covers a large number of fluids, only a few fluids are actually used in commercial plants. Hydrocarbons are the fluids with the most desirable thermodynamic properties and in practice, the flammability issues are managed by restricting the operating conditions. One of the hydrocarbon fluids, namely n-pentane, is the working fluid that is used in the 1 MW APS Saguaro PT plant in Arizona. The screening process of Bao and Zhao (2013) further concludes that R134a and R245fa are also possibilities for a solar application. These fluids have been used as working fluids on very small scale (<10 kW) solar applications. The saturation curves for the three possible working fluids are shown in figure 21.

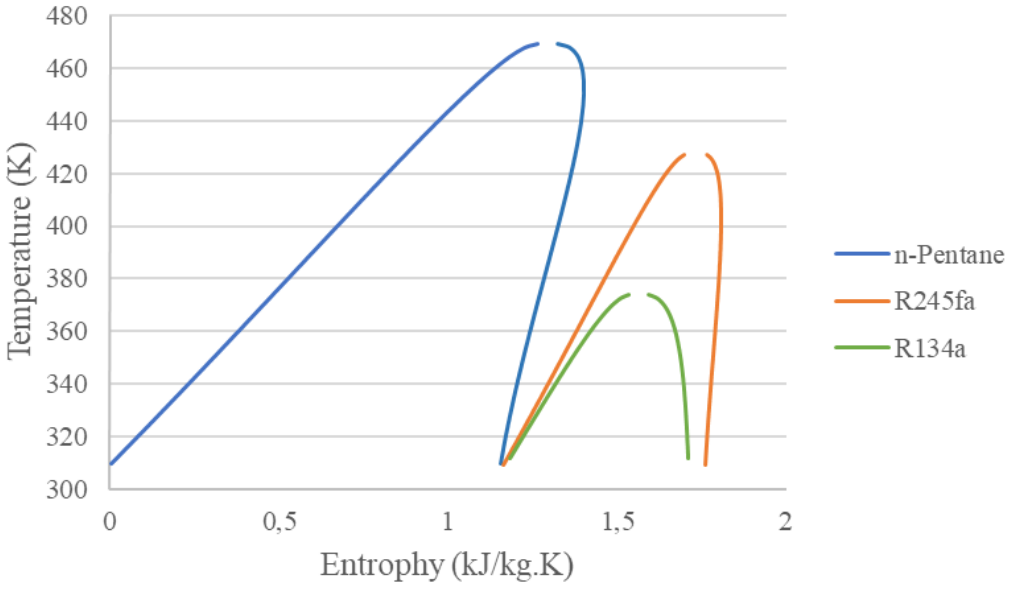

Figure 21: T-S diagram of typical organic fluids used in solar applications

Subsection 2.1.3 concludes that very little small scale solar powered ORC's exists in industry and seeing that n-pentane is the only fluid that has been successfully used on this scale for a solar application, this serves as the first argument to use n-pentane as working fluid in this analysis. For a second argument, table 10 gives a summary of how n-pentane relates to the selection criteria when compared to R134a and R245fa:

Table 10: N-pentane regarding the selection considerations

	Property/consideration	**Quantity/description**	**Relative weight**
Initial selection	Availability and cost	Locally and affordably available.	
	Non-flammable	NFPA 704 rating: 4; readily dispersed in air; will burn readily (Chemistry Reference, 2017).	
	Non-toxic	NFPA 704 rating: 1; (Chemistry Reference, 2017) .	
	Material compatibility	Compatible with all materials	
	Environmental benign	Quickly evaporates and biodegrades in soil (National Refrigerants Inc., 2015)	
	Thermal stability	NFPA 704 rating: 0; very stable	

	Property/consideration	Quantity/description	Relative weight
Selection according to thermodynamic properties, (all properties are evaluated at 25°C)	Vaporization latent heat	N-pentane: 365 kJ/Kg R134a: 178 kJ/Kg R245fa: 197 kJ/Kg	3 1 2
	Density	N-pentane: 620 kg/m^3 R134a: 1209.6 kg/m^3 R245fa:1339 kg/m^3	1 2 3
	Critical temperature	N-pentane: 197 °C R134a: 101 °C R245fa: 154 °C	3 1 2
	Boiling temperature (@1bar)	N-pentane: 36 °C R134a: -26.3 °C R245fa: 15.3 °C	3 1 2
	Molecular weight	N-pentane: 72.15 R134a: 102 R245fa: 134	1 2 3
	Viscosity	N-pentane: 0.217 mPa.s R134a: 12.06 mPa.s R245fa: 402.7 mPa.s	3 2 1
	Conductivity	N-pentane: 0.1112 W/mK R134a: 0.013 W/mK R245fa: 0.0125 W/mK	3 2 1
Total Weights		N-pentane: R134a: R245fa:	**17** **11** **14**

From the weighted totals, n-pentane proves to be the best choice as working fluid. That which is not sufficiently reflected in the weighted total is the difference in the boiling temperatures of the fluids and the difficulty to condense R134a and R245fa that have very low boiling temperatures. A system simulation for each of the three proposed ORC fluids for solar applications is done and in section 5.3 the above selection is confirmed. N-pentane will resultantly be taken as working fluid for the ORC and the properties of n-pentane can be seen in appendix A.

4.4.2 Power block layout

From the various power block plant layouts mentioned in subsection 2.2.2, the single pressure level cycle is always the first option for solar applications due to its simplicity and attainable efficiencies (Macchi & Astolfi, 2017). This layout is

commonly used in the commercial market while other configurations are proposed by literature for specific applications. The supercritical single pressure level cycle is not further developed than a few experimental setups hence due to maturity of technology the subcritical single pressure level cycle is the common choice (Macchi & Astolfi, 2017). A recuperator is added to the cycle to increase efficiency and the final chosen power block layout can be seen in figure 22.

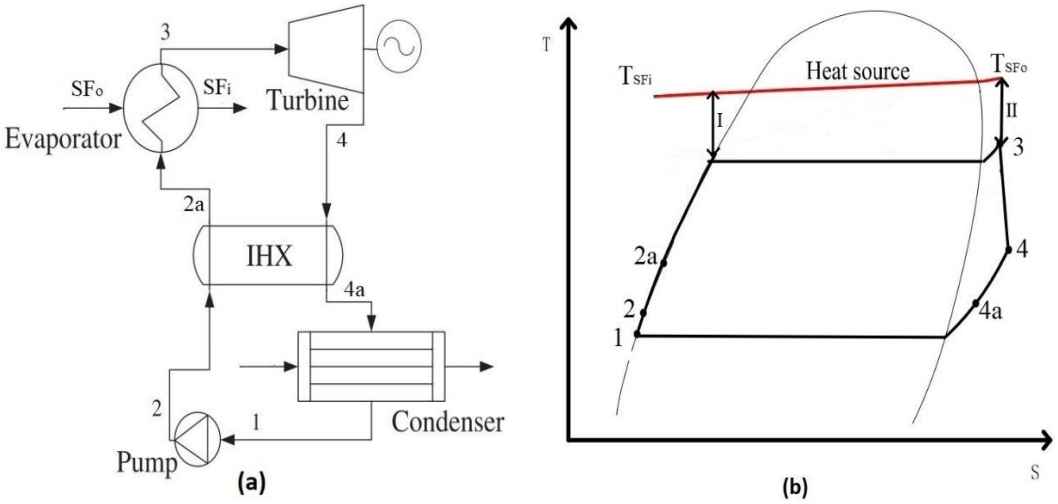

Figure 22: A schematic diagram of the ORC (a) with accompaning T-S diagram (b), (Guo et al., 2014)

An important parameter in the design of ORC's, is the pinch point temperature. The pinch point temperature is defined as the temperature difference between the heat source and the point of boiling inception in the evaporator. This temperature difference is shown with the double-headed arrow I in figure 22 and plays a significant role in the heat transfer performance (Wang et al., 2012). A detailed model to predict the location of the pinch point in the evaporator has been presented by (Guo et al., 2014) for cases where an optimal heat exchanger design is required. The simulation in chapter 5 varies the pinch point temperature and then obtains the pinch point with the best effect on overall system performance.

By defining a control volume over each component in the cycle, the conservation of energy and mass principles can be applied to each component at steady state conditions. After combining these individual models, a complete cycle model is achieved. Conducting energy and mass balances over each component, the analysis follow below.

4.4.3 Turbine

Macchi & Astolfi, (2017) defined a set of general correlations for the estimation of axial flow turbine isentropic efficiency specifically for ORC applications. They optimised several hundreds of turbines using similarity rules to present relations between the size parameter (SP), volume ratio (V_r) and specific speed (N_s). This

optimisation of parameters was done for single, two and three stage turbines. This non-dimensional approach allows for the comparison of optimal turbine designs based on specific parameters. The results obtained for a certain turbine stage can be extended to any other case if the turbines stages obey the following conditions (Macchi & Perdichizzi, 1977):

- All the geometrical ratios are equal.
- The flow is fully turbulent hence the Reynold number effects are negligible.
- The Mach numbers are similar.
- The specific speed is the same.
- The volumetric behaviour of the two fluids are the same, namely the volume flow rate variation across the stage is equal for both fluids. This condition is verified when both fluids are incompressible.

The parameters suggested as independent variables were defined as follow:

$$SP = \frac{\sqrt{\frac{\dot{m}_{out}}{\rho_{out}}}}{\sqrt[4]{\Delta h_{is}}} = \frac{\dot{V}_{out,is}{}^{0.5}}{\Delta h_{is}{}^{0.25}} \tag{4-72}$$

$$V_r = \frac{V_{out,is}}{V_{in}} = \frac{\rho_{in}}{\rho_{out}} \tag{4-73}$$

$$N_s = \frac{RPM}{60}\frac{V_{out,is}{}^{0.5}}{\Delta h_{is}{}^{0.75}} \tag{4-74}$$

These parameters were then used to optimize hundreds of turbines over a range of ORC applications. The optimizations were realized by assuming a ideal gas with an overall expansion coefficient value of 1.05 to represent a generic organic fluid. An in house turbine optimization tool named Axtur code was used by Macchi and Astolfi (2017) where every turbine stage is defined by nine parameters. The first three parameters define the stage quantities namely the isentropic degree of reaction (r^*), the isentropic loading coefficient (k_{is}) and the isentropic volume ratio (V_r). The other six parameters define the stage geometrical ratios (o/s, o/b and b/r_m) where three describe the rotor and the remaining three describe the stator. This approach conducted on a single stage axial flow turbine resulted in efficiency correlations that can be seen in figure 23.

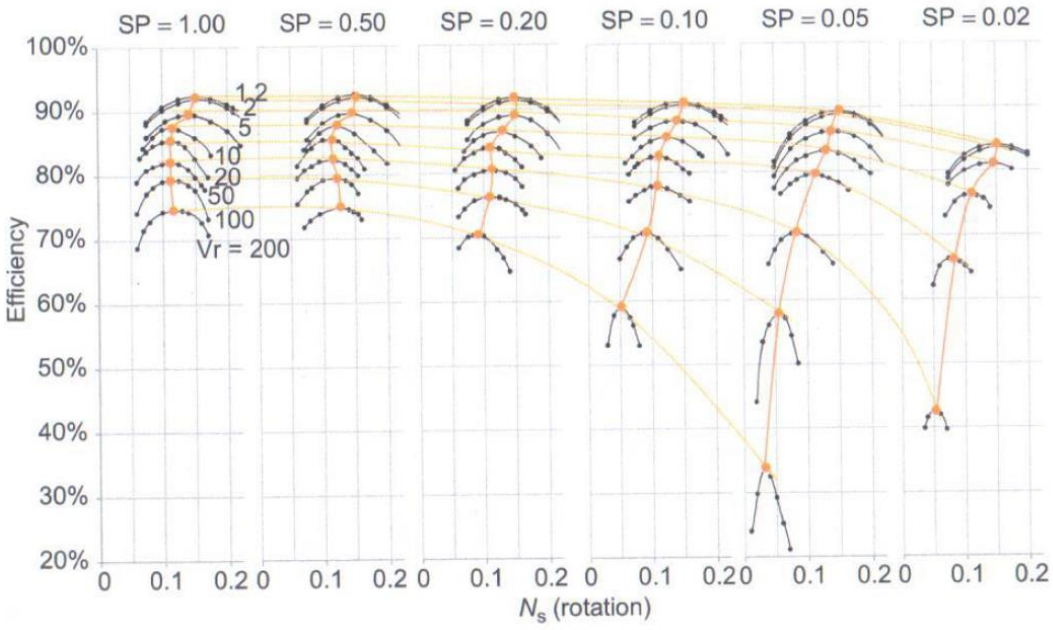

Figure 23: Resultant efficiency correlations for single stage ORC turbines, (Macchi & Astolfi, 2017)

In figure 23, the black markers show the optimal turbine configuration for each combination of SP, V_r and N_s. The red markers represent the turbine designs at optimal rotational speed for each combination of SP and V_r. Running the turbine at optimal rotational speed, Ns, and using equations 4-72 – 4-74, the turbine efficiency can be derived from figure 23. In terms of the isentropic mass flow rate the gross turbine power output is:

$$W_{gross} = \dot{m}_{PB,is}(h_3 - h_4) \tag{4-75}$$

Taking the generator efficiency as constant, the power output of the turbine can be calculated as follow in terms of the actual mass flow rate:

$$W_{gross} = \dot{m}_{PB}(h_3 - h_4)\eta_T\eta_{gen} \tag{4-76}$$

The pressure drop over the turbine is evaluated from known thermodynamic states by:

$$\Delta P_T = P_3 - P_4 \tag{4-77}$$

4.4.4 Evaporator

A plate type heat exchanger is chosen as evaporator due to its compactness and high heat transfer coefficients. The energy balance on the working fluid or power block side of the evaporator can be expressed as:

$$\dot{Q}_{PB,evap} = \dot{m}_{PB}(h_3 - h_{2a}) \tag{4-78}$$

While the energy balance on the HTF or solar field side is:

$$\dot{Q}_{PB,evap} = \dot{m}_{SF} Cp_{SF}(T_{SFi} - T_{SFo}) \tag{4-79}$$

Furthermore the available energy to the evaporator can be expressed in terms of the solar field efficiency that was defined previously in equation 4-1:

$$\dot{Q}_{PB,evap} = \dot{Q}_{in}\eta_{SF} \tag{4-80}$$

The log mean temperature difference over the evaporator is defined as:

$$\Delta T_{m,evap} = \frac{(T_{SFi} - T_3) - (T_{SFo} - T_2)}{\ln\left(\frac{T_{SFi} - T_3}{T_{SFo} - T_2}\right)} \tag{4-81}$$

The pressure drop in the evaporator needs to be overcome by the pump therefore, it is necessary to know what the pressure drop is. The pressure drop over the evaporator is very small in comparison to the pressure drop over the turbine and according to Macchi & Astolfi (2017) it is sufficient to assume typical pressure drops for the heat exchangers in systems analyses such as this. A typical pressure drop of 100 kPa is assumed for a plate type heat exchanger (Mechinox Heat Exchangers, 2018). The system sensitivity in variations of this typical value is shown in subsection 5.3.4.

$$\Delta P_{evap} = 100\ kPa \tag{4-82}$$

4.4.5 Condenser

Due to the scarcity of water where this system will be implemented, ACC is used. The advantages of using an ACC includes reduced maintenance costs and air-side fouling that is easier to handle than water side fouling and corrosion (Macchi & Astolfi, 2017). The heat that is rejected by the condenser is given by:

$$\dot{Q}_{PB,C} = \dot{m}_{PB}(h_{4a} - h_1) \tag{4-83}$$

Even though lower condensing temperatures are desired, the performance of an ACC is dependent on air temperature and limits the condensing temperature. A typical value for the initial temperature difference (ITD) is used and the effect on system performance by variations of this value is shown in subsection 5.3.4. According to (Pretorius & Du Preez, 2009) the typical ITD for an ACC is 27 °C.

A general relationship between the work required by the air-cooled condenser fan and the turbine power output is adopted where (O'Donovan, 2013):

$$W_{C,F} = 0.02 \times W_{gross} \tag{4-84}$$

The total pressure loss over the condenser, ΔP_C , is evaluated exactly the same way as that for the evaporator using a typical value and monitoring how sensible the system is towards this value. A typical pressure drop value for the working fluid side of the ACC is given by (O'Donovan & Grimes, 2015):

$$\Delta P_C = 1\ kPa \tag{4-85}$$

4.4.6 Recuperator

The recuperator removes some of the cooling load from the condenser and improves the system efficiency by re-utilising heat and rejecting less heat. The energy balance of the recuperator is given by:

$$h_{2a} - h_2 = h_4 - h_{4a} \tag{4-86}$$

A typical pressure drop according to (Macchi & Astolfi, 2017) is also assumed for the recuperator:

$$\Delta P_{rec} = 50\ kPa \tag{4-87}$$

4.4.7 Pump

Pumps used in the ORC industry are usually variable speed multistage centrifugal pumps. Their designs are relatively common as they are widely used also in the chemistry and refinery industries. The first fundamental parameter to analyse the performance of pumps is the mass flow rate. For the case of incompressible flow, it is more common to refer to volume flow rate. In the turbomachinery industry, volume flow rate is often referred to as capacity and is defined as:

$$\dot{V} = \frac{\dot{m}}{\rho} \tag{4-88}$$

The second fundamental parameter is the net head of the pump and is defined by the Bernoulli head between inlet and outlet of the pump (Çengel & Cimbala 2010):

$$H = \left(\frac{P}{\rho g} + \frac{V^2}{2g} + z\right)_{out} - \left(\frac{P}{\rho g} + \frac{V^2}{2g} + z\right)_{in} \tag{4-89}$$

For the case of incompressible flow through a pump, where the inlet and outlet diameters are identical and where there is no change in elevation from the pump inlet to outlet, equation 4-89 can reduce to (Çengel & Cimbala, 2010):

$$H = \frac{P_{out} - P_{in}}{\rho g} = \frac{\Delta P}{\rho g} \tag{4-90}$$

The useful power that is actually delivered to the fluid is termed the water horsepower and is proportional to the net pump head by following means (Çengel & Cimbala, 2010):

$$\dot{W}_{waterhorsepower} = \rho g \dot{V} H = \dot{V} \Delta P \tag{4-91}$$

Because of pump inefficiencies and internal irreversibilities the actual power supplied to the pump must be larger than the water horsepower hence a parameter called the brake horsepower or bhp is introduced which is the power supplied to the pump ($\dot{W}_{PB,pump}$). The resulting pump efficiency can then be calculated from (Çengel & Cimbala, 2010):

$$\eta_{PB,pump} = \frac{\dot{W}_{waterhorsepower}}{\dot{W}_{PB,pump}} \tag{4-92}$$

To calculate the pumping power required of the power block pump, the pressure drops in the turbine, evaporator and condenser needs to be accounted for. The work required for the power block pump is then:

$$W_{PB,pump} = \frac{\dot{V}\left(\Delta P_T + \Delta P_{evap} + \Delta P_C + \Delta P_{rec}\right)}{\eta_{PB,pump}} \tag{4-93}$$

5 Design Point Simulation

This chapter considers the determination of the design point of the SORC plant depicted in figure 24. The simulation is set up by using the theory provided in chapter 4. The methodology and simulation approach are first described after which all the constraints and simulation inputs are declared. The design point of the SORC is determined and the effect of certain parameters on the design point is discussed. The chapter ends off with showing, discussing and validating the simulation results.

5.1 Design point simulation methodology

In order to determine the optimized design point of the SORC plant proposed in figure 24, a thermodynamic optimization is conducted on the power plant.

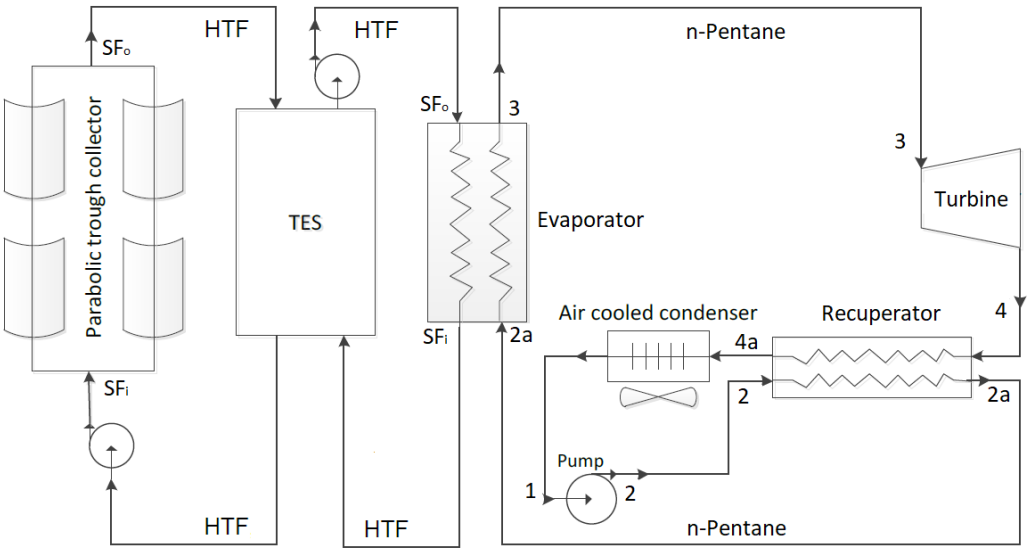

Figure 24: Simulation SORC plant schematic, adapted from (Saini et al., 2015)

The optimization is conducted under the assumption that at design point the TES is fully charged and all the heat coming from the solar field is absorbed by the ORC. The instance of solar noon at the first equinox is considered therefore solar tracking is also neglected in this optimization. The overall plant efficiency is used as objective function and defined as the ratio between the net power plant output for and the maximum received thermal heat. By modifying equation 4-2 the plant efficiency is:

$$\eta_{plant} = \frac{W_{net}}{\dot{Q}_{in}} \tag{5-1}$$

Taking into consideration that $\eta_{plant} = f(\eta_{PT}, \eta_{PB})$, a fundamental aspect of a SORC is that there exists an opposing trend between the efficiency and operating temperature of a PT collector (negative derivative – higher operating temperatures lead to lower efficiency) compared to the thermodynamic cycle (positive derivative – higher operating temperatures lead to higher efficiency). This implies that an optimum operating temperature exists where the best overall plant efficiency is achieved.

The independent decision variable that is typically used as optimizing variable in ORC's is the evaporating temperature considering that the condensing temperature is dependent on air temperature, (Macchi & Astolfi, 2017). By neglecting the thermal loss in the power block piping, the turbine inlet temperature will be equal to the evaporating temperature.

The optimization is split into two parts. Firstly, the whole range of operating conditions of a PT collector loop is defined by varying the solar field inlet temperature and HTF mass flow rate in the solar field separately as shown in figure B.1 in appendix B. For each combination of solar field inlet temperature and mass flow rate, the solar field efficiency, solar field outlet temperature and amount of heat gained are recorded.

Secondly, considering the power block, for each iteration of evaporating temperature, a range of solar field operating conditions exist to supply the correct heat at the correct temperatures and pressures for operations. Referring to figure 25, the possible solar field operating conditions are defined by the two for-loops and from among these the most efficient operating condition is chosen. By doing this, it is ensured that for each iteration of evaporation temperature, the solar field is also optimized.

All model equations are solved sequentially for the power block following the procedures as demonstrated in figure 25. With the black-box optimization approach the most efficient plant design according to equation 5-1, is determined. The numerical calculations are carried out for the turbine output range of 500 kW – 5 MW at full load for each turbine output case, using MatLab as simulating software.

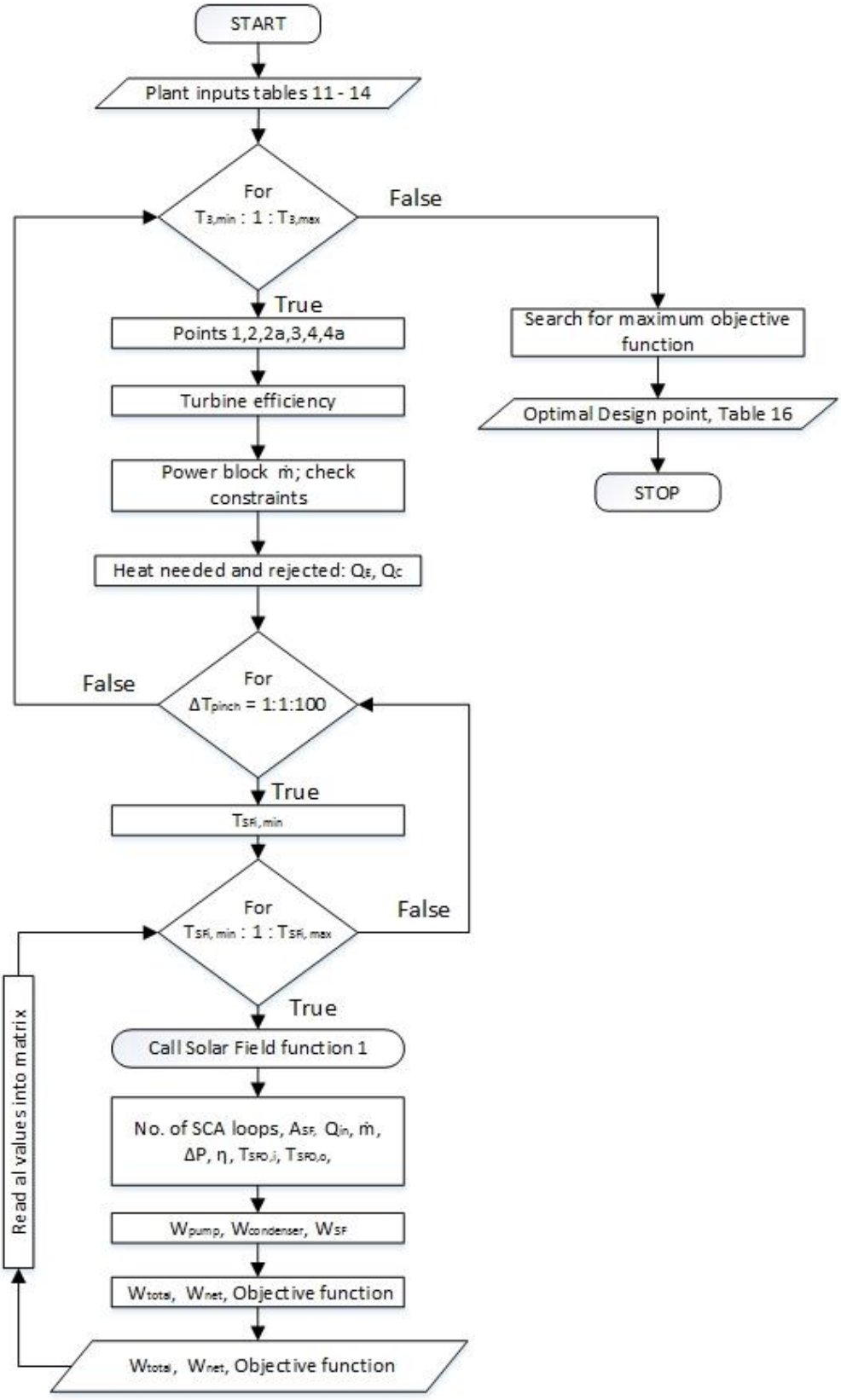

Figure 25: Design point simulation main function

5.2 Input data

According to (Macchi & Astolfi, 2017) it is sufficient to assume typical values for pressure drops, temperature differences, mechanical efficiencies etc. on the basis of best design practice if the focus of the work is on the overall cycle and not on detail component design. These typical values together with simulation constraints, constants, and data derived values are listed in tables as the input parameters for the various components of the SORC plant.

The optimization constraints and constants are listed in table 11. The constraints are due to the working fluid property constraints and component material characteristics. N-pentane's critical temperature and critical pressure serves as upper constraints for the power block in the simulation. The HTF fluid properties serve as constraints for the solar field in the simulation. The lowest possible condensing temperature is desired but is limited by the ACC. The condensing temperature is set as a constant value at the lowest possible temperature by the ACC. The maximum mass flow rates are limited by the plate type heat exchanger.

Table 11: Design point simulation constraints and constants

	Parameter	**Quantity/Description**	**Reference**
Temperature	Maximum evaporation	N-pentane: 197 °C R134a: 101 °C R245fa: 154 °C	Table A.1 – A.3
	Minimum evaporation	T_{cond} + 2 °C	N/A
	Condensing	T_{air} + 27 °C	(Pretorius & Du Preez, 2009)
	Maximum solar field	345 °C	Table A.4
	Minimum solar field	-3 °C	Table A.4
Pressure	Maximum power block	N-pentane: 3.37 MPa R134a: 4.0 MPa R245fa: 3.7 MPa	Table A.1 – A.3
	Maximum solar field	4.1 MPa	(SCHOTT Solar CSP GmbH, 2013)
Mass flow rate	Maximum solar field	190 kg/s	(Mechinox Heat Exchangers, 2018)
	Maximum power block working fluid	190 kg/s	(Mechinox Heat Exchangers, 2018)

	Parameter	Quantity/Description	Reference
Constants	σ	5.67×10^{-8} W/m^{2}K^4	N/A
	g	9.81 m/s^2	N/A
	g_c	1	N/A
	Error Margin	1×10^{-3}	N/A

The input parameters that are used for the design point simulation are categorised in metrological inputs, solar field inputs and power block inputs. The metrological input parameters are described in table 12 for the chosen site of Aggeneys. Aggeneys reaches solar irradiation values of up to 1122 W/m^2 in summer, but the data is presented for the first solar equinox to achieve a more realistic design point, (SODA, 2014). Three years of weather data is freely available and instead of choosing a specific year the average of the three years is taken.

Table 12: Metrological input parameters

	Parameter	Quantity/Description	Reference
Metrological conditions	Site:	Aggeneys	N/A
	Solar time:	Solar noon	N/A
	Time of year:	First solar equinox, 20 March	N/A
	Solar Irradiation:	884 W/m^2	(SODA, 2014)
	Air Temperature:	31.5 °C	(SODA, 2014)
	Sky Temperature:	0 °C	Assumed
	Wind direction 10 m above ground (0° means from North, 90° from East etc.):	314°	(SODA, 2014)
	Wind speed 10 m above ground:	4.4 m/s	(SODA, 2014)
	Air Properties	Multiple	(NIST, 2017)

The SORC input parameters needed for the solar field regarding the PTC module, receiver tube and optical efficiency parameters are described in table 13.

Table 13: Solar field input parameters

	Parameter	Quantity/Description	Reference
	Differential increment size	1 m	Design choice
	HTF:	Therminol 66	Table A.4
	Solar field pump efficiency	0.85	(Yilmaz & Söylemez 2014)

	Parameter	Quantity/Description	Reference
PTC Module	Collector:	Ultimate Trough	(Riffelmann et al., 2014)
	Collector aperture length:	7.51 m	
	Length of single collector module:	24.5 m	
	Number of modules per SCA	10	
	Length of SCA	245 m	
Receiver	Receiver type:	Schott PTR 70	(SCHOTT Solar CSP GmbH, 2013)
	Absorber tube material:	Steel type: DIN 1.4541	
	Surface roughness	0.002 mm	(Çengel & Cimbala, 2010)
	Absorber tube inside diameter:	0.066 m	(SCHOTT Solar CSP GmbH, 2013)
	Absorber tube outside diameter:	0.07 m	
	Absorber tube thermal conductivity:	15 W/m.°C	(Thyssenkrupp, 2017)
	Absorber tube emissivity:	0.095	(SCHOTT Solar CSP GmbH, 2013)
	Absorber tube absorptance:	0.96	
	Glass cover material:	Borosilicate glass	(SCHOTT Solar CSP GmbH, 2013)
	Glass cover inside diameter:	0.12 m	
	Glass cover outside diameter:	0.125 m	
	Glass cover thermal conductivity:	1.2 W/m °C	
	Glass cover emissivity:	0.86	
	Glass cover absorptance:	0.02 (Anti reflective coating)	
	Glass cover transmittance:	0.97	
Optical efficiency	Clean mirror reflectance:	0.94	(Riffelmann et al., 2014)
	Tracking error, e_{tr}	0.994	
	Geometry error, e_{ge}	1	
	Dirt on mirrors, e_{dm}	0.97	
	Dirt on receivers, e_{da}	0.995	(Yilmaz & Söylemez, 2014)
	Receiver shadowing, e_{sh}	0.98	
	Unaccounted error, e_{un}	0.96	

The input parameters regarding the power block are described in table 14, noting that typical pressure drops were taken for the evaporator, condenser and recuperator and that the ACC ITD is fixed. A plate type heat exchanger is chosen as evaporator and according to (Shah & Sekulić, 2003) the temperature approach can be as low as 1 °C in a plate type heat exchanger.

Table 14: Power block input parameters

Parameter	**Quantity/Description**	**Reference**
Gross power output:	500 kW_e – 5 MW_e	
ACC fan work	0.02 × Gross power output	Subsection 4.4.5
Pump efficiency:	0.75	(Madhawa Hettiarachchi et al., 2007)
Generator efficiency:	0.96	
Working fluid:	N-pentane	Table A.1
Evaporator type:	Plate type heat exchanger	Subsection 4.4.4
Evaporator pressure drop:	100 kPa	(Mechinox Heat Exchangers, 2018)
Condenser working fluid side pressure drop:	1 kPa	(O'Donovan & Grimes, 2015)
Recuperator pressure drop:	50 kPa	(Macchi & Astolfi, 2017)
Evaporator minimum temperature difference	1 °C	(Shah & Sekulić, 2003)

5.3 Results

5.3.1 Solar field results

The range of operating conditions of a PT collector loop was defined by varying the solar field inlet temperature and solar field mass flow rate. The operating conditions were defined in temperature increments of one. The results of this first part of the simulation for three solar field inlet temperatures can be seen in figure 32 on each graph. The effect of the mass flow rate on different parameters is shown in the different figures and all solar field results are validated with hand calculations in appendix C.1 and C.2.

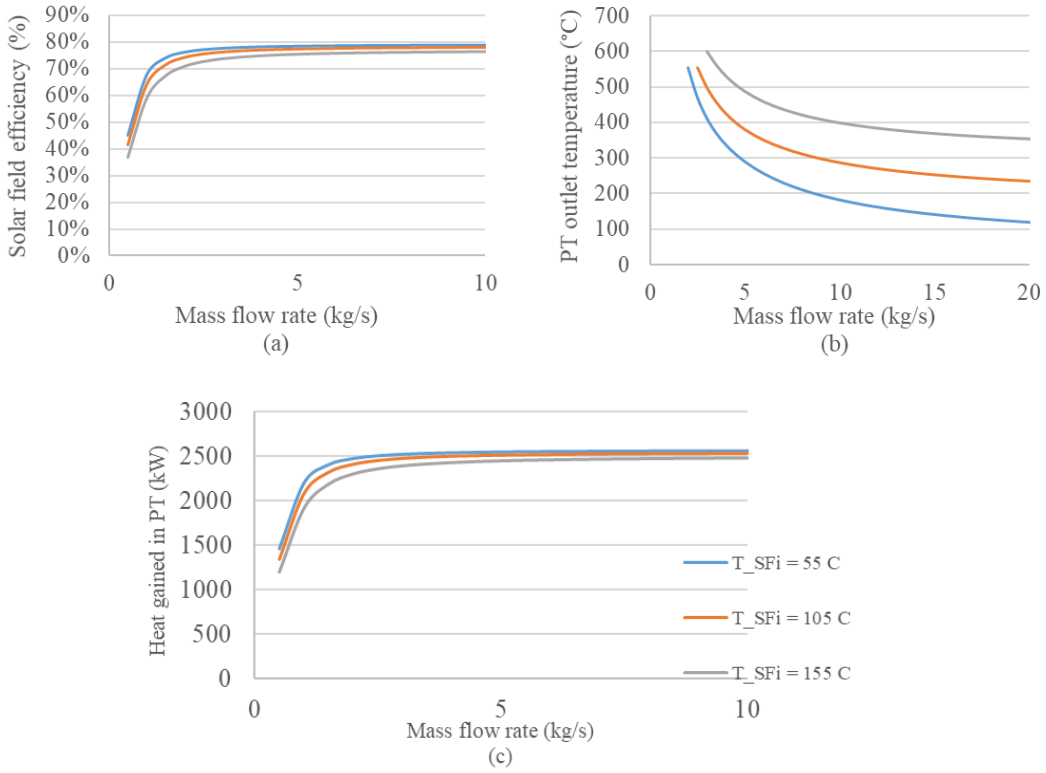

Figure 26: The effect of the solar field mass flow rate on PT collector efficiency (a), PT outlet temperature (b) and heat gained (c) for different inlet temperatures

From figure 26 (a) and (c) it can be concluded that a higher mass flow rate is desired for better solar field performance as the efficiency and heat gained increases with the increase in mass flow rate. Initially the increase in efficiency and heat gained is steep but flattens out very quickly. In figure 26 (b), it is shown that as the mass flow rate increases, the PT collector outlet temperature decreases. In all cases in figure 26, it can be seen that the lowest possible solar field inlet temperature is desired. Also in figure 26 (b), the maximum allowed solar field temperature constraints the mass flow rate at a minimum value which is about 3 kg/s for the solar field inlet temperature case of 155 °C. In figure 26 (a) and (c) this mass flow rate minimum values are overwritten to extrapolate the effects of the mass flow rate on PT collector performance. The constraints are applied in the actual simulation.

Not shown in the figures, but as the mass flow rate of the solar field increases, the pressure drop also increases requiring more pumping power to overcome the pressure drops. An increased mass flow rate has a positive effect on the solar field thermal efficiency but a negative effect on the net power output as more power is consumed by the solar field pump. By defining all the possible operating conditions for the PT loop, the best operating point of the solar field can be chosen where the solar field thermal efficiency and the work consumed by the solar field pump are weighed off against each other to ensure the best effect on the total system performance.

5.3.2 Comparison between working fluids

After defining the solar field operating conditions, a thermodynamic optimization is conducted on the SORC plant where the plant efficiency is used as the objective function. The gross power output is set to vary from 500 kW_e to 5 MW_e by changing the turbine size and running at full load for every defined power output. The exact same simulation is done for all three proposed SORC fluids in subsection 4.4.1. The SORC plant efficiency and net power output are shown in table 15 for each instance.

Table 15: Resulting optimized plant efficiencies with nett power output

Turbine power output (kW)	N-pentane		R134a		R245fa	
	Nett output (kW)	SORC plant efficiency	Nett output (kW)	SORC plant efficiency	Nett output (kW)	SORC plant efficiency
500	442.0	12.7 %	354.4	4.7 %	435.8	9.4 %
1000	875.3	12.8 %	685.3	4.6 %	872.1	9.4 %
2000	1775.7	12.7 %	1330.5	4.3 %	1725.8	9.3 %
3000	2664.8	12.6 %			2571.7	9.2 %
4000	3538.5	12.6 %			3406.2	9.2 %
5000	4404.8	12.5 %			4229.4	9.1 %

In table 15, a screening of different working fluids is presented and the results of the screening methods proof that the result of the working fluid selection guideline in subsection 4.4.1 correct. This indicates that n-pentane is for every instance in this simulation the best working fluid choice as concluded by the higher SORC plant efficiencies. One of the reasons for n-pentane showing the higher efficiency, is that n-pentane has the highest critical temperature of the three fluids and this results in a bigger temperature difference over the turbine. The effect of the turbine inlet temperature for the 1 MW_e gross power output case is shown in figure 27 for the three fluids.

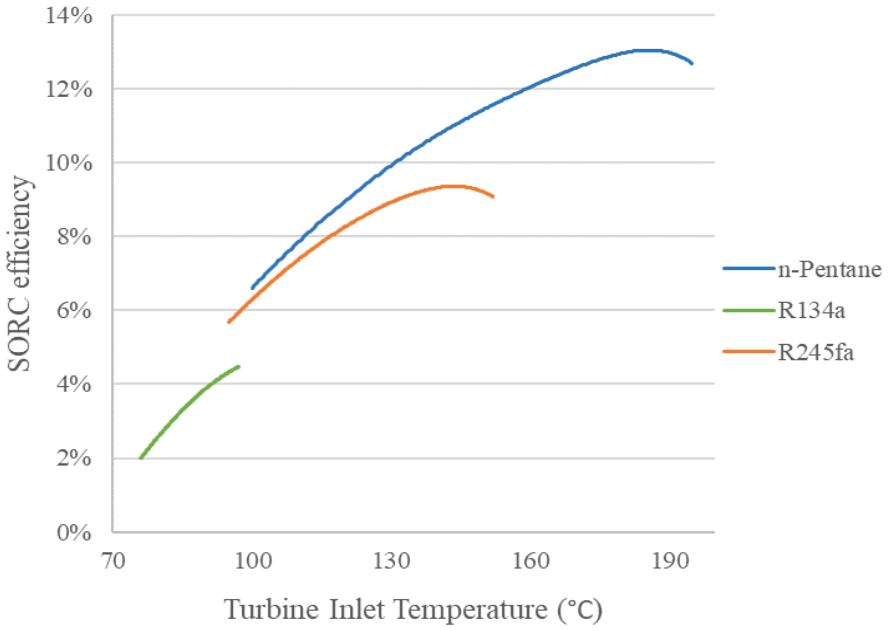

Figure 27: Effect of turbine inlet temperature on plant efficiency for a 1 MWe turbine output

The opposing trend between the effects of operating temperature of the power block and the solar field can be seen in figure 27 for n-pentane and R345fa. In the case of R134a, the turbine inlet temperature remains low enough for the solar field not to enter the adverse effects of high temperatures hence no decline in efficiency is seen at the higher temperatures of R134a. For the most part the higher the operating temperature, the higher the SORC efficiency but at the highest temperatures of each fluid it evidently shows how the SORC efficiency decreases when the operating temperature increases. This is where the adverse effect of high temperatures in the solar field outweighs the beneficial effects in the power block. The design point with the highest efficiency is resultantly reached at a certain temperature. For n-pentane, the 1 MW_e gross power output results in the highest SORC efficiency of 12.8 % and will therefore be defined as the design point.

5.3.3 Design point conditions

Through the thermodynamic optimization, the design point for the proposed SORC is calculated. The design point is achieved at a turbine inlet pressure and evaporating temperature of 2858.8 kPa and 186 °C respectively. The solar field area is 7718.2 m^2 and the solar field inlet and outlet temperatures are 93 °C and 233.1 °C respectively. All design point results are verified with hand calculations done on SMath Studio in Appendix C.3 and C.4.The T-S diagram for the design point is shown in figure 28 with the solar field heat source temperatures added.

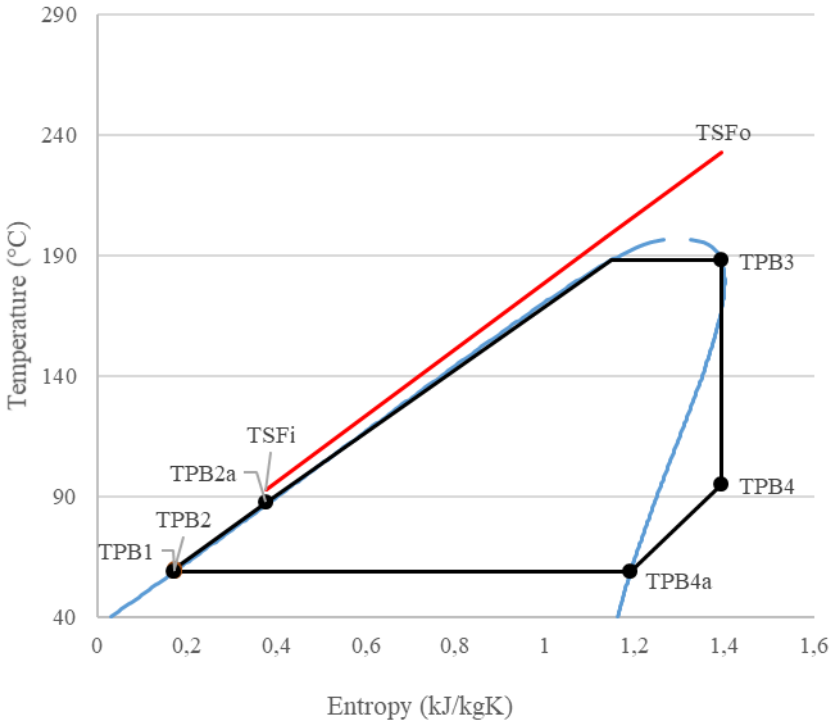

Figure 28: Design point T-S diagram

In figure 28, the temperature approach between the working fluid and the HTF in the evaporator can be seen. The temperature approach occurs at the working fluid inlet side between T_{SFi} and T_{PB2a}. The temperature values of figure 28 together with the full set of optimal design results are shown in table 16.

Table 16: Design point simulation results

Parameter		Design point value
SORC	Objective function	12.8 %
	Turbine power output	1000 kW_e
	Net power output	875.3 kW_e
Power Block	T_{PB1}	59 °C
	T_{PB2}	60 °C
	T_{PB2a}	88 °C
	T_{PB3}	186 °C
	T_{PB4}	95.7 °C
	T_{PB4a}	59 °C
	ΔT_{pinch}	10 °C
	P_{PB3}	2858.8 kPa
	P_{PB1}	207.54 kPa
	$\dot{m}_{PB}$	12.4 kg/s
	η_{PB}	18.7 %

Parameter		Design point value
Solar Field	T_{SFi}	93 °C
	T_{SFo}	233.1 °C
	$\dot{m}_{SF}$	18.5 kg/s
	$\dot{m}_{SF,loop}$	8.8 kg/s
	SCA_{loops}	2.1
	$SCA's$	4.2
	A_{SF}	7718.2 m^2
	η_{SF}	78.5 %
	η_{tube}	95.3 %
	η_{opt}	82.3 %

With the HTF mass flow rate achieved in the PT Collector, the assumed turbulent flow in subsection 4.2.3 is confirmed. The achieved power block conversion efficiency of 18.7 %, is a bit more conservative than the 20.7 % built-in power block efficiency of the System Advisor Model (SAM 2017.9.5) for a 1 MW_e SORC turbine. The SAM power block efficiency is based on empirical results.

The achieved PT collector optical efficiency of 82.3 % compares well to the peak optical efficiency of 82.7 % achievable by the Ultimate Trough collector as stated by the developers, FLABEG GmbH, (Riffelmann et al., 2014). The sensitivity of the SORC plant regarding certain input parameters are evaluated next in order to analyse the robustness of the model and to get a broader picture of the capabilities of a SORC.

5.3.4 Sensitivity analysis

The first sensitivity analysis regards the input parameters taken as typical values found in literature as well as the assumed values. The purpose of this analysis is to determine what influence these input parameters have on the outcome of the simulation. The analysis considers what percentage of change the total plant efficiency experiences for a certain percentage of change in the input value. While the input parameter is varied, all other inputs are kept constant. The optimization is started again for the changed input parameter and a new design point is calculated. The change in the new design point is recorded. The results are recorded in table 17.

Table 17: Input parameter sensitivity

Input parameter	Change of input parameter	Difference in SORC plant efficiency
Typical pressure drops	+ 20 %	- 0.02 %
Sky temperature	- 10 °C	0 %
Condenser ITD	+ 10 %	- 0.26 %

The conclusion from the first sensitivity analysis is that the assumed value for sky temperature does not have a big influence on the SORC efficiency. The typical values from literature used for pressure drops and the ITD in the condenser also has little effect on the outcome of the simulation.

The second sensitivity considers what effect the change in weather conditions have on the plant efficiency. The purpose of this analysis is to obtain a better understanding of whether a SORC can be successfully deployed in various areas. For this analysis, the design point conditions are kept constant as presented in subsection 5.3.3 and the effect of changing weather conditions are recorded. The results are shown in table 18.

Table 18: Metrological conditions sensitivity

Input parameter	**Percentage change of input parameter**	**Effect on SORC plant efficiency**	**Effect on net power output**
Air temperature	+ 10 %	- 0.26 %	- 0.2 %
Irradiation	- 10 %	- 0.02 %	- 9.6 %
Wind speed	+ 10 %	0 %	0 %

In table 18 it is evident that the variation in irradiation has a significant effect on plant performance as can be expected for a CSP system. As for a change in irradiation, the plant efficiency does not change remarkably. As the irradiation decreases the net power produced by the system decreases in more or less the same ratio. From the definition of plant efficiency the efficiency therefore does not change remarkably. The air temperature and wind speed has negligible effects on system performance.

The optimum design point with all the working condition of the proposed SORC plant is determined in this chapter. The plant however deviates from the optimal design point as the solar resource goes through alterations during the day (from morning to noon). It is therefore necessary to simulate the SORC over a period of a year as will be done in chapter 6.

6 Annual Simulation

In this chapter, the SORC is simulated over a period of one year to determine the annual electricity production, capacity factor and LCOE of the plant. This will assist in proposing the technology for a specific purpose. The simulation methodology is first described after which the input parameters are listed. Thereafter the chapter ends off with showing, discussing and validating the simulation results.

6.1 Annual simulation methodology

In order to determine the annual net electricity generation, E_a, and the capacity factor the plant simulation needs to run over a period of one year. The annual net electricity generated is an important parameter in LCOE calculations used to determine the economic feasibility of SORC's.

The annual simulation of a SORC plant necessitates the definition of a control strategy. To simplify the control, all the HTF from the solar field is dumped into the TES and from the TES the HTF is pumped to the evaporator of the ORC at constant temperature. Further details about the operating strategy entails:

- When DNI reaches 100 W/m^2 collectors are set to tracking.
- After every period of no production, the first 0.5 hours of DNI is used to warm up the SORC and cannot be captured in TES or used for electrical generation (Ruegamer et al., 2013).
- The ORC is engaged for an hour if there is an hour of storage in the TES.
- When the TES is fully charged, the solar field defocuses a number of PT collectors but the TES level is maintained.

The solar multiple (SM) and TES size are still two unknowns that needs to be determined. This is done by varying the SM and TES sizes separately and calculating the capacity factor and LCOE of the SORC plant for each combination of SM and TES size. The LCOE is based on weighted cost average and is thus a widely accepted metric for comparing different energy sources. This is however a difficult metric to accurately calculate for the following reasons (O. O. Craig et al., 2017):

- The CSP LCOE can be country specific.
- It is very difficult to obtain the latest cost information for existing plants.

- Different cost information structures exist for different plants with regards to the manufacturing and are often kept confidential.

The LCOE is defined by (O. O. Craig et al., 2017) as:

$$LCOE = \frac{CRF \times CAPEX_{total} + OPEX_{total} + k_{fuel}}{E_{e,a}} \quad (6\text{-}1)$$

where the capital recovery factor (CRF) is defined as:

$$CRF = \frac{k_d(1+k_d)^n}{(1+k_d)^n - 1} + k_{insurance} \quad (6\text{-}2)$$

The values for the parameters in equations 6-1 and 6-2 are listed in table 19 with all the other simulation inputs.

6.2 Input data

The various input parameters for the annual simulation are listed in table 19. Regarding the metrological conditions for Aggeneys, the DNI data is taken as an average over the years 2004, 2005 and 2006 as this was the only data that could be freely obtained. For the purposes and scope of this thesis, the three-year average is deemed sufficient. Furthermore, the calculated design point conditions from subsection 5.3.3, are taken as inputs noting that the solar field efficiency will vary as the hour of the day changes. In reality the solar field size can only be multiples of an integer number of PT collector assemblies and this is incorporated in the simulation by taking the next largest integer number of PT collector assemblies.

The economic parameters used was obtained from the different most applicable sources. Seeing that most of the technology of the SORC is not locally produced, the specific technological cost was taken at international standard. The power block CAPEX is determined by cost models developed specifically for ORC's. The power block OPEX costs are given as estimates by ORC manufacturers. Regarding the TES, thermocline specific costs are presented.

The CAPEX cost for the site preparation is calculated per meter squared. In order to calculate the total site area the formula as in SAM (2017.9.5) software is used:

$$A_{site} = A_{SF} \times \frac{row\ spacing}{max\ aperture} \times Nonsolar\ field\ area\ multiplier \quad (6\text{-}3)$$

with $row\ spacing = 15m$ and $Nonsolar\ field\ area\ multiplier = 1.4$

Table 19: Annual simulation input data

	Parameter	Quantity/Description	Reference
Metrological	Site	Aggeneys	N/A
	Longitude	18.7987507	(SODA, 2014)
	Latitude	-29.2607537	
	Time Zone:	UTC +2 (30°E)	
	Daylight savings time	0	
	DNI	Three year average	
SORC Plant	Turbine output	1 MW_e	Table 16
	Nett power output	875.3 kW_e	Table 16
	Design solar field area	7718.2 m^2	Table 16
	η_{PB}	18.7 %	Table 16
	η_{tube}	95.3 %	Table 16
	η_{TES}	99 %	(Ma et al., 2012)
Economic data	$CAPEX_{Siteprep}$	20 $/$m^2$	(Mehos et al., 2016)
	$CAPEX_{SF}$	190 $/$m^2$	(Mehos et al., 2016)
	$CAPEX_{Rec}$	50 $/$m^2$	Mehos et al., 2016)
	$CAPEX_{PB}$	692 $/kW	(Saini et al., 2015)
	$CAPEX_{TESS}$	25 $/$kWh_{th}$	(Mehos et al., 2016)
	$OPEX_{fixed}$	0.05 % × $CAPEX_{PB}$	(Senechal, 2014)
	Lifetime and depreciation rate, n	30	(Sklar-Chik & Brent, 2017)
	k_d	10 %	(Madaly, 2014)
	$k_{insurance}$	0.5 %	Assumed
	k_{fuel}	0	N/A

6.3 Results and validation

6.3.1 Capacity factor results

In figure 29 it is evident that the SORC capacity factor increases as the SM and TES size increases. The larger the TES size, the bigger impact the SM has on the capacity factor for the plant. The plant almost reaches maximum capacity factor with 14 hours TES as a very small increase in capacity factor exists between the 14 hours and 18 hours TES. The main advantage of TES is to enable electricity production during night for which 14 hours of TES is enough. With 14 hours TES, the SORC can reach a capacity factor of about 83 %. During summer months the SORC plant can run at full capacity but during winter months it is not possible. Seeing that mines operate 24 hours per day all year round, this indicates the technology cannot be considered for baseload generation in an off-grid applications and auxiliary energy sources is still necessary.

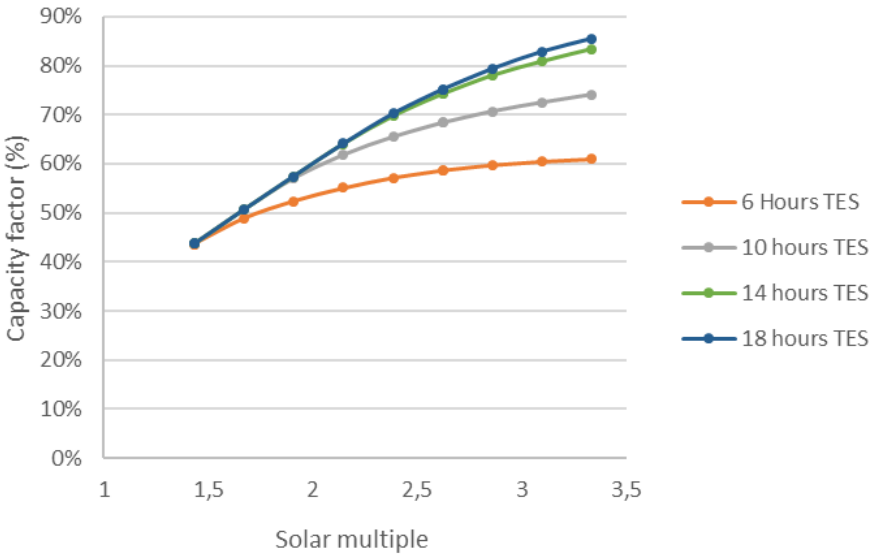

Figure 29: The SORC capacity factor for different TES sizes and SM's

6.3.2 LCOE results

From figure 30 the lowest achievable LCOE is 16.7 $c/kWh at a SM of 1.7 and TES size of 6 hours. For this specific case, the plant has a capacity factor of about 50 %. The second lowest LCOE value of 17.0 $c/kWh is found at a SM of 2.1 and 10 hours TES. A much higher capacity factor of 62 % is achieved at these conditions. SORC's will therefore be more competitive with non-base load production applications. The range of LCOE values can be seen in figure 30.

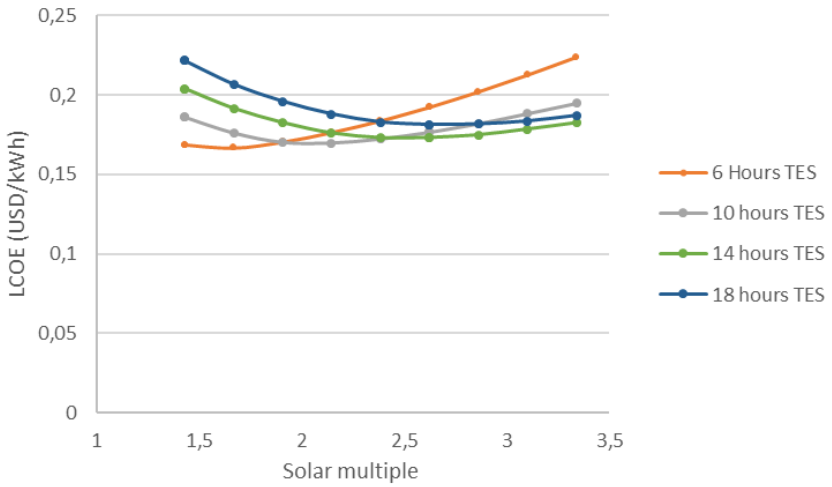

Figure 30: The SORC LCOE values for different TES sizes and SM's

For the case of the lowest achieved LCOE (6 hour TES), a further inspection is given into the energy production for specific days in order to pin down the capabilities of a SORC.

6.3.3 Solstices energy production

To better understand the suitability and determine the operating parameters where SORC will be most competitive, it is useful to look at a typical day's electricity generation. In figures 31 and 32 the daily operation for summer solstice and winter solstice are displayed respectively for the lowest LCOE value parameters and a discussion of the figures follow. The solar energy collected by the solar field, the thermal energy as received by the evaporator and the power produced are shown on the figures as the day progresses.

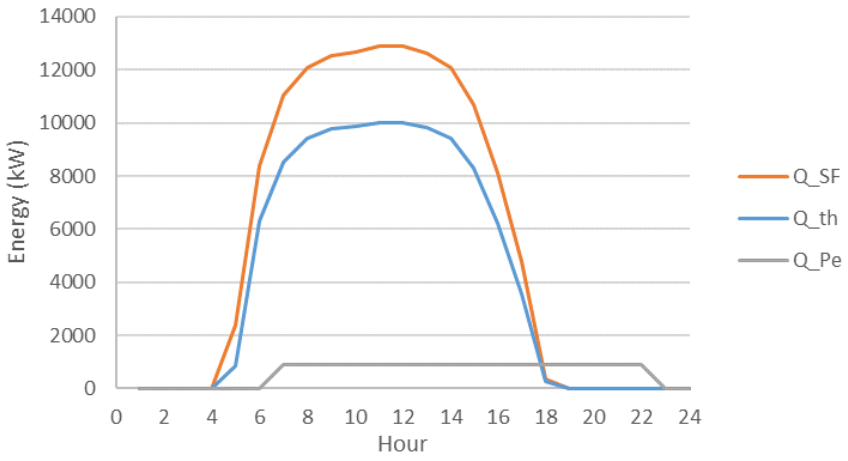

Figure 31: Summer solstice – 22 December

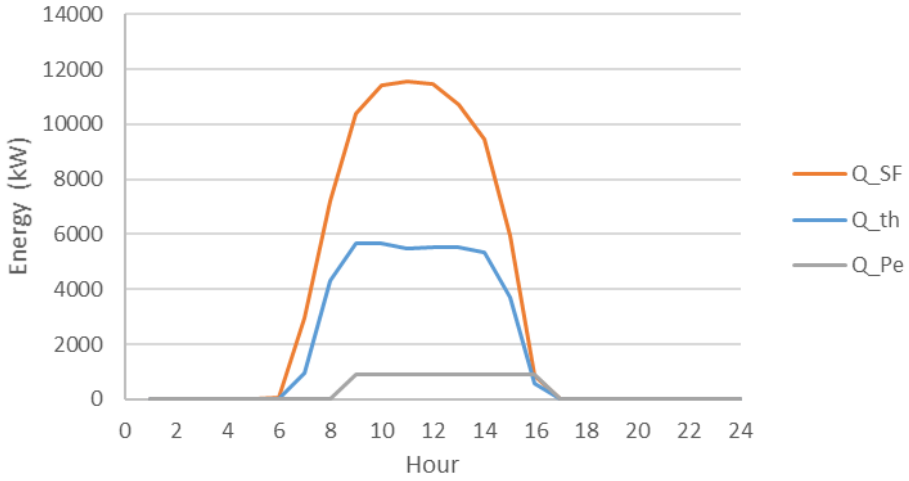

Figure 32: Winter solstice – 21 June

In figure 31, it is clear that the SORC can produce electricity for 15 hours of the day and that number reduces to 8 hours in mid-winter as shown in figure 32. The electrical production during the summer months might be sufficient to meet the demand but having only 8 hours of electricity during the winter months will necessitate the use of more auxiliary energy sources. It might make sense to increase the SM as it is evident that a large amount of storage is not being utilised. In figure 33, it is shown that the TES level just surpasses the 20 % mark during the winter solstice. For the case of a SM of 2 and 10 hours TES where the second lowest LCOE is achieved, the plant can produce electricity for 20 hours during summer and 9 hours during winter.

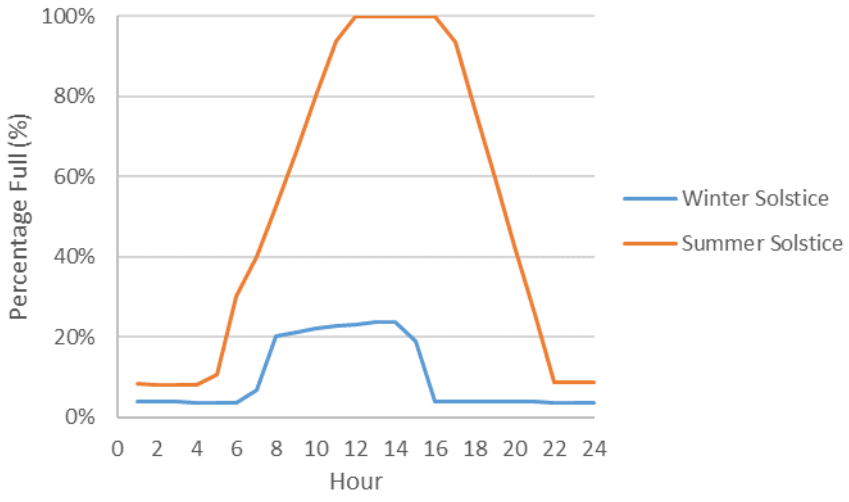

Figure 33: TES level monitoring

6.3.4 Annual simulation validation

A simulation model for a 1 MW_e SORC plant is set up in the free software SAM, to validate the annual simulation results. The model is set up by using the empirical model choice that uses a set of curve-fit equations derived from real data measured at a relevant plant. The SAM model can be customised to simulate a similar plant as discussed in chapters 5 and 6.

The model is set up using the 1 MW_e APS ORC turbine with a recuperated and wet cooling cycle and combined with a PT. The Ultimate Trough with Schott PTR70 receiver is implemented for the solar field. Data specific to Aggeneys is used as weather input file to the simulation. The model is set up for a SM of 1.7 and TES of 6 hours. A detailed documentation of the input parameters of the SAM model is shown in appendix D and a summary of the results are presented in table 20.

Table 20: Annual simulation validation

Metric	**Annual Simulation**	**SAM**	**Difference**
LCOE ($c/kWh)	16.7	17.9	6.7 %
Capacity factor (%)	48.8	41.4	15.2 %

Slight differences exist between the results of the SAM and developed model with the biggest difference in the capacity factor. The SAM model produces a higher LCOE value and lower capacity factor. One explanation for the difference in the capacity factor is the difference in PT tracking strategy. Seeing that the SAM model uses data from an existing plant, the PT collectors are set to start tracking only after the second hour of DNI. The developed model uses the operating strategy where collectors are set to tracking when DNI reaches 100 W/m^2. For the SAM model, the result is less thermal energy absorbed by the solar field and subsequently less power produced when compared to the developed model.

The power block conversion efficiency used by the SAM model is 2 % higher than that of the developed model. Resultantly more electricity is produced per unit of thermal energy received by the power block when compared to the developed model. However, the effect of the difference in tracking strategy has a bigger influence on the total produced electricity that in turn influence the capacity factor. Other smaller factors contributing to the difference in the models, is the difference in TES incorporated. The SAM model can only incorporate a two-tank TES with a PT plant; therefore, the thermal losses associated with storage is more. This in turn contributes to the lower capacity factor of the SAM model. The annual simulation results and the applicability thereof, is further discussed in support of concluding the thesis in the next chapter.

7 Conclusion

In this chapter, the thesis concludes by starting with a discussion of the results of the design point and annual simulation. Thereafter recommendations for future work to continue the study of small-scale SORC's are given. The conclusion of the thesis is reached by evaluating the objectives and making a conclusion based on the research question.

7.1 Discussion of results

The design point of the SORC simulation was obtained through a thermodynamic optimization. By comparing three possible working fluids that was suggested in literature for solar applications, the best working fluid for a SORC plant in the range of 500 kW_e – 5 MW_e was found to be n-pentane. A SORC is most efficient for a turbine output of 1 MW_e and reached an efficiency of 12.8 %. The design point results showed good correlation with existing data from field tests done by other researchers and formed the frame work to conduct the annual simulation on the SORC.

The annual simulation considered a one year operation of the SORC with weather data averaged over three years for the Black Mountain mine near Aggeneys. The TES size and SM were chosen as design variables and the lowest LCOE value obtained was 16.7 $c/kWh at a SM of 1.7 and TES size of 6 hours. The second lowest LCOE value of 17.0 $c/kWh is found at a SM of 2.1 and 10 hours TES. For the case of the lowest LCOE value the plant can only operate for 8 hours at winter solstice. For the second lowest LCOE value the operating hours for winter solstice is 10 hours. A SAM model was used to validate the results and with the SAM model a LCOE of 17.9 $c/kWh was calculated. This is a 6.7 % difference when compared to the developed model. The possible causes of this difference in result were mentioned.

In an off-grid scenario, the SORC will have to be economically competitive with fossil fuels like diesel generators that are generally being used. In 2015 diesel generator produced electricity amounted to about 20 $c/kWh (Mail & Guardian, 2015) and with the diesel prices that have increased by 57 % (Global Petrol Prices, 2018) since January 2015, the cost of diesel generator produced electricity will amount to 31 $c/kWh in 2018's terms. When looking at the cost per kWh a SORC shows very good potential in becoming a renewable energy source replacement for diesel generators.

The energy demand of Black Mountain mine near Aggeneys is 4.81 MW_e hence a 1 MW_e SORC plant can be used with a modular concept to implement more than one plant in similar off-grid situations. Another option is to use a SORC with larger electrical output and in table 15 it is evident that little compromise on plant efficiency will take place.

Considering the achieved capacity factor, the probable application for a SORC is as part of the total energy solution and not relying solely on the SORC to meet the energy demand. According to the daily operating hours of the SORC, it will not be possible for a single SORC to take over the entire base load production as mines run 24 hours a day. A SORC will be valuable when used in conjunction with other renewable energy sources, like photovoltaic energy, as a SORC can then be used as energy source during night times. The value of a SORC lies in the provided TES and it has proven that a SORC can be economically competitive with traditional fossil fuels in off-grid scenarios.

7.2 Recommendations for future work

A lot of research must still be done to reach an optimized SORC technology. The first recommendation for further work is to extend the theoretical analysis in this thesis for each component. The components were analysed on a high level and it is worth developing detail-designed models to optimize each component like the heat exchangers and turbine with respect to the system. The theoretical analysis can be expanded to include an exergy analysis to determine exactly where the losses occur. A second recommendation in order to better conclude on the economic competitiveness of SORC's, is to develop a more detailed economic model. By doing so a more conclusive economic analysis can be conducted.

Specific SORC plant hardware were chosen for the analysis but the integration of small-scale CSP with an ORC can be done with other combinations of CSP and ORC types. The SORC performance while using another solar collecting technology like a central receiver can then be compared to that of a PT. Variations in ORC cycles includes supercritical cycles, multi pressure level cycles and trilateral cycles that have all been documented by (Macchi & Astolfi, 2017). It is worth investigating whether other combinations of ORC cycles and CSP technology can result in better plant performance.

The final recommendation will be to model SORC's in a hybrid solution with other renewable energy sources like photovoltaic solar energy. The photovoltaic panels can generate electricity cheaper during the day while the SORC can utilise the TES to produce electricity during the night. A hybrid renewable energy solution can then be presented to compete in the off-grid market.

7.3 Conclusion

In attempt to minimise the current trend of global warming, renewable energy sources have to reach the goals set by the IEA. In the small-scale off-grid energy sector, consumers are often left reliant on fossil fuels like diesel generators as the most renewable energy sources offer only intermitted power solutions. The aim of the research was to analyse an ORC integrated with a small-scale CSP system and to determine whether the SORC is a feasible solution to provide electricity for off-

grid applications. The analysis considered a SORC with a gross power output range of 500 kW_e – 5 MW_e for a mining application in the town of Aggeneys in the Northern Cape Province in South Africa.

Each of the objectives set out for the thesis was reached:

- The successful operation of existing small-scale SORC plants has shown that integrating small-scale CSP with ORC is technically feasible. The technology is still considered immature as they are still in the research and development phase and the research interest in SORC's has grown over the past decade.

- Black Mountain mine near the town Aggeneys in the Northern Cape Province in South Africa was selected as site for the case study. Through using a multi criteria decision analysis (MCDA) tool namely the simple multi-attribute rating technique (SMART) the site selection was made. A site specifically in the higher DNI region of South Africa was selected where various small mines exist that consumes less than 5 MW of electricity.

- A theoretical analysis was conducted on the SORC plant by dividing the plant into three functional units namely the solar field, storage and power block. In each functional unit the individual components were considered and theory was developed for each component. By combining the theory of each component, the whole plant was simulated on MatLab to determine the design point of the SORC. The simulation was expanded to an annual simulation to calculate the net annual electricity produced as well as the capacity factors for various combinations of SM's and TES sizes. With the obtained capacity factor of 83 % for 14 hours TES, a SORC cannot solely meet an energy demand.

- A high level economic analysis was conducted and the lowest LCOE was calculated to be 16.7 $c/kWh at a SM of 1.7 and TES size of 6 hours. In comparison with the cost of diesel generator produced electricity of 31 $c/kWh, it shows that a SORC can be economically competitive as power source in off-grid applications.

The conclusion of the thesis is therefore that a SORC is economically competitive with diesel generators in small-scale, off-grid applications. However, a SORC alone cannot meet the energy need and auxiliary energy sources are needed.

Appendices

Appendix A: Fluid Properties

The properties of the various fluids that are used in the thesis are presented in the tables below. N-pentane is shown in table A.1, R134a in table A.2, R245fa in table A.3 and Therminol 66 in table A.4. The isobaric properties by temperature are not included here.

Table A.1: N-pentane properties, (Chemistry Reference, 2017)

Molecular formula	C_5H_{12}
Molecular weight	72.15 g/mol
Chemical family	Paraffin series hydrocarbon
Appearance	Clear, colourless liquid
Physical State	Liquid at ambient temperature
Odour	Sweet petroleum odour
Melting point	-130 °C
Flash point	-40 °C
Boiling point	36 °C
Critical Temperature	197 °C
Auto ignition temperature	260 °C
Critical pressure	3.37 MPa
Density (@ 20 °C)	630 kg/m^3

Table A.2: R134a properties, (Chemistry Reference, 2017)

Molecular formula	CH_2FCF_3
Molecular weight	102.0309 g/mol
Chemical family	Haloalkane refrigerant
Appearance	Colorless
Physical State	Liquefied gas under pressure
Odour	Slight, ether like
Melting point	-103.3 °C
Flash point	Non-flammable
Boiling point	-26.1 °C
Critical Temperature	101.21 °C
Auto ignition temperature	Non-flammable
Critical pressure	4.06 MPa
Density (@ 20 °C)	1209.6 kg/m^3

Table A.3: R24fa properties, (Chemistry Reference, 2017)

Molecular formula	$C_3H_3F_5$
Molecular weight	134.03 g/mol
Chemical family	Hydrofluorocarbon
Appearance	Clear, colourless vapour
Physical State	Liquefied gas under pressure
Odour	Weak
Melting point	-103 °C
Flash point	Non-flammable
Boiling point	15.3 °C
Critical Temperature	134 °C
Auto ignition temperature	Non-flammable
Critical pressure	3.651 MPa
Density (@ 20 °C)	1339 kg/m^3

Table A.4: Therminol 66 properties, (Eastman, 2017)

Appearance	Clear, pale yellow liquid
Composition	Modified terphenyl
Maximum bulk temperature	345 °C
Maximum film temperature	375 °C
Normal boiling point	359 °C
Pumpability, at 300 mm2/s (cSt)	11 °C
Pumpability, at 2000 mm2/s (cSt)	–3 °C
Flash point, COC (ASTM D-92)	184 °C
Flash point, PMCC (ASTM D-93)	170 °C
Autoignition temperature (ASTM E-659)	374 °C
Autoignition temperature (DIN 51794)	399 °C
Pour point (ASTM D-97)	–32 °C
Coefficient of thermal expansion at 200°C	0.000819/°C
Total acidity (ASTM D-664)	< 0.2 mg KOH/g
Average molecular weight	252 g/mol
Pseudocritical temperature	569 °C
Pseudocritical pressure	24.3 bar
Pseudocritical density	317 kg/m3
Chlorine content, ppm (DIN 51577)	< 10 ppm
Copper corrosion (ASTM D-130)	<< 1a
Moisture content, maximum (ASTM E-203)	150 ppm
Dielectric constant @ 23ºC (ASTM D-924)	2.61

Appendix B: Simulation Flowcharts

This chapter shows the simulation flowchart in figure B.1 for the solar field simulation in chapter 5.

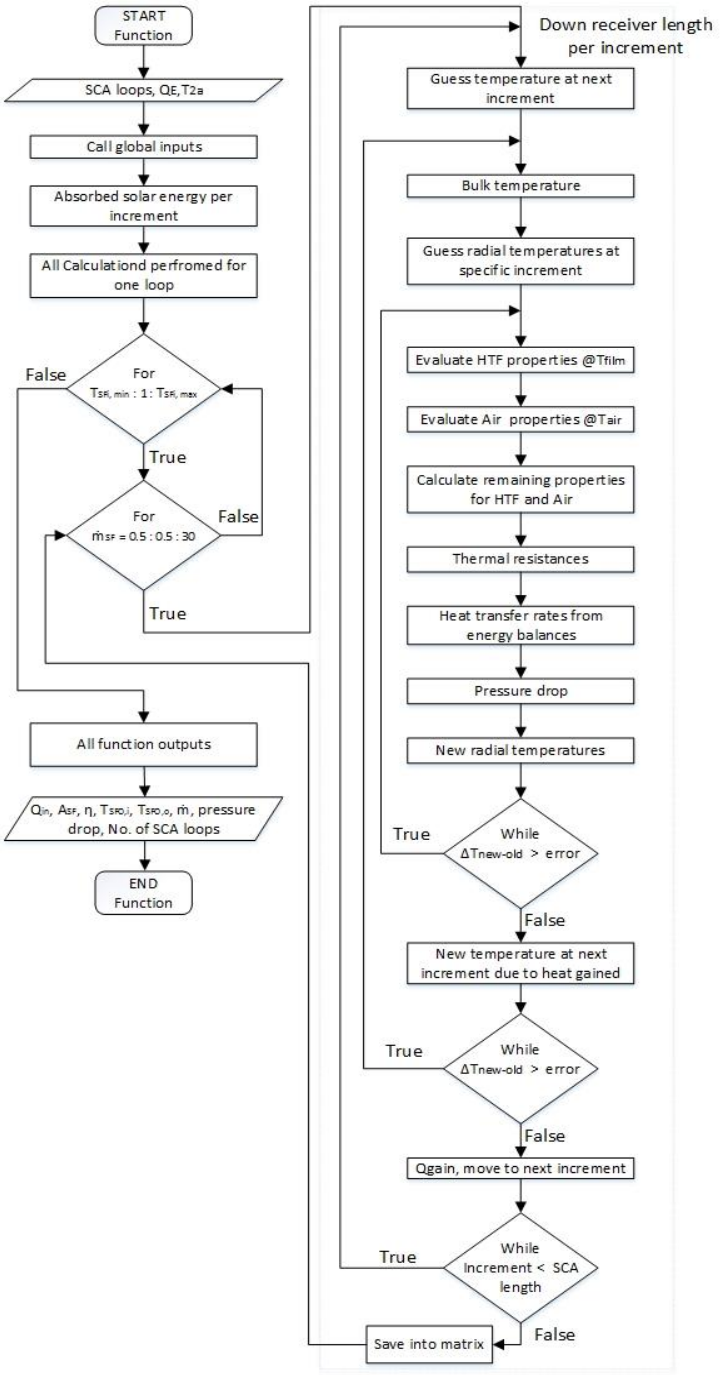

Figure B.1: Solar field simulation flow chart

Appendix C: Design Point Validation

In this chapter the design point simulation is validated by hand calculations done on SMath studio software. The chapter first considered the solar field calculations and thereafter the power block calculations.

C.1 Solar field results validation

In table C.1 the results of the solar field simulation are summarised for a sample calculation shown in section C.2.

Table C.1: Solar field result comparison

Parameter	Design point simulation	Validation Calculation	Parameter	Design point simulation	Validation Calculation
η_c	0.8484	0.8484	h_{htf}	702.8267	701.1307
η_a	0.8230	0.823	$R_{conv.htf}$	0.0036	0.0036
$Q_{sol.a}$	5244.9522	5244.9522	$R_{cond.a}$	6.2432×10^{-4}	6.0×10^{-4}
$Q_{sol.c}$	112.6493	112.6493	h_{an}	1.0729	1.0729
V_{htf}	1.4873	1.4873	$R_{rad.an}$	4.2384	4.2384
Re_{htf}	21295	21294.6	$R_{cond.c}$	0.0054	0.0054
Pr_{htf}	70.1805	69.7053	$h_{rad.ref}$	7.3917	7.3917
f_{htf}	0.0257	0.0257	$R_{rad.ref}$	0.689	0.689
C_{htf}	7.219	7.219	$h_{rad.sky}$	6.4633	6.4633
Nu_{htf}	406.8997	405.9178	$R_{rad.sky}$	0.788	0.788
Re_{air}	34 039	34038.8662	h_{air}	0.0264	0.0264
β_{air}	0.0033	0.0033	$R_{conv.air}$	96.2873	96.2873
Ra_{air}	1.5624×10^{7}	1.5624×10^{7}	Q_1	5229.6	5229.58
Nu_T	48.5362	48.5362	Q_2	15.3665	15.3764
f_{air}	0.9301	0.9301	T_{oa}	385.2127	385.2585
Nu_l	49.4605	49.4605	T_{ia}	381.9478	381.9936
Nu_t	25.7495	25.7495	T_{oc}	320.0001	320.0038
Nu_N	49.4677	49.4677	T_{ic}	320.0833	320.087
Re_i	9715.3	9715.3189	f_{darc}	0.0254	0.0254
Re_{eff}	41579	41578.852	dP_f	408.9441	408.9445
Nu_{air}	124.1675	124.1675	$T_{m,3new}$	362.5846	362.5846

A slight difference is some of the decimal numbers can be seen and is the difference in the cumulative rounding off in the different software used. A sample calculation for the solar field is given next.

C.2 Solar field sample calculation

Simulation input parameters from table 11 - 13

Constraints and constant input parameters

$mdot_{max} := 190 \frac{kg}{s}$ $T_{SF,max} := 618\ K$

$\sigma := 5,67 \cdot 10^{-8} \frac{W}{m^2 K^4}$ $g := 9,81 \frac{m}{s^2}$

Metrological conditions input parameters

$I_{ba} := 884 \frac{W}{m^2}$ $T_a := 305\ K$ $T_{sky} := 273\ K$

$V_{wind} := 4,4 \frac{m}{s}$ $\omega := 44\ deg$

Solar field input parameters

$\eta_{SF,pump} := 0,85$

$dx := 1\ m$ $l_{ap} := 7,51\ m$ $L := 245\ m$

$eps_{surf} := 2 \cdot 10^{-6}\ m$

$D_{ia} := 0,066\ m$ $D_{oa} := 0,07\ m$ $D_{ic} := 0,12\ m$ $D_{oc} := 0,125\ m$

$k_a := 15 \frac{W}{m\ K}$ $eps_a := 0,095$ $\alpha_a := 0,96$

$k_c := 1,2 \frac{W}{m\ K}$ $eps_c := 0,86$ $\alpha_c := 0,02$ $\tau_c := 0,97$

$\rho_{cl} := 0,94$

$e_{sh} := 0,98$ $e_{tr} := 0,994$ $e_{ge} := 1$ $e_{dm} := 0,97$ $e_{da} := 0,995$

$K_{ins} := 1$

Solarfield calculation

Calculate absorbed solar energy per increment

$\eta_c := e_{sh} \cdot e_{tr} \cdot e_{ge} \cdot e_{dm} \cdot e_{da} \cdot e_{un} \cdot \rho_{cl} \cdot K_{ins} = 0,8484$

$\eta_a := \eta_c \cdot \tau_c = 0,823$

$Q_{sol,a} := I_{ba} \cdot l_{ap} \cdot dx \cdot \eta_a \cdot \alpha_a = 5244,9522\ W$

$Q_{sol,c} := I_{ba} \cdot l_{ap} \cdot dx \cdot \eta_c \cdot \alpha_c = 112,6493\ W$

For $T_{SFi} := 362\ K$ and $mdot_{SF} := 4,89\ \frac{kg}{s}$

check mdot_SF < max ***Yes***

Calculate heat gained down length of receiver loop

Guess temperature at next i

$T_{m,1} := T_{SFi}$

$T_{m,3} := T_{SFi} + 2\ K$

Balancing bulk temperature loop

Calculate bulk temp:

$$T_{bulk} := \frac{\left(T_{m,1} + T_{m,3}\right)}{2} = 363\ K$$

Guess radial temperatures

$T_{ia,2} := T_{bulk} + 2\ K$

$T_{oa,2} := T_{bulk} + 7\ K$

$T_{ic,2} := T_{bulk} + 5\ K$

$T_{oc,2} := T_{bulk} + 2\ K$

Calculating heat loss and radial temperatures loop

Evaluate therminol properties @T_film

$$T_{film} := \frac{\left(T_{bulk} + T_{ia,2}\right)}{2} = 364\ K$$

$Cp_{htf} := 1,8060\ \frac{kJ}{kg\ K}$ $\mu_{htf} := 0,0044\ Pa\ s$

$\rho_{htf} := 961\ \frac{kg}{m^3}$ $\nu_{htf} := 4,6098 \cdot 10^{-6}\ \frac{m^2}{s}$

$k_{htf} := 0,114\ \frac{W}{m\ K}$

$$V_{htf} := \frac{mdot_{SF}}{\left(\frac{D_{ia}}{2}\right)^2 \cdot \pi \cdot \rho_{htf}} = 1,4873\ \frac{m}{s}$$

$$Re_{htf} := V_{htf} \cdot \frac{D_{ia}}{\nu_{htf}} = 21294,6041$$

$$Pr_{htf} := \mu_{htf} \cdot \frac{Cp_{htf}}{k_{htf}} = 69,7053$$

Check laminar or turbulent flow? **Turbulent**

$$f_{htf} := \left(0,79 \cdot \ln\left(Re_{htf}\right) - 1,64\right)^{-2} = 0,0257$$

$$C := 2,78 \cdot \ln\left(\frac{\left(\sqrt{\frac{f_{htf}}{8}}\right) \cdot Re_{htf}}{90}\right) = 7,219$$

$$Nu_{htf} := \frac{\left(\sqrt{\frac{f_{htf}}{8}}\right) \cdot Re_{htf} \cdot Pr_{htf}}{12,48 \cdot Pr_{htf}^{\frac{2}{3}} - 7,853 \cdot Pr_{htf}^{\frac{1}{3}} + 3,613 \cdot \ln\left(Pr_{htf}\right) + 5,8 + C} = 405,9178$$

Evaluate air properties @T_a

$$\nu_{air} := 1,6158 \cdot 10^{-5} \frac{m^2}{s} \qquad k_{air} := 2,6624 \cdot 10^{-5} \frac{W}{m\,K}$$

$$Pr_{air} := 0,7058$$

$$Re_{air} := V_{wind} \cdot \frac{D_{oc}}{\nu_{air}} = 34038,8662$$

$$\beta_{air} := \frac{1}{T_a} = 0,0033 \cdot \frac{1}{K}$$

$$Ra_{air} := Pr_{air} \cdot \frac{\left(g \cdot \beta_{air} \cdot \left(T_{oc,2} - T_{sky}\right) \cdot D_{oc}^{3}\right)}{\nu_{air}^{2}} = 1,5624 \cdot 10^{7}$$

$$Nu_T := 0,772 \cdot Ra_{air}^{0,25} = 48,5362$$

$$f_{air} := 1 - \frac{0,13}{Nu_T^{0,16}} = 0,9301$$

$$Nu_l := 2 \cdot \frac{f_{air}}{\ln\left(1 + 2 \cdot \frac{f_{air}}{Nu_T}\right)} = 49,4605$$

$$Nu_t := 0,103 \cdot Ra_{air}^{\frac{1}{3}} = 25,7495$$

$$Nu_N := \left(Nu_l^{10} + Nu_t^{10}\right)^{\frac{1}{10}} = 49,4677$$

From table 8, find a & n

$a := 0,148 \qquad n := 0,633$

$$Re_i := \left(\frac{Nu_N}{a}\right)^{\frac{1}{n}} = 9715,3189$$

$$Re_{eff} := \left(\left(Re_i + Re_{air} \cdot \cos(\omega)\right)^2 + \left(Re_{air} \cdot \sin(\omega)\right)^2\right)^{\frac{1}{2}} = 41578,852$$

$$Nu_{air} := a \cdot Re_{eff}^{\,n} = 124,1675$$

Calculate thermal resistances

$$h_{htf} := Nu_{htf} \cdot \frac{k_{htf}}{D_{ia}} = 701,1307 \ \frac{W}{m^2 K}$$

$$R_{conv,htf} := \frac{1}{\pi \cdot D_{oc} \cdot dx \cdot h_{htf}} = 0,0036 \ \frac{K}{W}$$

$$R_{cond,a} := \frac{\ln\left(\frac{D_{oa}}{D_{ia}}\right)}{2 \cdot \pi \cdot k_a \cdot dx} = 0,0006 \ \frac{K}{W}$$

$$h_{an} := \frac{\sigma \cdot \left(T_{oa,2} + T_{ic,2}\right) \cdot \left(T_{oa,2}^{\,2} + T_{ic,2}^{\,2}\right)}{\frac{1}{eps_a} + \left(\frac{1 - eps_c}{eps_c}\right) \cdot \left(\frac{D_{oa}}{D_{ic}}\right)} = 1,0729 \ \frac{W}{m^2 K}$$

$$R_{rad,an} := \frac{1}{\pi \cdot D_{oa} \cdot dx \cdot h_{an}} = 4,2384 \ \frac{K}{W}$$

$$R_{cond,c} := \frac{\ln\left(\frac{D_{oc}}{D_{ic}}\right)}{2 \cdot \pi \cdot k_c \cdot dx} = 0,0054 \ \frac{K}{W}$$

$$h_{rad,ref} := \sigma \cdot eps_c \cdot \left(T_{oc,2} + T_a\right) \cdot \left(T_{oc,2}^{\,2} + T_a^{\,2}\right) = 7,3917 \ \frac{W}{m^2 \ K}$$

$$R_{rad,ref} := \frac{1}{\pi \cdot \left(\frac{D_{oc}}{2}\right) \cdot dx \cdot h_{rad,ref}} = 0,689 \ \frac{K}{W}$$

$$h_{rad,sky} := \sigma \cdot eps_c \cdot \left(T_{oc,2} + T_{sky}\right) \cdot \left(T_{oc,2}^{\,2} + T_{sky}^{\,2}\right) = 6,4633 \ \frac{W}{m^2 \ K}$$

$$R_{rad,sky} := \frac{1}{\pi \cdot \left(\frac{D_{oc}}{2}\right) \cdot dx \cdot h_{rad,sky}} = 0,788 \ \frac{K}{W}$$

$$h_{air} := Nu_{air} \cdot \frac{k_{air}}{D_{oc}} = 0,0264 \ \frac{W}{m^2 \ K}$$

$$R_{conv,air} := \frac{1}{\pi \cdot D_{oc} \cdot dx \cdot h_{air}} = 96,2873 \ \frac{K}{W}$$

$$R_1 := R_{conv,htf} + R_{cond,a}$$

$$R_2 := R_{rad,an} + R_{cond,c}$$

$$R_3 := \frac{R_{rad,ref} \cdot R_{rad,sky}}{R_{rad,ref} + R_{rad,sky}}$$

$$R_4 := R_{conv,air}$$

Calculate heat transfer rates

$$Q_1 := \frac{T_{oa} - T_{bulk}}{R_1} \quad \ldots\ldots\ldots (1) \qquad Q_2 := \frac{T_{oa} - T_{oc}}{R_2} \quad \ldots\ldots\ldots (2)$$

$$Q_3 := \frac{T_{oc} - T_{sky}}{R_3} \quad \ldots\ldots\ldots (3) \qquad Q_4 := \frac{T_{oc} - T_a}{R_4} \quad \ldots\ldots\ldots (4)$$

substituting 1,2,3 and 4

$$Q_1 := \frac{Q_{sol,a} \cdot R_3 \cdot R_4 + Q_{sol,c} \cdot R_3 \cdot R_4 + T_{sky} \cdot R_4 + T_a \cdot R_3 + \left(Q_{sol,a} \cdot R_2 - T_{bulk}\right) \cdot \left(R_3 + R_4\right)}{\left(\left(R_1 + R_2\right) \cdot \left(R_4 + R_3\right) + R_3 \cdot R_4\right)} =$$

$$= 5229,5758 \ W$$

$$Q_2 := Q_{sol,a} - Q_1 = 15,3764 \ W$$

Temperatures

$T_{oa} := Q_1 \cdot R_1 + T_{bulk} = 385,2585\ K$

$T_{ia} := Q_1 \cdot R_{conv,htf} + T_{bulk} = 381,9936\ K$

$T_{oc} := T_{oa} - Q_2 \cdot R_2 = 320,0038\ K$

$T_{ic} := Q_2 \cdot R_{cond,c} + T_{oc} = 320,087\ K$

Pressure drop

$$f_{darc} := \left(\frac{1}{-1,8 \cdot \log10\left(\frac{6,9}{Re_{htf}} + \left(\frac{\frac{eps_{surf}}{D_{ia}}}{3,7} \right)^{1,11} \right)} \right)^2 = 0,0254$$

$$dP_f := f_{darc} \cdot \frac{dx}{D_{ia}} \cdot 0,5 \cdot \rho_{htf} \cdot V_{htf}^{\ 2} = 408,9445\ Pa$$

Check new temps - old temps < error **No**

Repeat above process until error condition is met

$T_{film} := 371,1875\ K$ (Balanced temperature)

$Q_1 := 5233,2\ W$ (Balanced heat)

End loop

Evaluate therminol properties @T_film

$$Cp_m := 1,8307\ \frac{kJ}{kg\ K}$$

$Q_{gain} := Q_1$

$$T_{m,3new} := T_{m,1} + \frac{Q_{gain}}{mdot_{SF} \cdot Cp_m} = 362,5846\ K$$

Check T_m,3new - T_m,3 < error **No**

Repeat above process until error condition is met

End balancing bulk temperature loop

Read calculated values into matrixes

Repeat process down length of receiver until Q_gain = Q_e

End heat gained down length of reciever loop

C.3 Power block results validation

In table C.2 the results of the power block simulation are summarised for a sample calculation shown in section C.4.

Table C.2: Power block result comparison

Parameter	Design point simulation	Validation Calculation
$\dot{m}_{PB,is}$	10.1234 kg/s	10.1234 kg/s
SP	0.4448	0.4448
Vr	23.468	23.468
η_{turb}	0.8538	0.8556
$\dot{m}_{PB}$	12.351 kg/s	12.3509 kg/s
Q_e	5340.2 kW	5340.1 kW
Q_c	4177.7 kW	4177.7 kW
$Gradient_{SF}$	630.0357	630.0485
y	-260.295	-260.2876
$T_{SFi,min}$	-22.2576	-22.2633
SCA_{loops}	2.0903	2.0902
A_{SF}	7692 m^2	7691.8316 m^2
Q_{in}	6799.7 kW	6799.58 kW
$\dot{m}_{SF}$	19.7775 kg/s	19.777 kg/s
ΔP_{SF}	1118.2 kPa	1118.1343 kPa
$W_{PB,pump}$	81.2932 kW	81.2921 kW
$W_{con,fan}$	20 kW	20kW
$W_{SF,evap}$	2.675 kW	2.6749 kW
W_{SF}	28.4044 kW	28.4031 kW
$W_{SF,total}$	31.0793 kW	31.078 kW
$W_{consumed}$	132.3725 kW	132.3702 kW
W_{net}	867.6275 kW	867.6298 kW
η_{plant}	0.1276	0.1276

In comparing the results of the design point simulation and the calculation on SMath Studio a slight difference is seen in some of the decimal numbers. The reason being the cumulative rounding off difference of the two software packagers used. A sample calculation of the power block is presented next.

C.4 Power block sample calculation

Simulation input parameters from table 11 - 14

Constraints and constant input parameters

$mdot_{max} := 190 \frac{kg}{s}$ $T_{PB,max} := 470\ K$ $T_{SF,max} := 618\ K$

Metrological conditions input parameters

$I_{ba} := 884 \frac{W}{m^2}$ $T_a := 305\ K$

Power block input parameters

$W_{gross} := 1\ MW$ $dP_{SF,evap} := 100\ kPa$

$\eta_{gen} := 0,96$ $dP_{PB,evap} := 100\ kPa$

$\eta_{PB,pump} := 0,75$ $dP_{PB,con} := 1\ kPa$

$\eta_{SF,pump} := 0,85$ $dP_{PB,rec} := 50\ kPa$

Solar field input parameters

$l_{ap} := 7,51\ m$ $L := 245\ m$

Power Block loop $T_{PB1} := T_a + 27\ K = 332\ K$ $T_{PB3} := 461\ K$

Point 1 from saturated liquid tables @T_PB1:

$P_{PB1} := 207,5406\ kPa$ $\rho_{PB1} := 585,8423 \frac{kg}{m^3}$

$h_{PB1} := 55,3467 \frac{kJ}{kg}$ $s_{PB1} := 0,1721 \frac{kJ}{kg\ K}$

Point 3 from saturated vapor tables @T_PB3:

$P_{PB3} := 2,9485\ MPa$ $\rho_{PB3} := 120,8366 \frac{kg}{m^3}$

$h_{PB3} := 563,2091 \frac{kJ}{kg}$ $s_{PB3} := 1,3940 \frac{kJ}{kg\ K}$

Point 2 from Compressed liquid tables @P_PB2:

$P_{PB2} := P_{PB3}$

$s_{PB2} := s_{PB1}$

$T_{PB2} := 333,1402\ K$ $h_{PB2} := 60,0124 \frac{kJ}{kg}$

Point 4 from superheated vapor tables @P_PB4:

$P_{PB4} := P_{PB1}$

$s_{PB4} := s_{PB3}$

$T_{PB4} := 368,1212\ K \qquad h_{PB4} := 464,4279\ \frac{kJ}{kg} \qquad \rho_{PB4} := 5,1490\ \frac{kg}{m^3}$

Point 4a from saturated vapor tables @T_PB1:

$h_{PB4a} := 393,598\ \frac{kJ}{kg} \qquad s_{PB4a} := 1,1909\ \frac{kJ}{kg\ K}$

Point 2a from compressed liquid tables @P_PB2:

$P_{PB2a} := P_{PB3}$

$h_{PB2a} := (h_{PB4} - h_{PB4a}) + h_{PB2} = 130,8423\ \frac{kJ}{kg}$

$T_{PB2a} := 360,9283\ K \qquad s_{PB2a} := 0,3762\ \frac{kJ}{kg\ K}$

Point of evaporation inception from saturated liquid tables @T_PB3:

$s_{PBb} := 1,1464\ \frac{kJ}{kg\ K}$

Calculate turbine efficiency

$mdot_{PB,is} := \frac{\dot{W}_{gross}}{h_{PB3} - h_{PB4}} = 10,1234\ \frac{kg}{s}$

$SP_1 := \frac{mdot_{PB,is}}{\rho_{PB4}} = 1,9661\ \frac{m^3}{s}$

$SP_2 := h_{PB3} - h_{PB4} = 98,7812\ \frac{kJ}{kg}$

$SP := \frac{(1,9661)^{0,5}}{(98,7812)^{0,25}} = 0,4448\ m$

$Vr := \frac{\rho_{PB3}}{\rho_{PB4}} = 23,468$

From figure 30 @SP and Vr:

$\eta_{turb} := 0,8538$

Calculate power block mass flow rate, heat received and heat rejected

$$mdot_{PB} := \frac{mdot_{PB,is}}{\eta_{turb} \cdot \eta_{gen}} = 12,3509 \frac{kg}{s}$$

check mdot_PB < max ***Yes***

$$Q_e := mdot_{PB} \cdot \left(h_{PB3} - h_{PB2a}\right) = 5,3401 \, MW$$

$$Q_c := mdot_{PB} \cdot \left(h_{PB4a} - h_{PB1}\right) = 4,1777 \, MW$$

Possible solar field operating conditions

For $\Delta T_{pinch} := 1 \, K$

determine minimum solar field inlet temperature allowed

$$gradient_{SF} := \frac{T_{SF,max} \cdot \frac{1}{K} - \left(T_{PB3} \cdot \frac{1}{K} + \Delta T_{pinch} \cdot \frac{1}{K}\right)}{\left(s_{PB3} \frac{kg\,K}{kJ} - s_{PBb} \frac{kg\,K}{kJ}\right)} = 630,0485$$

$$y := T_{SF,max} \cdot \frac{1}{K} - gradient_{SF} \cdot s_{PB3} \frac{kg\,K}{kJ} = -260,2876$$

$$T_{SFi,min} := gradient_{SF} \cdot s_{PB2a} \frac{kg\,K}{kJ} + y + 1 = -22,2633$$

Searching from the solar field possible operating conditions input file @ΔT_pinch & T_SFi

For $T_{SFi} := T_{PB2a} + 1 \, K$ (max value between T_SFi,min & T_PB2a + 1)

$mdot_{SF,loop} := 9,4617 \frac{kg}{s}$ $\Delta P_{SF,loop} := 534,934 \, kPa$

$\eta_{SF,therm} := 0,9543$ $Q_{SF,loop} := 2554,8 \, kW$

$\eta_{SF} := 0,7853$ $T_{SFo} := 494,1709 \, K$

$$SCA_{loops} := \frac{Q_e}{Q_{SF,loop}} = 2,0902$$

Solar field totals

$$A_{SF} := l_{ap} \cdot 2 \cdot L \cdot SCA_{loops} = 7691,8316 \, m^2$$

$$Q_{in} := I_{ba} \cdot A_{SF} = 6799,5791 \, kW$$

$$mdot_{SF} := mdot_{SF,loop} \cdot SCA_{loops} = 19,7771 \frac{kg}{s}$$

$$\Delta P_{SF} := \Delta P_{SF,loop} \cdot SCA_{loops} = 1118,1343\ kPa$$

Calculate Pumping requirements

Power block pump

$$W_{PB,pump} := \frac{\frac{mdot_{PB}}{\rho_{PB1}} \cdot \left(\left(P_{PB2} - P_{PB1} \right) + dP_{PB,con} + dP_{PB,rec} + dP_{PB,evap} \right)}{\eta_{PB,pump}} = 81,2921\ kW$$

$$W_{con,fan} := 0,02 \cdot W_{gross} = 20\ kW$$

Solar field pump

Properties from Therminol tables @T_SFo and @T_SF,avg

$$\rho_{SF,o} := 869,8291\ \frac{kg}{m^3} \qquad \rho_{SF,avg} := 915,9504\ \frac{kg}{m^3}$$

$$W_{SF,evap} := \frac{\frac{mdot_{SF}}{\rho_{SF,o}} \cdot dP_{SF,evap}}{\eta_{SF,pump}} = 2,6749\ kW$$

$$W_{SF} := \frac{\frac{mdot_{SF}}{\rho_{SF,avg}} \cdot \Delta P_{SF}}{\eta_{SF,pump}} = 28,4031\ kW$$

$$W_{SF,pump} := W_{SF,evap} + W_{SF} = 31,078\ kW$$

Total power consumed

$$W_{T,pump} := W_{PB,pump} + W_{con,fan} + W_{SF,pump} = 132,3702\ kW$$

Calculate objective function

$$W_N := W_{gross} - W_{T,pump} = 867,6298\ kW$$

$$OBF := \frac{W_N}{Q_{in}} = 0,1276$$

END T_SFi For

END pinch For

Repeat above process for all ΔT_pinch & T_SFi's and from that search for maximum objective function for the specified T_PB3

Appendix D: SAM Simulation

In this chapter the complete set of input parameters used for the SAM validation model is presented in the different categories as distinguished by SAM.

D.2.1 Location and resource

A custom weather file is created to provide data specifically for Black Mountain mine near Aggeneys. The average weather conditions over a period of three years is taken. The SAM location and resource input can be seen in figure D.1.

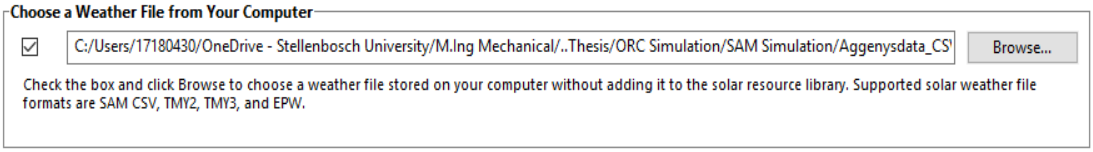

Figure D.1: SAM location and resource input

D.2.2 Solar field

The solar field input parameters are shown in figure D.2.

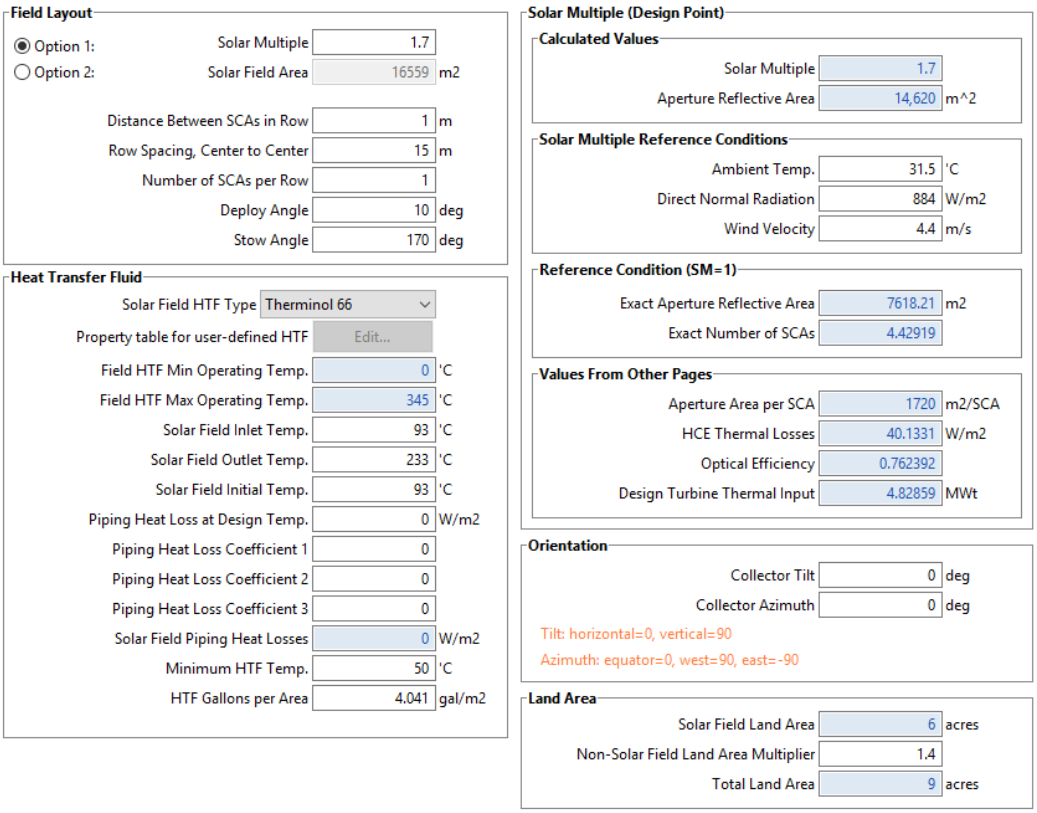

Figure D.2: SAM solar field input parameters

D.2.3 Collectors (SCA's)

The SAM library values for the Ultimate Trough PT collector and the Schott PTR70 receiver are shown in figure D.3 and figure D.4 respectively.

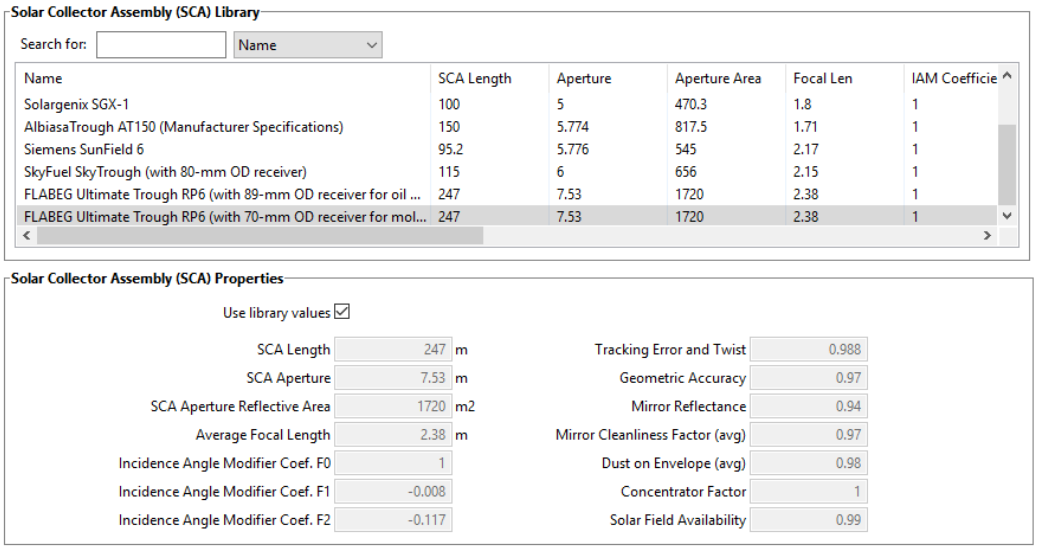

Solar Collector Assembly (SCA) Library

Search for: Name

Name	SCA Length	Aperture	Aperture Area	Focal Len	IAM Coefficie
Solargenix SGX-1	100	5	470.3	1.8	1
AlbiasaTrough AT150 (Manufacturer Specifications)	150	5.774	817.5	1.71	1
Siemens SunField 6	95.2	5.776	545	2.17	1
SkyFuel SkyTrough (with 80-mm OD receiver)	115	6	656	2.15	1
FLABEG Ultimate Trough RP6 (with 89-mm OD receiver for oil ...	247	7.53	1720	2.38	1
FLABEG Ultimate Trough RP6 (with 70-mm OD receiver for mol...	247	7.53	1720	2.38	1

Solar Collector Assembly (SCA) Properties

Use library values ☑

SCA Length	247	m	Tracking Error and Twist	0.988	
SCA Aperture	7.53	m	Geometric Accuracy	0.97	
SCA Aperture Reflective Area	1720	m2	Mirror Reflectance	0.94	
Average Focal Length	2.38	m	Mirror Cleanliness Factor (avg)	0.97	
Incidence Angle Modifier Coef. F0	1		Dust on Envelope (avg)	0.98	
Incidence Angle Modifier Coef. F1	-0.008		Concentrator Factor	1	
Incidence Angle Modifier Coef. F2	-0.117		Solar Field Availability	0.99	

Figure D.3: SAM collector input parameters

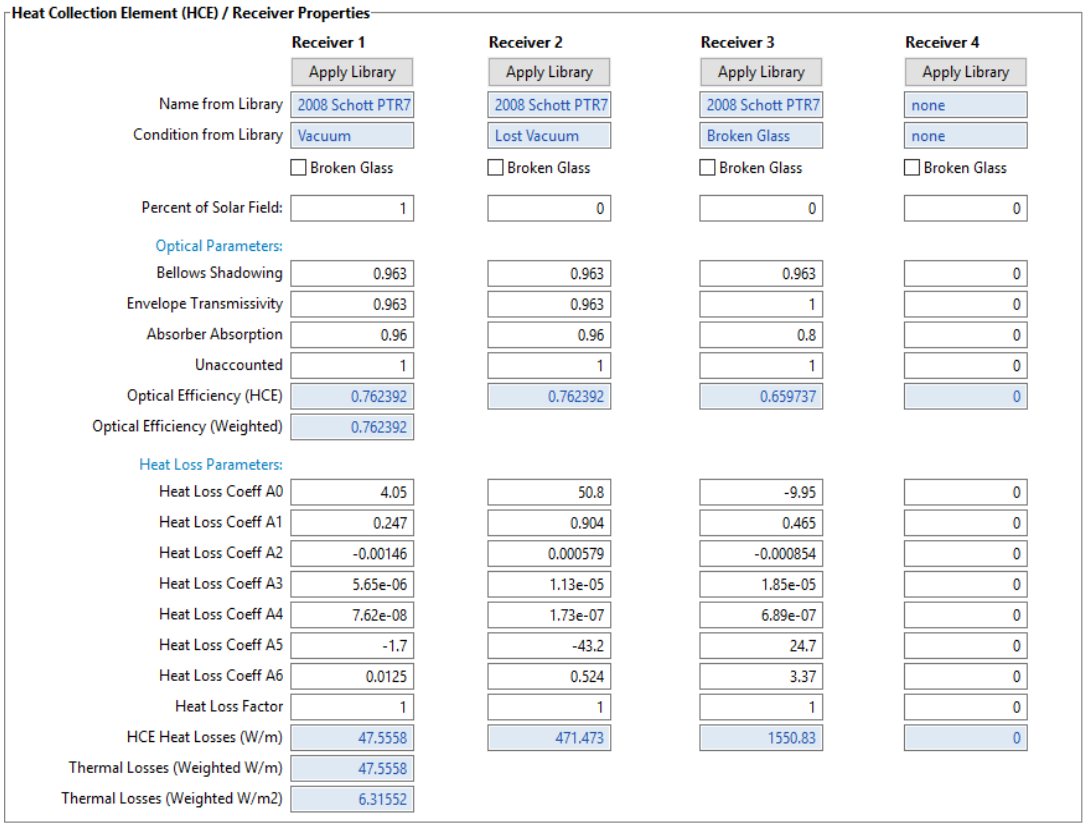

Heat Collection Element (HCE) / Receiver Properties

	Receiver 1	Receiver 2	Receiver 3	Receiver 4
	Apply Library	Apply Library	Apply Library	Apply Library
Name from Library	2008 Schott PTR7	2008 Schott PTR7	2008 Schott PTR7	none
Condition from Library	Vacuum	Lost Vacuum	Broken Glass	none
	☐ Broken Glass	☐ Broken Glass	☐ Broken Glass	☐ Broken Glass
Percent of Solar Field:	1	0	0	0
Optical Parameters:				
Bellows Shadowing	0.963	0.963	0.963	0
Envelope Transmissivity	0.963	0.963	1	0
Absorber Absorption	0.96	0.96	0.8	0
Unaccounted	1	1	1	0
Optical Efficiency (HCE)	0.762392	0.762392	0.659737	0
Optical Efficiency (Weighted)	0.762392			
Heat Loss Parameters:				
Heat Loss Coeff A0	4.05	50.8	-9.95	0
Heat Loss Coeff A1	0.247	0.904	0.465	0
Heat Loss Coeff A2	-0.00146	0.000579	-0.000854	0
Heat Loss Coeff A3	5.65e-06	1.13e-05	1.85e-05	0
Heat Loss Coeff A4	7.62e-08	1.73e-07	6.89e-07	0
Heat Loss Coeff A5	-1.7	-43.2	24.7	0
Heat Loss Coeff A6	0.0125	0.524	3.37	0
Heat Loss Factor	1	1	1	0
HCE Heat Losses (W/m)	47.5558	471.473	1550.83	0
Thermal Losses (Weighted W/m)	47.5558			
Thermal Losses (Weighted W/m2)	6.31552			

Figure D.4: SAM receiver input parameters

D.2.4 Power cycle

The SAM library values for the 1 MW_e ORC turbine are shown in figure D.5. Only a wet cooling option is available in SAM.

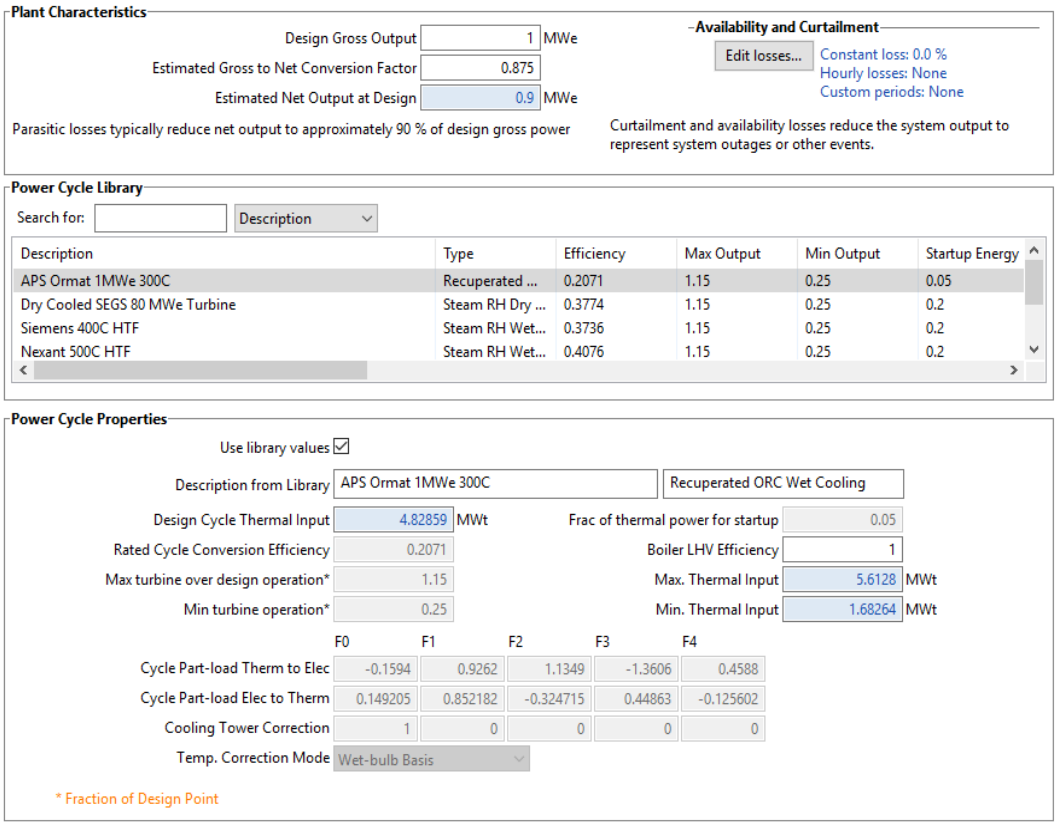

Figure D.5: SAM power block input parameters

D.2.5 Thermal storage

The 6 hour TES input parameters are shown in figure D.6. Only a two-tank TES option is available in SAM and not the desired thermocline. The dispatch schedule of the TES is kept on the SAM default values.

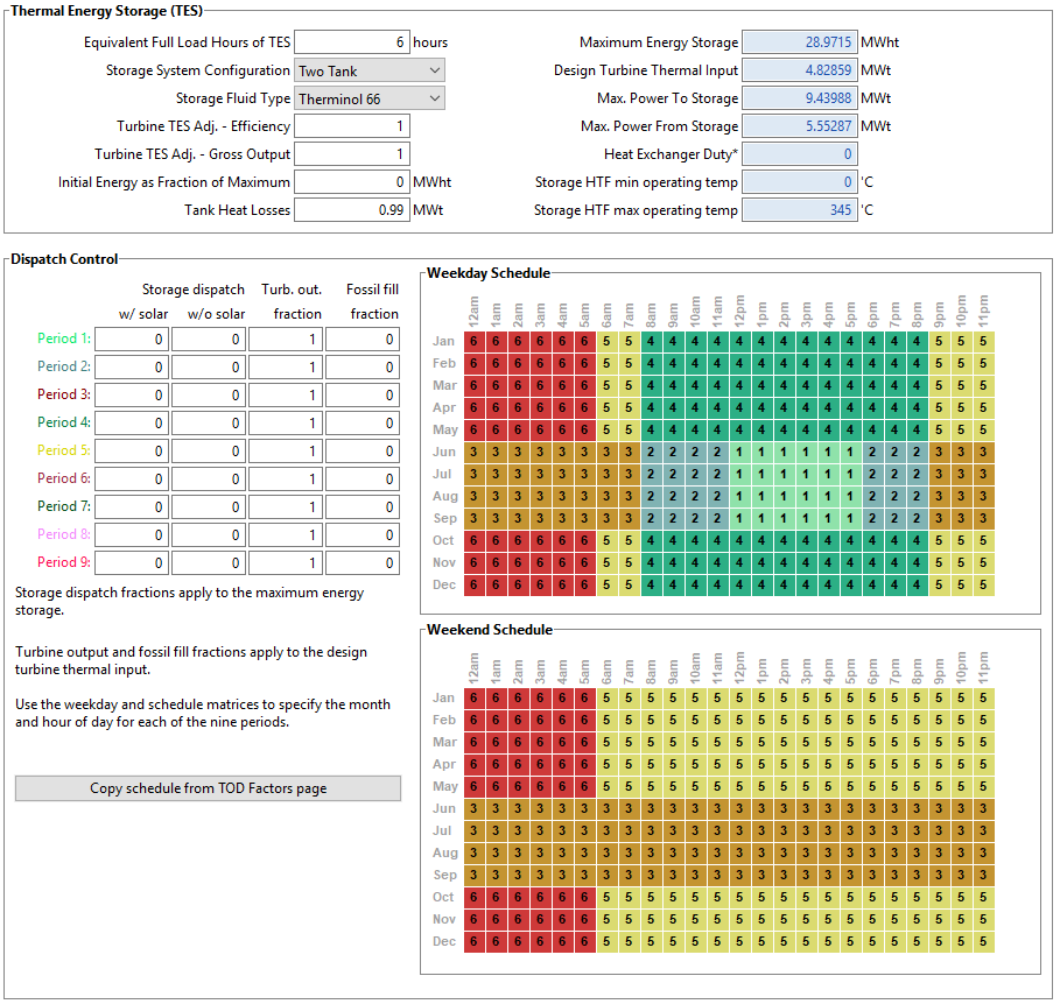

Figure D.6: SAM TES input parameters

D.2.6 Parasitics

The parasitic input parameters are shown in figure D.7. The parasitic input values have been modified to match the model developed in this thesis.

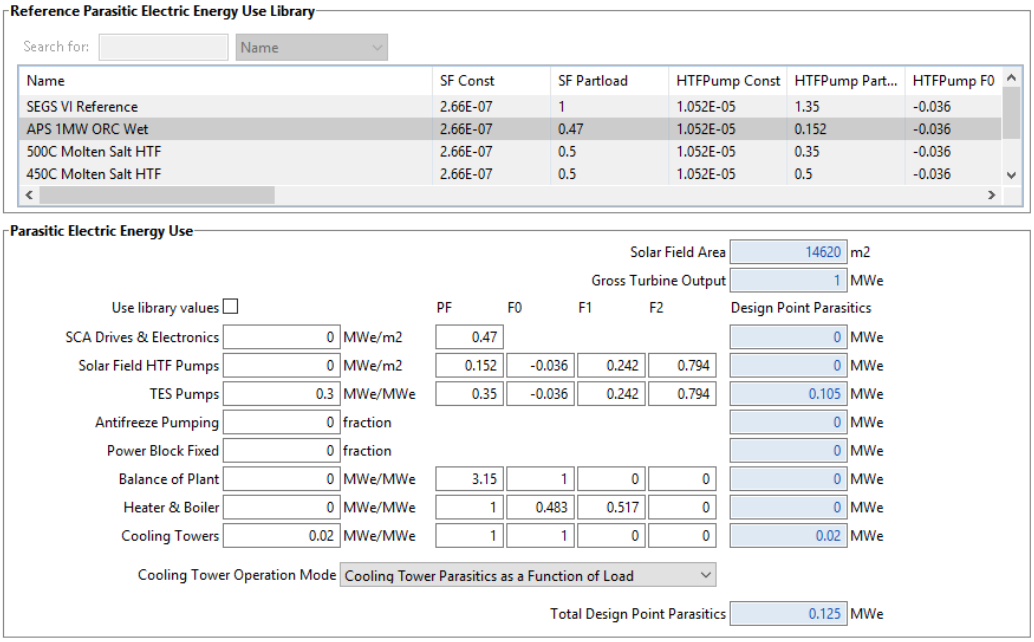

Figure D.7: SAM parasitic input parameters

D.2.7 Financial parameters

The financial input parameters are shown in figure D.8.

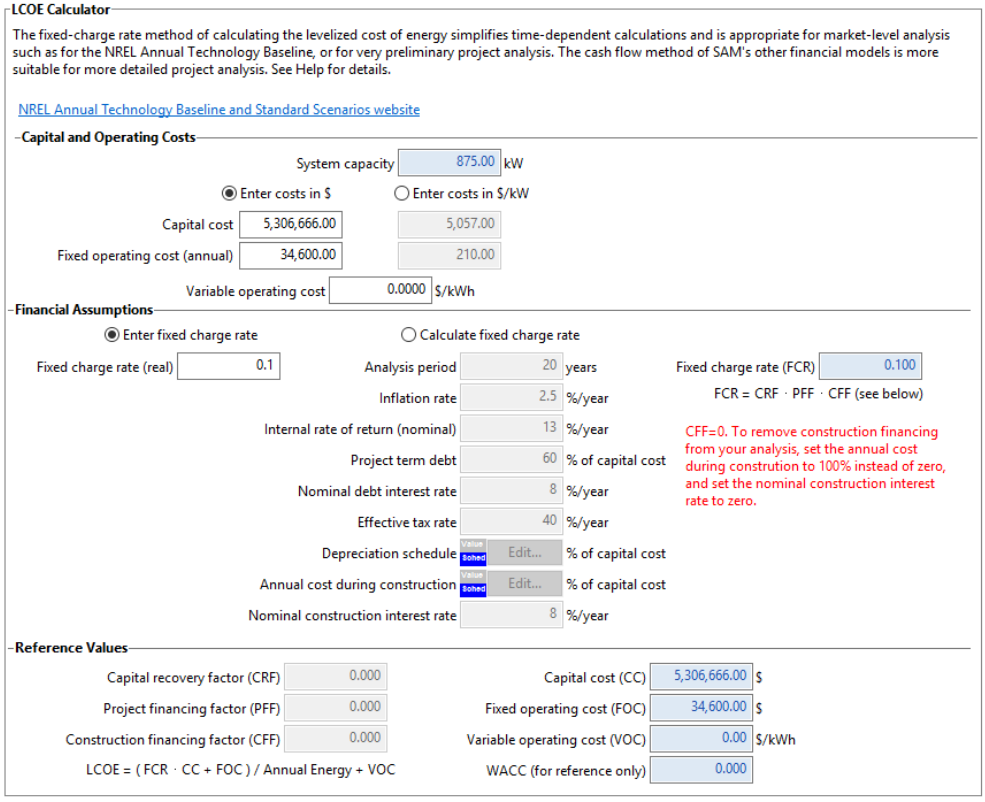

Figure D.8: SAM financial input parameters

References

Airlight Energy, 2015. Ait-Baha CSP pilot plant - Airlight Energy. Available at: http://www.airlightenergy.com/ait-baha-csp-pilot-plant/ [Accessed November 14, 2016].

Andreasen, J.G., Meroni, A. & Haglind, F., 2017. A comparison of organic and steam Rankine cycle power systems for waste heat recovery on large ships. *Energies*, 10(4), pp.1–23.

Badr, O., Probert, S.D. & O'Callaghan, P.W., 1985. Selecting a working fluid for a Rankine-cycle engine. *Applied Energy*, 21(1), pp.1–42.

Bao, J. & Zhao, L., 2013. A review of working fluid and expander selections for organic Rankine cycle. *Renewable and Sustainable Energy Reviews*, 24, pp.325–342. Available at: http://dx.doi.org/10.1016/j.rser.2013.03.040.

Berlin, H.Z., 2014. *Granite Power - Public Dissemination Report*,

Binsley, R.L. & Binsley, R.L., 1968. Axial Turbine Performance Evaluation. Part A—Loss-Geometry Relationships. *Journal of Engineering for Gas Turbines and Power*, 90(4), p.341. Available at: http://gasturbinespower.asmedigitalcollection.asme.org/article.aspx?doi=10.1115/1.3609211 [Accessed March 24, 2017].

C2ES, 2015. UN Framework Convention on Climate Change (UNFCCC). *Outcomes of the UN Climate Change Conference in Paris*, (December), pp.1–5. Available at: http://www.c2es.org/international/negotiations/cop21-paris/summary.

Cabrera, F.J. et al., 2013. Use of parabolic trough solar collectors for solar refrigeration and air-conditioning applications. *Renewable and Sustainable Energy Reviews*, 20, pp.103–118.

Canada, S. et al., 2005. Status of APS 1-Mwe Parabolic Trough Project. , p.Size: 5 pp. Available at: www.osti.gov/servlets/purl/882807-d8b9mN/.

Casati, E.I.M., 2014. *New Concepts for Organic Rankine Cycle Power Systems*. Delft University of Technology.

Çengel, Y.A. & Boles, M.A., 2011. *Thermodynamics : an engineering approach*, McGraw-Hill.

Çengel, Y.A. & Cimbala, J.M., 2010. *Fluid mechanics : fundamentals and applications*, McGraw-Hill Higher Education. Available at: https://books.google.co.za/books?id=zdQRQgAACAAJ&dq=cengel+cimbala+fluid+mechanics&hl=en&sa=X&ved=0ahUKEwifrOfq8vjSAhWrKMAKHdlOAt0Q6AEINDAF [Accessed March 28, 2017].

Çengel, Y.A. & Ghajar, A.J. (Afshin J., 2015. *Heat and mass transfer : fundamentals & applications*, McGraw-Hill.

Chemistry Reference, 2017. Chemistry Reference. , p.PENTANE*-(109-66-0). Available at: http://chemistry-reference.com/q_compounds.asp?CAS=109-66-0 [Accessed September 7, 2017].

Chen, H., Goswami, D.Y. & Stefanakos, E.K., 2010. A review of thermodynamic cycles and working fluids for the conversion of low-grade heat. *Renewable and Sustainable Energy Reviews*, 14(9), pp.3059–3067. Available at: http://linkinghub.elsevier.com/retrieve/pii/S1364032110001863 [Accessed September 4, 2017].

Craig, O.O. et al., 2017. The Current and Future Energy Economics of Concentrating Solar Power (Csp) in South Africa. *South African Journal of Industrial Engineering*, 28(November), pp.1–14.

Craig, T.O., Brent, A.C. & Dinter, F., 2017. Concentrated Solar Power (Csp) Innovation Analysis in South Africa. *South African Journal of Industrial Engineering*, 28(2), pp.14–27. Available at: http://sajie.journals.ac.za/pub/article/view/1640.

Curran, H.M., 1981. Use of Organic Working Fluids in Rankine Engines. *Journal of Energy*, 5, pp.218–223.

Delgado-Torres, A.M. & García-Rodríguez, L., 2010. Analysis and optimization of the low-temperature solar organic Rankine cycle (ORC). *Energy Conversion and Management*, 51(12), pp.2846–2856.

Desai, N.B. & Bandyopadhyay, S., 2016. Thermo-economic comparisons between solar steam Rankine and organic Rankine cycles. *Applied Thermal Engineering*, 105, pp.862–875. Available at: http://dx.doi.org/10.1016/j.applthermaleng.2016.04.055.

Dickes, R. et al., 2015. Impact of Model Reduction on the Dynamic Simulation of a Micro-Scale Concentrated Solar Power System Integrated with a Thermal Storage. *Proceedings of the ISES Solar World Congress 2015*, (November), pp.1–11. Available at: http://orbi.ulg.ac.be/handle/2268/188674%0Ahttp://proceedings.ises.org/citation?doi=swc.2015.04.15.

Dickes, R., 2016. Solar-based ORC power systems. In *ORC-Plus Workshop*.

Dinter, F. & Busse, K.T., 2015. Overview of predictive CSP spread scenarios and its opportunities. *Sasec 2015*, 27(May), pp.1–7.

Dudley, V.E. et al., 1994. Test results: SEGS LS-2 solar collector.

Duffie, J.A. & Beckman, W.A., 2013. *Solar engineering of thermal processes*, Wiley.

Eastman, 2017. *THERMINOL® 66 heat transfer fluid*,

Eskom, 2014. Transmission development plan. Available at: http://www.eskom.co.za/Whatweredoing/ElectricityGeneration/PowerStations/Pages/Map_Of_Eskom_Power_Stations.aspx [Accessed February 28, 2017].

Evans, G.W., 2017. *Multiple criteria decision analysis for industrial engineering : methodology and applications*, Available at: https://books.google.co.za/books?id=zqaiDQAAQBAJ&dq=Von+Winterfeldt+%26+Edwards.+(1986).+SMART+DECISIONS+SUMMARY&source=gbs_navlinks_s [Accessed January 11, 2018].

Gaggioli, W., 2016a. Index ORC-PLUS Project • Background • ORC-PLUS Project • Project goals • Expected results. In *ORC-Plus Workshop 1*. pp. 1–25.

Gaggioli, W., 2016b. ORC-PLUS (Organic Rankine Cycle - Prototype Link to Storage Unit) PROJECT. In *SolarPaces*. p. 657690.

García-Valladares, O. & Velázquez, N., 2009. Numerical simulation of parabolic trough solar collector: Improvement using counter flow concentric circular heat exchangers. *International Journal of Heat and Mass Transfer*, 52(3–4), pp.597–609. Available at: http://dx.doi.org/10.1016/j.ijheatmasstransfer.2008.08.004.

GeoSun Africa, 2016. Solar Maps | GeoSun Africa. Available at: http://geosun.co.za/solar-maps/ [Accessed November 18, 2016].

Giostri, A. et al., 2012. Comparison of Two Linear Collectors in Solar Thermal Plants: Parabolic Trough Versus Fresnel. *Journal of Solar Energy Engineering*, 135(1), p.011001. Available at: http://solarenergyengineering.asmedigitalcollection.asme.org/article.aspx?doi=10.1115/1.4006792.

Giovannelli, A., 2015. State of the art on small-scale concentrated solar power plants. *Energy Procedia*, 82, pp.607–614.

Global Petrol Prices, 2018. South Africa diesel prices, 27-Aug-2018 | GlobalPetrolPrices.com. Available at: https://www.globalpetrolprices.com/South-Africa/diesel_prices/ [Accessed September 2, 2018].

Good, P. et al., 2016. A 1.2MWth solar parabolic trough system based on air as heat transfer fluid at 500°C — Engineering design, modelling, construction, and testing. *Solar Energy*, 139, pp.398–411. Available at: http://linkinghub.elsevier.com/retrieve/pii/S0038092X16304583.

Good, P. et al., 2013. Towards a commercial parabolic trough CSP system using air as heat transfer fluid. *Energy Procedia*, 49, pp.381–385. Available at: http://dx.doi.org/10.1016/j.egypro.2014.03.041.

Günter, R. & Colin, A., 2016. A literature review on the potential of renewable electricity sources for mining operations in South Africa. *Journal of Energy in Southern Africa*, 27(2), pp.1–21.

Günther, M., Joemann, M. & Csambor, S., 2011. Advanced CSP Teaching Materials Parabolic Trough Technology Authors. *2011*, pp.1–43.

Guo, C. et al., 2014. Performance analysis of organic Rankine cycle based on location of heat transfer pinch point in evaporator. *Applied Thermal Engineering*, 62(1), pp.176–186. Available at: http://dx.doi.org/10.1016/j.applthermaleng.2013.09.036.

Helios CSP, 2018. Concentrated Solar Power Installed Capacity Increased to 5133 MW by the End of 2017 – HELIOSCSP. Available at: http://helioscsp.com/concentrated-solar-power-installed-capacity-increased-to-5133-mw-by-the-end-of-2017/ [Accessed August 24, 2018].

IEA, 2014. *Technology Roadmap Solar Thermal Electricity*, Available at: www.iea.org.

IEA & IRENA, 2017. Perspectives for the Energy Transition: Investment Needs for a Low-Carbon Energy System. *International Energy Agency*, p.204. Available at: http://www.irena.org/DocumentDownloads/Publications/Perspectives_for_the_Energy_Transition_2017.pdf.

IRESEN, 2016a. IRESEN - Research Institute for Solar Energy and New Energies. Available at: http://www.iresen.org/en/ORC-PLUS.html [Accessed November 15, 2016].

IRESEN, 2016b. Research Institute for Solar Energy and New Energies. In *ORC-Plus Workshop 1*. CASABLANCA.

Jamal, N., 2015. Options for the supply of electricity to rural homes in South Africa. *Journal of Energy in Southern Africa*, 26(3), pp.58–65. Available at: http://www.scielo.org.za/scielo.php?script=sci_arttext&pid=S1021-447X2015000300006&nrm=iso.

Kalaiselvam, S. & Parameshwaran, R., *Thermal energy storage technologies for sustainability : systems design, assessment, and applications*,

Kalogirou, S.A., 2012. A detailed thermal model of a parabolic trough collector receiver. *Energy*, 48(1), pp.298–306. Available at: http://dx.doi.org/10.1016/j.energy.2012.06.023.

Keighley, P.S., 2013. 96-Year-Old Solar Energy Genius Harry Zvi Tabor Talks To NoCamels About Pioneering Solar Power | People. Available at: http://nocamels.com/2013/08/96-year-old-solar-energy-genius-harry-zvi-tabor-talks-to-nocamels-about-pioneering-solar-power/ [Accessed August 26, 2018].

Kim, K. & Han, C., 2015. A Review on Solar Collector and Solar Organic Rankine Cycle (ORC) Systems. *Journal of Automation and Control Engineering Vol*, 3(1), pp.66–73. Available at: http://www.joace.org/uploadfile/2014/0310/20140310042620325.pdf.

Larjola, J., 1995. Electricity from industrial waste heat using high-speed organic Rankine cycle (ORC). *International Journal of Production Economics*, 41(1–3), pp.227–235. Available at: http://linkinghub.elsevier.com/retrieve/pii/0925527394000980 [Accessed September 4, 2017].

Li, G., 2016. Organic Rankine cycle performance evaluation and thermoeconomic assessment with various applications part I: Energy and exergy performance evaluation. *Renewable and Sustainable Energy Reviews*, 53, pp.477–499. Available at: http://dx.doi.org/10.1016/j.rser.2015.08.066.

Lovegrove, K. & Stein, W., 2012. *Concentrating solar power technology : principles, developments and applications*, Woodhead Publishing.

Lovins, A.B., 2011. *Reinventing fire : bold business solutions for the new energy era*, Chelsea Green Pub. Available at: https://books.google.co.za/books?id=ZQVZxsGFjnAC&printsec=frontcover&source=gbs_ge_summary_r&cad=0#v=onepage&q=microgrids&f=false [Accessed November 28, 2016].

Ma, Z. et al., 2012. Thermal Energy Storage Performance Metrics and Use in Thermal Energy Storage Design. *Solar 2012*, p.6. Available at: https://ases.conference-services.net/resources/252/2859/pdf/SOLAR2012_0086_full paper.pdf.

Macchi, E. & Astolfi, M., 2017. *Organic rankine cycle (ORC) power systems : technologies and applications*, Available at: https://books.google.co.za/books/about/Organic_Rankine_Cycle_ORC_Power_Systems.html?id=BoW9jwEACAAJ&redir_esc=y&hl=en [Accessed March 6, 2017].

Macchi, E. & Perdichizzi, A., 1977. Theoretical Prediction of the Off-Design Performance of Axial-Flow Turbines, sl. Available at: https://scholar.google.com/scholar?cluster=8182386686576960997&hl=en&oi=scholarr [Accessed March 24, 2017].

Madaly, K., 2014. Identifying the optimum storage capacity for a 100-MWe concentrating solar power plant in South Africa. , (April).

Madhawa Hettiarachchi, H.D. et al., 2007. Optimum design criteria for an Organic Rankine cycle using low-temperature geothermal heat sources. *Energy*, 32(9), pp.1698–1706.

Mago, P.J. et al., 2008. An examination of regenerative organic Rankine cycles using dry fluids. *Applied Thermal Engineering*, 28(8–9), pp.998–1007. Available at: http://linkinghub.elsevier.com/retrieve/pii/S1359431107002293 [Accessed September 4, 2017].

Mail & Guardian, 2015. 21 days and Eskom's broke | News | National | M&G. Available at: https://mg.co.za/article/2015-01-08-21-days-and-eskoms-broke [Accessed September 2, 2018].

Maizza, V. & Maizza, A., 2001. Unconventional working fluids in organic Rankine-cycles for waste energy recovery systems. *Applied Thermal Engineering*, 21(3), pp.381–390. Available at: http://linkinghub.elsevier.com/retrieve/pii/S1359431100000442 [Accessed September 4, 2017].

Maizza, V. & Maizza, A., 1996. Working fluids in non-steady flows for waste energy recovery systems. *Applied Thermal Engineering*, 16(7), pp.579–590. Available at: http://linkinghub.elsevier.com/retrieve/pii/1359431195000445 [Accessed September 4, 2017].

Mechinox Heat Exchangers, 2018. Gasketed Plate & Frame Heat Exchangers Suppliers South Africa. Available at: http://www.heat-exchangers.co.za/products/gasketed-plate-heat-exchangers/ [Accessed May 25, 2018].

Mehos, M., Turchi, C. & Jorgenson, J., 2016. Advancing Concentrating Solar Power Technology, Performance, and Dispatchability. *SunShot*, (May), pp.1–66. Available at: http://www.nrel.gov/docs/fy16osti/65688.pdf.

Mitchell, J. & Scheuerer, M., 2014. Applications For Concentrating Solar Power (CSP) 01.09.2014. Available at: ProTarget.

Morgan, V.T., 1975. The Overall Convective Heat Transfer from Smooth Circular Cylinders. *Advances in Heat Transfer*, 11, pp.199–264.

Naeeni, N. & Yaghoubi, M., 2007. Analysis of wind flow around a parabolic collector (2) heat transfer from receiver tube. *Renewable Energy*, 32(8), pp.1259–1272.

National Refrigerants Inc., 2015. *pentane MSDS*, Available at: http://www.refrigerants.com/pdf/SDS Pentane.pdf.

Nelson, V. & Starcher, K., 2011. *Introduction To Renewable Energy*,

NIST, 2017. NIST Chemistry WebBook. *National Institute of Standards and Technology*. Available at: http://webbook.nist.gov/chemistry/ [Accessed October 12, 2017].

NREL, 2014. Concentrating Solar Power Projects - Ivanpah Solar Electric Generating System | Concentrating Solar Power | NREL. Available at: https://www.nrel.gov/csp/solarpaces/project_detail.cfm/projectID=62 [Accessed August 26, 2018].

O'Donovan, A., 2013. MACCSol Project: Performance Characteristics of a Novel Modular Air-Cooled Condenser.

O'Donovan, A. & Grimes, R., 2015. Pressure drop analysis of steam condensation in air-cooled circular tube bundles. *Applied Thermal Engineering*, 87, pp.106–116. Available at: http://dx.doi.org/10.1016/j.applthermaleng.2015.04.072.

Ojan, M., 2015. Solar Power and new concrete applications : a pilot plant in Morocco.

ORC Plus, 2015. ORC-PLUS - Dispatchable small-scale solar thermal electricity. Available at: http://www.orc-plus.eu/ [Accessed November 15, 2016].

Orosz, M.S., 2009. Small scale solar orc system for distributed power in Lesotho. *29th ISES Biennial Solar World Congress 2009, ISES 2009*, 2(3), pp.1042–1048. Available at: http://www.scopus.com/inward/record.url?eid=2-s2.0-84873835908&partnerID=tZOtx3y1.

Padilla, R.V. et al., 2011. Heat transfer analysis of parabolic trough solar receiver. *Applied Energy*, 88(12), pp.5097–5110. Available at: http://dx.doi.org/10.1016/j.apenergy.2011.07.012.

Papadopoulos, A.I., Stijepovic, M. & Linke, P., 2010. On the systematic design and selection of optimal working fluids for Organic Rankine Cycles. *Applied Thermal Engineering*, 30(6–7), pp.760–769. Available at: http://linkinghub.elsevier.com/retrieve/pii/S1359431109003536 [Accessed September 4, 2017].

Pikra, G. et al., 2013. Development of small scale concentrated solar power plant using organic Rankine cycle for isolated region in Indonesia. *Energy Procedia*, 32, pp.122–128. Available at: http://dx.doi.org/10.1016/j.egypro.2013.05.016.

PowerTechnology, Holaniku at Keahole Point Micro CSP Thermal Plant - Power Technology. Available at: http://www.power-technology.com/projects/holanikuatkeaholepoi/ [Accessed November 14, 2016].

Pretorius, J.P. & Du Preez, A.F., 2009. Eskom cooling technologies Eskom power stations. In *Eskom cooling technologies 14th IAHR Conference Stellenbosch*,.

Price, H. et al., 2002. Advances in Parabolic Trough Solar Power Technology. *Journal of Solar Energy Engineering*, 124(2), p.109.

Quoilin, S. et al., 2015. Design, Modeling, and Performance Optimization of a Reversible Heat Pump/Organic Rankine Cycle System for Domestic Application. *Journal of Engineering for Gas Turbines and Power*, 138(1), p.011701. Available at: http://gasturbinespower.asmedigitalcollection.asme.org/article.aspx?doi=10.1115/1.4031004.

Quoilin, S. et al., 2011. Performance and design optimization of a low-cost solar organic Rankine cycle for remote power generation. *Solar Energy*, 85(5), pp.955–966. Available at: http://dx.doi.org/10.1016/j.solener.2011.02.010.

Quoilin, S., 2011. *Sustainable energy conversion through the use of Organic Rankine Cycles for waste heat recovery and solar applications*. University of Liege. Available at: http://orbi.ulg.ac.be/handle/2268/96436.

Quoilin, S. et al., 2013. Techno-economic survey of organic rankine cycle (ORC) systems. *Renewable and Sustainable Energy Reviews*, 22, pp.168–186.

Quoilin, S. & Lemort, V., 2009. Technological and Economical Survey of Organic Rankine Cycle Systems. *5th European Conference Economics and Management of Energy in Industry*, 278(36), p.12. Available at: http://orbi.ulg.ac.be/handle/2268/14609.

Quoilin, S. & Lemort, V., 2011. *The Organic Rankine Cycle: Thermodynamics, Applications and Optimization*, Paris, France: Eolss.

Raush, J.R. et al., 2013. Demonstration of Pilot Scale Large Aperture Parabolic Trough Organic Rankine Cycle Solar Thermal Power Plant in Louisiana. *Journal of Power and Energy Engineering*, 2013(December), pp.29–39. Available at: http://www.scirp.org/journal/PaperInformation.aspx?PaperID=40211#.VMhfCf54oUq.

Riffelmann, K. et al., 2014. Ultimate Trough® - A significant step towards cost-competitive CSP. *Energy Procedia*, 49, pp.1831–1839. Available at: http://dx.doi.org/10.1016/j.egypro.2014.03.194.

Ruegamer, T. et al., 2013. Molten salt for parabolic trough applications: System simulation and scale effects. *Energy Procedia*, 49(December), pp.1523–1532. Available at: http://dx.doi.org/10.1016/j.egypro.2014.03.161.

Russell, F., 2003. 27--Heat Transfer Analysis and Modeling of a Parabolic Trough Solar Receiver Implemented in Engineering Equation Solver. *National Renewable Energy Laboratory*, (October), p.164.

Rycroft, M., 2018. Power from the sun: An overview of CSP in South Africa - EE Publishers. *EE Publishers*. Available at: http://www.ee.co.za/article/power-from-the-sun-an-overview-of-csp-in-south-africa.html [Accessed August 28, 2018].

Saini, A. et al., 2015. Thermo-economic analysis of a mixture of RC-318 and pentane as a working fluid in a high temperature ORC. *Proceedings of the 3rd International Seminar on ORC Power Systems*, (2011), p.Paper ID: 155. Available at: www.asme-orc2015.be/online/proceedings/documents/155.pdf.

Saleh, B. et al., 2007. Working fluids for low-temperature organic Rankine cycles. *Energy*, 32(7), pp.1210–1221. Available at: http://linkinghub.elsevier.com/retrieve/pii/S0360544206001812 [Accessed September 4, 2017].

System Advisor Model Version 2017.9.5 (SAM 2017.9.5). National Renewable Energy Laboratory. Golden, CO. Accessed August 1, 2018. Available at: https://sam.nrel.gov/content/downloads.

Sandall, O.C., Hanna, O.T. & Mazet, P.R., 1980. A new theoretical formula for turbulent heat and mass transfer with gases or liquids in tube flow. *The Canadian Journal of Chemical Engineering*, 58(4), pp.443–447. Available at: http://doi.wiley.com/10.1002/cjce.5450580404 [Accessed February 28, 2017].

SCHOTT Solar CSP GmbH, 2013. SCHOTT PTR®70 Receivers, Dataheet. , p.2. Available at: http://www.schott.com/csp/english/download/schott_ptr70_4th_generation_datasheet.pdf.

SEIFSA, 2016. High electricity price increase will have a crippling effect of the already embattled metals and engineering sector.

Senechal, S., 2014. Turboden ORC : Recent developments and new applications in organic rankine cycle technology Business Energy Efficiency Seminar Theatre. , (May).

Shah, R.K. (Ramesh K.. & Sekulić, D.P., 2003. *Fundamentals of heat exchanger design*, John Wiley & Sons. Available at: https://books.google.co.za/books?id=beSXNAZblWQC&dq=shah+and+sekulic&source=gbs_navlinks_s [Accessed October 12, 2017].

Shuman, F., 1907. The Direct Acting Solar Engine: the Prime Mover of the Immediate Future.

Sklar-Chik, M.D. & Brent, A.C., 2017. *System Cost of Energy Generation Scenarios for South Africa: Understanding the real cost of integrating energy generation technologies*.

Smith, S.F., 1965. A Simple Correlation of Turbine Efficiency. *Journal of the Royal Aeronautical Society*, 69(655), pp.467–470. Available at: https://www.cambridge.org/core/product/identifier/S0001924000059108/type/journal_article [Accessed March 24, 2017].

SODA, 2014. Solar Energy Services for Professionals. *2014*. Available at: http://www.soda-pro.com/web-services/radiation/helioclim-3-archives-for-free [Accessed May 27, 2018].

SolarServer, 2010. ElectraTherm technology improves efficiency of solar thermal power plant on Hawaii. Available at: http://www.solarserver.com/news/news-e-1493.html [Accessed November 14, 2016].

SOPOGY, 2013. Sopogy MicroCSP - Solar Thermal, simplified - PROJECTS. Available at: http://sopogy.org/projects/index.php?id=39 [Accessed November 14, 2016].

Southon, M., 2015. *Performance and cost evaluation to inform the design and implementation of Organic Rankine Cycles in New Zealand (Master Thesis)*. University of Canterbury.

Stine, W.B. & Geyer, M., 2001. *Power From The Sun*, Available at: http://www.powerfromthesun.net/book.html.

Tabor, H.Z. & Doron, B., 1990. The Beith Ha'Arava 5 MW(e) Solar Pond Power Plant (SPPP)-Progress report. *Solar Energy*, 45(4), pp.247–253.

Tartière, T. & Astolfi, M., 2017. A World Overview of the Organic Rankine Cycle Market. *Energy Procedia*, 129, pp.2–9. Available at: http://dx.doi.org/10.1016/j.egypro.2017.09.159.

Tchanche, B.F. et al., 2011. Low-grade heat conversion into power using organic Rankine cycles - A review of various applications. *Renewable and Sustainable Energy Reviews*, 15(8), pp.3963–3979. Available at: http://dx.doi.org/10.1016/j.rser.2011.07.024.

Thyssenkrupp, 2017. *thyssenkrupp Materials (UK) Ltd Processing / Welding Standard welding processes for this steel grade are :*,

Touloukian, Y.S. & Dewitt, D.P., 1972. *Thermal radiative properties: Nonmetallic solids.*, United States.

Vélez, F. et al., 2012. A technical, economical and market review of organic Rankine cycles for the conversion of low-grade heat for power generation. *Renewable and Sustainable Energy Reviews*, 16(6), pp.4175–4189. Available at: http://dx.doi.org/10.1016/j.rser.2012.03.022.

Wang, D., Ling, X. & Peng, H., 2012. Performance analysis of double organic Rankine cycle for discontinuous low temperature waste heat recovery. *Applied Thermal Engineering*, 48, pp.63–71. Available at: http://dx.doi.org/10.1016/j.applthermaleng.2012.04.017.

Wang, M. et al., 2013. Thermodynamic analysis and optimization of a solar-driven regenerative organic Rankine cycle (ORC) based on flat-plate solar collectors. *Applied Thermal Engineering*, 50(1), pp.816–825. Available at: http://dx.doi.org/10.1016/j.applthermaleng.2012.08.013.

Von Winterfeldt, D. & Edwards, W., 1986. *Decision Analysis and Behavioral Research*,

World Bank Database, 2016. *Africa - PowerMining Projects Database (2014) - Africa_PowerMining_Projects_Database - ENERGYDATA.INFO*, Available at: https://energydata.info/en/dataset/africa-powermining-projects-database/resource/22ebe338-59ad-47fa-8110-60b25802c179 [Accessed June 3, 2018].

World Economic Forum, 2018. The key trends that will shape renewable energy in 2018 and beyond | World Economic Forum. Available at: https://www.weforum.org/agenda/2018/01/clean-energy-renewable-growth-sustainable-key-trends/ [Accessed August 24, 2018].

Yilmaz, I.H. & Söylemez, M.S., 2014. Thermo-mathematical modeling of parabolic trough collector. *Energy Conversion and Management*, 88, pp.768–784.